Title
Advanced two-photon fluorescence microscopy techniques for preclinical brain research

Author
Fan, Jiang Lan

Publication Date
2022

Peer reviewed|Thesis/dissertation

Advanced two-photon fluorescence microscopy techniques for preclinical brain research

by

Jiang Lan Fan

A thesis submitted in partial satisfaction of the

requirements for the degree of

Joint Doctor of Philosophy

with The University of California, San Francisco

in

Bioengineering

in the

Graduate Division

of the

University of California, Berkeley

Committee in charge:

Professor Na Ji, Chair

Professor Marla Feller

Professor Srikantan Nagarajan

Fall 2022

Abstract

Advanced two-photon fluorescence microscopy techniques for preclinical brain research

by

Jiang Lan Fan

Joint Doctor of Philosophy
with The University of California, San Francisco in Bioengineering

University of California, Berkeley

Professor Na Ji, Chair

Two-photon fluorescence microscopy is an indispensable tool in modern systems neuroscience, with its high spatial resolution, high temporal resolution, and ability to harness the target specificity of genetic tools. Its usefulness is underscored by its ubiquity in both technology-driven and science-driven research laboratories around the world, made even more accessible with off-the-shelf microscopes sold by many industry partners. Although incompatible with human clinical research due to a need for an exogenous fluorescent indicator, two-photon fluorescence microscopy shines when applied to preclinical small animal models such as the laboratory mouse that can harness a full library of transgenic and acute genetic tools to study healthy and diseased physiology. Insights learned from imaging experiments performed in these animal models can then be used to guide clinical therapies in human patients. This thesis aims to develop and validate novel neural technologies that marry two-photon fluorescence microscopy with preclinical research applications, while keeping accessibility as a core goal.

The first section of this thesis explores the use of Bessel two-photon fluorescence microscopy in the study of neurovascular dynamics. Characterizing the dynamics of vasodilation, vasoconstriction, and blood flow in the brain can guide therapies for neurovascular pathologies such as traumatic brain injury and stroke. This study establishes Bessel two-photon fluorescence microscopy as a superior method for observing neurovascular dynamics over the conventional Gaussian two-photon fluorescence microscopy due to its fast volumetric imaging speed and integration of fluorescence signal. An embodiment of accessible technologies and in collaboration with an industrial partner, a commercial Bessel two-photon fluorescence microscopy system was designed, built, and used in this study.

The next section of this thesis introduces and implements two techniques that complement Bessel two-photon fluorescence microscopy: adaptive optics and Bessel-droplet focus. Both methods improved the imaging quality of a commercial Bessel two-photon fluorescence microscope without the need of additional hardware.

The final section of this thesis combines two-photon fluorescence microscopy with cortical electrical stimulation to understand how the cortical microcircuit responds to electrical perturbation. Cortical electrical stimulation can be a powerful tool in clinical treatment, but its application has been hampered by a lack of understanding on the input-output relationship between stimulation parameters and neural response, as well as how stimulation can perturb regular cortical functions such as sensory processing. By performing concurrent brain-surface electrical stimulation and two-photon imaging of genetically defined neuronal subtypes in the awake mouse, this study uncovers a mechanism where the sensory-evoked excitatory cortical response is reduced through direct electrical activation of an inhibitory neuron population.

The technologies and discoveries described in this thesis, through their accessibility and clinical relevance, aspire to enable future research pursuits of scientific discovery and therapy development.

To my mother and father,
who worked tirelessly to provide me
with every opportunity to succeed

Contents

Acknowledgements

I'd like to begin these acknowledgements by thanking my incredible mentor and inspiration, Prof. Na Ji, for greatly exceeding my expectations on what an academic mentor could be. Na's superbly sharp mind must be experienced first-hand to fully appreciate, as I've never had a meeting with her that didn't leave me with new insights and new admiration of her intelligence. She's also an excellent science communicator and an advocate for well-written papers and well-practiced talks. Furthermore, she leads by example with her elite work ethic, where she'll always find time to discuss science, troubleshoot lab equipment, review data, and edit papers and presentations despite her busy schedule. These are all outwardly apparent traits that have led to her running a world-class research lab, yet what makes her really stand out as a mentor, in my mind, is her empathy, patience, and passion. She likes to say that she chose to move to UC Berkeley because she loves mentoring students, and she's proven this to be true time and time again. Whether it's discussions about life outside of the lab, stories of her lived experiences, or just down-to-earth small talk, I've felt very welcomed and cared for not just as a researcher but as an individual, throughout my time in her lab. I really cannot believe my luck in finding such a compatible and compassionate mentor.

I'd like to thank my colleagues and mentors in the Ji Lab who are all not only fantastic scientists, but wonderful people. Dr. Guanghan Meng, who was my first introduction to the Ji Lab, is an ambitious class project partner turned treasured friend. Dr. Ryan Natan, who taught me mouse surgical technique, is an especially enjoyable person to converse with, whether it be about science or life. Dr. Wei Chen, who taught me all the practical knowledge of building and running an advanced microscope, continues to be an indispensable resource for optics knowledge. Dr. Jose Rivera, who I had the pleasure of working closely with on a project, is a capable, yet humble, presence in the lab. Dr. Qinrong Zhang, my desk neighbor for years, kept me company while the lab was still transitioning from Janelia. Dr. Yajie Liang, who I was lucky enough to shadow for mouse surgeries, is an incredible surgeon and science colleague. I'd like to also show my gratitude towards Dr. Katharine Borges, Dr. Cristina Rodriguez, Dr. Xinxin Ge, Benno Giammarinaro, and Yuhan Yang, who have been valuable academic resources in my journey. I'd like to thank Ha Yun (Anna) Yoon and Hyeonggeon (Ed) Kim for being patient mentees – I'm happy the lab is in capable hands. My thanks also go out to all the other Ji lab members, past and present, who contributed to such a wonderful learning and work environment.

During my time in the Ji lab, Na has given me many opportunities to work with collaborators, sometimes just to try new ideas, but other times blossoming into rich projects. I would like to thank these collaborators for the knowledge and insights they have imbued in me. Dr. Stefano Cabrini, Arian Gashi, and the rest of the team at the Molecular Foundry in LBL, who trained me on microfabrication techniques, gave me valuable and practical project advice. Dr. Wei Sun, Dr. Henry Haeberle, and the rest of the microscopy team at Thorlabs, who developed the initial hardware and software for the commercial Bessel microscope, provided valuable, practical help with the microscope, as well as scientific help on our collaborative manuscript. Dr. Youngbin Tchoe, Dr. Keundong Lee, and the rest of the team led by Prof. Shadi Dayeh at UCSD, who are the brilliant scientists behind designing and fabricating the platinum-nanorod electrode arrays, graciously provided me with electrodes and the practical know-how to use them effectively. Prof. Eric Halgren at UCSD, who felt like a personal mentor as much as he was a collaborator, spent a

full weekend with me in the lab excitedly performing proof-of-concept experiments, took me to an impromptu lunch at a conference, and continue to make time for enthusiastic scientific discussion. Dr. Gokul Upadhyayula, a leading expert in computational image processing who helped me with analyses, also happened to be a wonderful instructor who I GSI'd for. I was also lucky to be part of many shorter collaborative sessions with the Kaufer (UCB), Kato (UCSF), Paninski (Columbia), Lin (Stanford), Hallatschek (UCB), and Denes (LBL) labs, which gave me both a breadth of experience and a breath of fresh air.

I would like to give thanks to a few more people who were indispensable during my time in the graduate program. Dr. Will Liberti, who I look up to as a brilliant scientist and charismatic person, is also who I look across the table to while eating pizza. A heartfelt thanks to Dr. AJ Velasquez-Mao, Dr. Caylin Colson, Dr. Alejandro Morales, Nathan Ersaro, Louise Hansen, Barry Fung, Alden Moss, Michael Cronce, and others in my program cohort who I've taken classes and spent enjoyable time with. I'd like to thank Prof. Steven Conolly for being my academic advisor in the program, and both Kristin Olson and Rocio Sanchez for being fantastic graduate program advisors over the years. I'd like to give a special thanks to my thesis committee members Prof. Marla Feller and Prof. Srikantan Nagarajan for taking time out of their busy schedules to help me in my journey by providing valuable insights and feedback on my research. I'd like to also thank my qualifying exam committee, Prof. Laura Waller, Prof. Yang Dan, Prof. Saul Kato, and Prof. Kristofer Bouchard for assisting me in that milestone moment.

I would like to thank the long list of incredible academic mentors I've had the privilege of learning from prior to joining the Ji Lab. I'd like to thank Dr. Supin Chen, Dr. Allison Yorita, Jeanine Pebbles, and the rest of the LLNL team for introducing me to clean room fabrication techniques before and during my first year rotation. I'd like to thank Prof. Michel Maharbiz, Dr. Travis Massey, Dr. David Piech, and Oliver Chen for introducing me to their science fiction world of implantable MEMS devices during my other enjoyable rotation. Prof. Richard Ivry, Prof. Yang Dan, Prof. Loren Frank, Dr. Matthew Crossley, Dr. Siyu Zhang, and Dr. Min Xu deserve a special thanks for initially exposing me to academic research and, through their teachings, giving me the courage to pursue this graduate degree. I'd like to give a special thanks to two incredible graduate student mentors, Dr. Jason Chung and Dr. Hannah Joo, who in addition to teaching me a huge number of skills which set me up to succeed, treated me, a lab technician, as a peer and friend. The time I spent with them strongly influenced my research interests and I cannot express how valuable those years were to me, academically and personally.

I end these acknowledgements by thanking the people most important in my life, my family. My beautiful, thoughtful, resilient, hilarious, and encouraging wife, Tricia Tsui, who I've spent almost 8 years with, has been a much-needed reliable constant in my life. She makes me a better person by her example, but also cares for me when I don't care for myself. I am so thankful that she continues to choose to be with me. My mother and father, who upended their lives to move from China to Canada over 20 years ago to provide me with a brighter future, are the biggest inspirations in my life. Over the years, they have worked hard to provide me with the best resources and opportunities to pursue my dreams, for which I am forever indebted and grateful. I would not be here without their encouragement and unwavering support, and so this thesis is dedicated to them.

Preface

A common struggle among graduate students who dedicate their time towards technology development is the worry and realization that their research product will likely not be adopted by the intended users. It is a sobering truth that most advanced research techniques do not see the light of day beyond the walls of their laboratory. A major contributing factor to this is a lack of motivation to continue developing the technique beyond the initial proof-of-concept. Academics chase novel challenges and are rewarded with publications and citations when they conquer them, but the same is not true for incremental improvements on existing techniques that make them more robust, easy to use, or cheaper.

We won't need to look further than my own past research for an example of this. Before my graduate studies, I co-first-authored a study on a novel microfabrication method to develop guide shuttles for the implant of flexible depth electrodes into the brain[1]. Unfortunately, to this day other research groups beyond close collaborators of my former lab have not been able to use the technology developed in the study, despite its benefits, due to both the difficulty of device fabrication and surgical methods. Simplifying the methods and commercializing the product would greatly help the speed of adoption and maximize its impact, but require funding, personnel, and a company willing to take on the risks.

Another major contributing factor to the demise of most advanced technology methods is a disconnect between the goals of the technology developer and the end user. In most cases, the two roles are held by separate people, oftentimes in separate research labs with distinct expertise and minimal cross-communication. This leads to situations where the technologist incorrectly assumes research needs and use cases without consulting the end user. As a result, the end user receives a product that is either not capable of addressing their research questions or overly complicated for an incremental gain in performance. A primary draw of the lab of Prof. Na Ji is that both technologists and end users work in the same space and collaborate on the same projects. The benefit of working in this environment is the open communication that keeps researchers focused on developing genuinely useful technologies.

Since the start of my graduate studies, I have been drawn to the prospects of developing technologies both adoptable by neuroscientists and useful for scientific discovery. My thesis contains an underlying theme of technology accessibility, through commercialization and simplification of once-advanced imaging techniques. Furthermore, my thesis focuses on methods that directly address unmet needs in current preclinical research fields. Included in these methods-focused studies are experiments that answer novel neuroscience questions. Through taking these technology-focused studies one step further into neuroscience, I play both the role of technologist and end user to validate the utility of the developed techniques.

Chapter 1: Introduction

1.1 Two-photon laser scanning fluorescence microscopy

Two-photon laser scanning fluorescence microscopy[2], or two-photon fluorescence microscopy (2PFM) for short, has proven itself to be an indispensable tool in biological research over the last 3 decades. Where it lacks in spatial resolution compared to confocal microscopy and temporal resolution compared to widefield microscopy, it makes up for them with its ability to image deep into opaque biological tissue. This is possible due to three factors. Longer excitation wavelengths in the near infrared (NIR) spectrum can better penetrate opaque tissue because of both reduced scattering and absorption. The nonlinear relationship between laser intensity and fluorescence signal due to the two-photon absorption process results in optical sectioning during excitation. Finally, the efficient collection of emitted fluorescence without the need for de-scanning or confocal filtering allows for minimal loss of emission signal.

Even at hundreds of microns into opaque tissues, 2PFM still has fantastic spatial resolution capable of discerning structures that are <1 micron in size. Temporal resolution is where 2PFM falls short of other methods since it uses a point-by-point scanning approach to produce an image. With the advent of faster scanning methods[3], deciding on 2PFM parameters is now a question of balancing spatial resolution, temporal resolution, signal-to-noise ratio (SNR), and technical complexity.

A large part of the SNR discussion lies upon the fluorophores used in 2PFM. Because 2PFM is a fluorescence imaging technique, any fluorescent compound with a two-photon cross-section can be used as a contrast agent. Over the last few decades, countless fluorophores, both inorganic and organic, endogenous and exogenous, synthetic and genetically encoded, static and dynamic, have been used in biological research. New fluorescent indicators are invented every year to improve the 2PFM method with brighter signal, better dynamics, higher specificity, lower toxicity, and new molecular targets[4,5].

The combination of resolution, labeling specificity, and compatibility with opaque tissue make 2PFM very useful in biological research and has fueled its growth into an indispensable research tool of the 21st century.

1.2 The ubiquity of two-photon fluorescence microscopy in modern systems neuroscience

Unsurprisingly, the field of modern systems neuroscience has fully embraced 2PFM as a standard method for studying neural activity across cell types and brain regions, in several model organisms in healthy and diseased states. Systems neuroscience uses the spatial resolution of 2PFM to its fullest, since the smallest features of interest are the synapse-forming axonal boutons and dendritic spines, which requires the submicron resolution of 2PFM to resolve. Temporal resolution is determined by the dynamics of the underlying physiology: in the case of fluorescent indicators reporting calcium influx during neural activity[6], a sampling rate of a few Hz is sufficient. For

fluorescent indicators reporting membrane voltage[7], hundreds to thousands of frames per second[8] may be necessary.

Molecular and cellular specificity of the fluorescence signal is a major advantage of 2PFM over traditional electrophysiology recordings in systems neuroscience. For example, the ability to unambiguously distinguish between genetically defined neuronal subtypes and cortical layers allow deeper understanding of connectivity in the cortical circuit. Furthermore, specific fluorescent molecules can monitor chemical activity in the brain to provide a more complete picture of communication pathways beyond the action potential (AP). Finally, fluorescent dyes and proteins can label the non-neuronal components of the brain, such as neurovasculature and glia, which can shed new insight into their roles in both basic science and clinically motivated questions.

The clear-cut benefits provided by 2PFM have lifted this imaging method to the forefront of systems neuroscience research, preferred by countless academic labs around the world. A researcher can choose to work with a lab with 2PFM hardware and expertise, build their own microscope, or buy one of the many commercially available two-photon systems. However, like all technologies developed for research, 2PFM was not easily accessible, nor easy to use, at its inception.

1.3 Medical treatments in the brain benefit from pre-clinical findings

Techniques in clinical practice are in large part shaped by preclinical research performed in academic labs. Coined “preclinical” due to its goal of attaining conclusive evidence that can directly benefit clinical therapies, this type of research involves working with animals, most commonly lab mice, to observe clinical-like conditions or test therapies with greater granular control of experimental parameters than what is possible with human subjects.

Much of clinical neuroscience practice is built upon our preclinical understanding of brain structure and function in health and disease. For example, brain-computer interfaces (BCIs) using neural activity to control a cursor or robotic arm in real-time were first demonstrated in rats and non-human primates (NHPs) over 2 decades ago[9,10]. Since then, the technology, including both implant hardware and decoding algorithm, has been refined and successfully implemented in dozens of human tetraplegic patients[11–13] for cursor movement, text input, and motorized arm control. Another example is in deep brain stimulation (DBS) of Parkinson’s Disease (PD) patients. With the discovery of a NHP disease model for PD in the 1980’s, brain regions which cause PD symptoms were found through lesion experiments and DBS methods were developed to treat human patients soon after[14–16]. DBS is now by far the most common brain implant, with hundreds of thousands of patients implanted worldwide[17]. A final example is the discovery of the enzyme tissue plasminogen activator (tPA) for treating acute ischemic stroke. After the discovery of the protein and its clot-dissolving properties, tPA was first tested and validated in rabbit models in the 1970’s before human use[18,19]. Commercially produced tPA is still the most commonly used treatment for ischemic stroke today.

Given the precedence of preclinical neuroscience findings being used for the design and approval of medical applications, the future of clinical neuroscience may lie in current modern preclinical

research techniques, such as 2PFM. Animal experiments that take advantage of 2PFM's strengths in resolution and labeling specificity can provide a highly detailed and mechanistic understanding of a clinical treatment's effect on the brain. Results from animal experiments can then be used to guide the direction of treatment development and eventual clinical trial.

1.4 Adapting two-photon fluorescence microscopy towards clinically relevant research

Each year, 2PFM is increasingly being used for preclinical research[20–22] for its high resolution, cell and molecular specificity, ability to image into opaque tissue, and accessibility. However, some valuable preclinical questions require research methods with capabilities beyond that of conventional 2PFM alone. *The goal of my thesis is to develop and test neural technologies that apply the two-photon fluorescence microscopy method towards unmet preclinical research needs.* The rest of this thesis is organized as follows:

Chapter 2 presents a published study which adapts a fast volumetric 2PFM method for high-throughput measurement of neurovascular dynamics[23]. Characterizing the dynamics of vasodilation, vasoconstriction, and blood flow in the brain can guide therapies for neurovascular pathologies such as traumatic brain injury and stroke. Conventional 2PFM has low throughput when used to measure hemodynamics *in vivo*. In this chapter, we demonstrate the benefits of Bessel 2PFM, in measurement throughput and in simplifying analyses.

Chapter 3 develops and validates a next-generation fast volumetric two-photon fluorescence microscope that is easy to operate and commercially available. Both Bessel-droplet and Bessel AO 2PFM methods have been developed in home-built microscope systems, but not validated to work in commercial microscopes with fewer optical components. In this chapter, we validated that these methods improved the imaging quality of a commercial microscope without the need of additional hardware.

Chapter 4 details a study which combines 2PFM with cortical electrical stimulation to understand how stimulation perturbs a functioning cortical circuit. Cortical electrical stimulation can be a powerful tool in clinical treatment, but its application has been hampered by a lack of understanding on the input-output relationship between stimulation parameters and neural response, as well as how stimulation can perturb regular cortical functions such as sensory processing. In this chapter, we performed concurrent brain-surface electrical stimulation and 2PFM of genetically defined neuronal subtypes in the awake mouse to tease apart the relationship between stimulation and cortical circuit response.

Chapter 2: Bessel two-photon fluorescence microscopy for high-throughput readout of neurovascular dynamics

2.1 Introduction

2.1.1 The scientific and clinical importance of studying neurovasculature

Studying hemodynamics in the brain at capillary resolution provides insight into how neural and glial activities are coupled with local metabolism[24–26]. Local changes in brain hemodynamics form the basis of cerebral blood volume (CBV), cerebral blood flow, and blood-oxygenation level-dependent (BOLD) signals in functional magnetic resonance imaging (fMRI)[27,28]. These signals are often used in the medical imaging field as a proxy for neural activity when performing functional experiments or structural targeting[29,30]. Furthermore, abnormal hemodynamics are associated with numerous medical conditions including stroke[20,31,32], diabetes[33], chronic stress[34], and Alzheimer's disease[35–37] models.

Despite the importance of understanding the detailed functional roles of neurovasculature in basic research in order to guide clinical practice, existing optical techniques for interrogating hemodynamics in animals, primarily intrinsic signal optical imaging (ISOI)[30,38–40] and 2PFM[41], are limited in scope. ISOI does not require exogenous contrast agents but lacks capillary-resolving spatial resolution and the ability to image at depth. 2PFM can interrogate hemodynamics at high spatial resolution and at depth but is prohibitively slow at imaging brain volumes. An ideal imaging technique should have high spatial resolution to resolve the smallest capillaries and fast volumetric imaging rate to resolve blood flow dynamics.

2.1.2 Shortcomings of conventional 2PFM for studying neurovascular dynamics

2PFM is a popular method for in vivo imaging of the brain because of its ability to image structures at high spatial resolution within scattering tissue[2]. Two-photon excitation requires high peak intensity and thus restricts the fluorescence generation to a thin section at the focal plane, enabling 2PFM to optically section three-dimensional (3D) samples. With high spatial resolution in 3D, it has been routinely used to image neurovasculature at hundreds of microns below the brain surface using fluorescent dyes labeling the blood stream[41,42]. Several studies also demonstrated concurrent imaging of vasculature with neural activity and/or glia using multi-color fluorescent labeling[20,43–47].

To capture hemodynamic events occurring on second (vasodilation and vasoconstriction) to millisecond (red blood cell flow speed) timescales, 2PFM is most often used to capture two-dimensional (2D) frames at video rate (e.g., 30 Hz) or one-dimensional (1D) line scans at hundreds to thousands of lines per second. When applied to monitoring 3D vasculature populations, however, the volumetric imaging speed is limited by the need to serially scan the excitation focus in 3D. For example, for a 2PFM equipped with an 8-kHz resonant galvanometer and bi-directional scanning, imaging a 1 mm × 1 mm × 0.1 mm volume at 1 μm^3 voxel size would take over 6 s (not including

the additional time needed to move the excitation focus along the optical axis), too slow to image most hemodynamic events.

Even for imaging hemodynamics in 1D or 2D, standard 2PFM faces challenges arising from the micron-sized axial dimension of its excitation focus. Even though standard 2PFM can capture long segments of superficial, horizontally oriented pial vessels and measure their blood flow speed, it captures only cross-sections of penetrating vessels and capillaries that constitute most vasculature below cortical surface[48], making it exceedingly difficult to measure their blood flow speed. In addition, axial movements of the brain, even if only microns in amplitude, can shift structures out of the excitation focus, causing 2PFM to image different sample planes which introduces errors in hemodynamic measurements that are difficult to correct.

2.1.3 Bessel 2PFM uses an elongated focus for fast volumetric imaging

Recently, 2PFM methods utilizing axially extended Bessel-like foci[49–51] have been developed for high-speed volumetric imaging of neural activity in the brain[52–55]. Bessel beam generation theory has been explained in detail[56,57], but a short summary is as follows:

Conventional 2PFM utilizes Gaussian beam illumination to form a focus with diffraction-limited lateral and axial resolution. The lateral resolution is determined by the marginal rays, which are the rays at the largest numerical aperture (NA), or the edge, of the objective lens. The axial resolution is determined by the interference between the on-axis ray and the marginal ray. Bessel beam illumination, which takes the shape of a ring at the objective back pupil, removes on-axis rays, and therefore greatly extends the axial focus while maintaining high lateral resolution. Producing a Bessel beam illumination pattern involves three components: A radially symmetric diffraction grating, which directs most of the laser energy to the 1st order annular beam, a lens that focuses the diffracted beam, and an annular mask designed to remove energy from all other diffracted orders, including the 0th order, when placed at the lens' focal plane. The annular mask is then imaged onto the back pupil of the objective lens to generate a Bessel focus.

Scanning a Bessel focus laterally in 2D generates a projected view of a volume defined by the area scanned and the axial extent of the focus, the latter of which can span tens to hundreds of microns. As a result, the 2D frame rate becomes the effective volumetric imaging speed. In this study, we used a commercial 2PFM equipped with a Bessel focus module and applied it to cortical vasculature imaging in the awake mouse brain at high throughput. Imaging vasculature at up to 600 μm below brain surface, we demonstrated hemodynamic measurement over 1.4 mm × 1.4 mm × 0.1 mm volumes at 15 Hz. The axially elongated excitation volume of Bessel foci produced two-photon fluorescence signal that was proportional to vessel size, which enabled us to use fluorescence signal as a convenient measure of vasodilation and vasoconstriction down to capillary resolution. By imaging vasculature volumetrically at 99 Hz, we were also able to measure 3D blood flow speeds from both superficial and deeply penetrating vessels, including capillaries, up to 3 mm/s.

2.2 Methods

2.2.1 Design and characterization of a commercial 2PFM with a Bessel focus module

We designed and constructed a commercially available Thorlabs Bergamo® II multiphoton microscope with a Bessel focus module for high-speed volumetric imaging. All hardware controls and data acquisition were performed using the ThorImage software. A titanium-sapphire laser (Chameleon Ultra II, Coherent Inc.) tuned to 920 nm was used as the two-photon excitation source for all experiments. A 16x/0.8-NA water-dipping objective lens (Nikon) was used for all characterization and imaging data in this study. Bessel and Gaussian beam paths were switchable using an integrated, software-controlled rotatable half-wave plate combined with a polarizing beamsplitter and a removable mirror. Compared to the Gaussian beam path, the Bessel beam path had an additional lens (focal length = 400 mm) with a liquid crystal spatial light modulator (SLM, ODPDM512-1064, Meadowlark Inc.) at its front focal plane and an annular aperture mask at its back focal plane. A 0-π concentric binary phase grating pattern was presented on the SLM so that its 1st order diffraction ring was focused on the annular mask by the lens. The annular mask was custom fabricated (chrome deposited on quartz, Photo Sciences Inc.) to block 0th and higher order diffractions and its parameters (inner diameter = 2.3 mm, outer diameter = 2.5 mm) were chosen to generate a Bessel focus with a theoretical axial full-width at half-maxima (FWHM) of 85 μm at the focal plane of the 16x/0.8-NA objective, as calculated following Lu et al.[52]. The annular mask was 4f-conjugated to the non-resonant galvo surface in the galvo-resonant galvo scanning system. Fluorescence emission was collected by two GaAsP photomultiplier tubes (PMTs) with emission filters for simultaneous 2-color imaging of green (525/50 nm) and red (607/70 nm) fluorescence (BDF25GR, Thorlabs). Post-objective laser power was measured with a power meter calibrated at 920 nm. The system was designed and built in collaboration with Thorlabs and is now a commercially available microscope system (Bergamo® II series). 0.2-μm-diameter yellow-green fluorescent beads (FluoSpheres®, Thermo Fisher Scientific) attached to a glass slide were imaged using both the Gaussian and Bessel configurations of the microscope to measure lateral and axial point spread functions (PSFs). 3D resolution was measured by taking the FWHM of the PSFs. The largest field of view (FOV) achieved with the 16x/0.8 NA objective was 1.4 mm x 1.4 mm.

2.2.2 Mouse surgical preparation

All animal experiments were conducted according to the National Institutes of Health guidelines for animal research. Procedures and protocols on mice were approved by the Animal Care and Use Committee at the University of California, Berkeley. In vivo imaging data in this study were collected from four wild-type (Jackson Laboratories, Black 6, stock no. 000664), one Thy1-GFP (neuronal green fluorescence protein expression, Jackson Laboratories, Tg(Thy1-EGFP)MJrs/J, stock no. 007788), and two Aldh1l1-GFP (pan-glial green fluorescence protein expression, Mutant Mouse Resource & Research Centers, Tg(Aldh1l1-EGFP)OFC789Gsat/Mmucd, stock no. 011015-UCD) mice socially housed under normal light cycle. Cranial window implantation procedure has been described previously[58]. In brief, mice aged 3-4 months were anesthetized with 1 – 2% isoflurane in O2 combined with the analgesic buprenorphine (SC, 0.1 mg/kg) and head-fixed in a stereotaxic apparatus (Kopf Instruments). A 3.5-mm-diameter craniotomy was made over the left V1 centered at -2.5 mm medial-lateral and 1 mm anterior-posterior to lambda. A glass

window made of a single coverslip (Fisher Scientific, no. 1.5) was embedded in the craniotomy, flush with the skull, and sealed by a tissue adhesive (VetBond, 3M). A stainless-steel head-bar was then firmly attached to the skull with dental acrylic. Implanted mice were provided with a post-operative analgesia Meloxicam (SC, 5 mg/kg) for 2 days and allowed to recover for at least 2 weeks prior to imaging experiments.

2.2.3 *In vivo* imaging

All imaging experiments were performed on head-fixed, awake mice. Prior to imaging, animals were briefly anesthetized with isoflurane and retro-orbitally injected with 50 µL of 5% (w/v) 70-kDa dextran-conjugated Texas Red fluorescent dye. Mice were then head-fixed under the objective lens. First, structural image stacks were taken using both Gaussian and Bessel beam paths at the largest FOV. For the two Aldh1l1-GFP transgenic mice, blood vessel (red) and glial (green) structures were imaged concurrently. Next, volumetric imaging of blood vessel dynamics was performed at 15 Hz (1024 x 1024-pixel frames) or 99 Hz (128 x 128-pixel frames) in distinct FOVs using the Bessel focus module. During some experiments, we concurrently imaged the mouse's ipsilateral eye illuminated by infrared LEDs using a camera (Mako U-130B) with an infrared filter. The bright spot on the upper left quadrant of the pupil image (Fig. 4C) was the reflection of the infrared illuminator and did not affect pupil diameter analysis. For high-resolution capillary imaging, small FOVs were imaged at 30 Hz (512 x 512-pixels per frame) with 0.2 µm pixel size, first with Gaussian then Bessel foci. Due to the higher fraction of energy distributed in the side rings of a Bessel focus compared to a Gaussian focus[57], higher post-objective laser power was used for Bessel compared to Gaussian imaging at the same cortical depth (e.g., at 100 µm below pia surface, Bessel: 167-217 mW, Gaussian: 35-47 mW).

2.2.4 Data analysis

All image processing, visualization, and analysis were performed in ImageJ and MATLAB (MathWorks). Image sequences from Bessel functional data were registered to remove rigid lateral motion artifacts before further analysis. In all figures, superficial Bessel data (0 to 100 µm below surface of dura mater), unless otherwise stated, were visualized using the gray lookup table on the square root of fluorescence signal (normalized from minimum to maximum) to improve the visibility of dim structures without saturating bright structures. All Gaussian data and all other Bessel data were visualized using the gray lookup table on their fluorescence signal (normalized from minimum to maximum).

For Fig. 3 and its associated analysis, fluorescence signal and blood vessel size of 60 vessel segments were measured in both the Bessel image (900 frame average) and the corresponding Gaussian stack (5 frame average, 1 µm step size). For the Bessel image, line segments of 1-pixel thickness were drawn perpendicular to the blood vessels. Fluorescence signals were chosen to be the brightest pixel along the line segments and vessel sizes were the total numbers of pixels above a common threshold. The threshold was calculated by first selecting a region without vessels near the center of the image then adding 3 standard deviations to the mean pixel value of the region. For the Gaussian image stack, a line segment was drawn perpendicular to the same blood vessel in the Bessel image and the stack was resliced to show the axial cross section of the vessel:

fluorescence intensity was chosen to be the brightest pixel in this 2D cross section, and size was represented by the FWHM at the widest point in the cross section.

For Fig. 4, 1-minute-long 15 Hz functional data were used to study the relationship between fluorescence intensity and vasodilation. First, we performed a 5-frame (0.33 second) moving average of the raw frames to remove high-frequency fluorescence signal variations due to blood flow. For four blood vessels, we extracted the time traces of the average signal from 256-pixel-area (450 μm^2) ROIs fully encompassed within the lumen of the vessels and calculated their $\Delta F/F$ traces with F being the median value of the time trace. Blood vessel diameters were measured by thresholding the moving-averaged images at 3 standard deviations above the mean background signal near the blood vessel of interest, and then calculating the number of pixels above threshold within a 10-pixel-wide line segment drawn perpendicular to the vessel. The same analysis procedures were performed on four capillaries in higher-resolution (0.2 µm x 0.2 µm pixel size) Gaussian and Bessel data in Fig. 5, with 2 additional steps. 1) Fluctuating background signal was removed from Bessel data with frame-by-frame subtraction of the background signal near the capillary of interest, then adding back a session-averaged background value. By doing this, capillary fluorescence measurements were decoupled from fluctuations originating from out-of-focus fluorescence such as large surface vessel dilations. 2) 30-Hz Gaussian and Bessel data were first temporally binned to 1 second resolution to suppress high-frequency blood-flow-introduced signal variation followed by a 5-frame moving average on fluorescence and diameter measurements, which resulted in 5-second moving averages. For the signal correlation analysis in Fig. 3f-g, large volume (1.4 mm x 1.4 mm x 0.1 mm) Bessel 2PFM raw images were spatially binned to 64 x 64 ROIs (each 16 x 16-pixels) by averaging all pixels within an ROI. The time trace of each ROI was then extracted and correlated with the time trace of a specified target ROI with a sliding window of ±10 frames. The absolute maximum correlation value within the sliding window was used to represent the cross-correlation between the ROI and target ROI. Fig. 6C was created by first dividing standard deviation of the image time stack by the average image and plotted on a color scale. Then, the dimmest 80% of pixels in the average image that represented non-vasculature tissue were set to black. Fig. 6D was created in the same way, with an initial binning to 64 x 64 ROIs.

For the pupil-vessel entrainment experiment in Fig. 7, 10-minute-long 15 Hz functional images at 1024 x 1024-pixel resolution were also binned to 64 x 64 ROIs (each 16 x 16-pixels) by averaging all pixels within an ROI. We used a threshold and fitting method adapted from Diego Barragan ("Tracking pupil using image processing", MATLAB Central File Exchange) to extract pupil diameter from concurrently recorded mouse pupil images. We fit the pupil in each video frame as an oval, and used its width, rather than height, as pupil diameter to reduce squinting and blinking artifacts. The time trace of each ROI was correlated with the mouse's pupil diameter with a sliding window of ±10 frames. The absolute maximum correlation value within the sliding window was used to represent the cross-correlation between the ROI and pupil diameter.

For 3D blood flow speed measurement presented in Fig. 8, blood vessel segments were hand-traced over the average intensity projection of 1-minute-long 99 Hz datasets (two 208 µm x 208 µm x 80 µm volumes 0-80 µm below top pia surface in two mice; two 416 µm x 416 µm x 80 µm volumes 0-80 µm and 100-180 µm below the top pia surface, respectively, in two mice). Raw

Bessel images were then resliced along the length of blood vessel segments and plotted in time as kymographs. Because RBCs excluded fluorescent dye and appeared as dark shadows, they generated diagonal dark streaks in kymographs[42]. We rejected from analysis blood vessel kymographs with little to no RBC streaks visible above the background fluorescence. We measured the 3D lengths of blood vessel segments from skeletonized Gaussian structural data and then nonlinearly transformed the horizontal axes of the kymographs from 2D Bessel projection length to 3D Gaussian structural length for further analysis. We adapted an automated method developed by Chhatbar and Kara[59] to measure the slope of RBC streaks using Sobel filtering and iterative Radon transforms and calculated blood flow speed every 50-frame (0.5 second) kymograph segment. We further rejected from analysis blood vessel segments that had more than one-third of its time trace showing very high (> 5 mm/s) or reversed (< 0 mm/s) flow speeds. Sizes of blood vessel segments were measured by taking the FWHM of a representative hand-drawn line intensity cross-section of each segment from the average intensity projection of the Bessel dataset.

2.3 Results

2.3.1 A high-speed 2PFM equipped with a Bessel focus module

A simplified diagram of the imaging system is shown in Fig. 1a. The entire imaging system including the Bessel focus module is commercially available (Thorlabs Bergamo® II series). The Bessel focus module was located in between the excitation laser and the microscope's main body, which houses an 8-kHz resonant galvanometer–galvanometer pair scanning system. The combination of a rotatable half-wave plate and a polarizing beamsplitter directed the excitation light from the Gaussian beam path (yellow path, Fig. 1a) to the Bessel beam path (red path, Fig. 1a), where it reflected off a spatial light modulator (SLM) with a concentric binary grating pattern that diffracted the excitation light into an annulus. The excitation light was then focused by a lens and spatially filtered by an annular mask, which blocked the non-diffracted light and transmitted the electric field distribution giving rise to the desired axial focus profile[52]. Removing a mirror in the standard (Gaussian) beam path (yellow path, Fig. 1a) allowed the annular illumination to propagate into the microscope. The annular mask was 4f-conjugated to the microscope's galvanometer scanners and subsequently 4f-conjugated to the back focal plane of a 0.8-NA microscope objective. We characterized the point spread functions (PSFs) of the imaging system in both Gaussian and Bessel modes with sub-diffraction-sized 0.2-μm-diameter fluorescent beads (Fig. 1b). The PSF of the 0.8-NA Gaussian focus had a lateral full-width at half-maximum (FWHM) of 0.67 μm and an axial FWHM of 3.1 μm. The PSF of the 0.4-NA Bessel focus had a lateral FWHM of 0.65 μm, a comparable lateral resolution to the 0.8-NA Gaussian focus due to annular illumination giving rise to a sharper central peak[57], and an extended axial FWHM of 67 μm. The 22× increase in the axial excitation range allowed us to use 2D scanning of the Bessel focus to image a volume that would have required tens of 2D frames captured at different axial positions with the Gaussian focus (Fig. 1c), thereby substantially increasing our imaging throughput.

2.3.2 Volumetric structural imaging of blood vessels with Bessel focus scanning

To further test our commercial Bessel 2PFM system, we performed structural imaging over 1.4 mm × 1.4 mm areas of vasculature in five mice using both Gaussian and Bessel foci, with

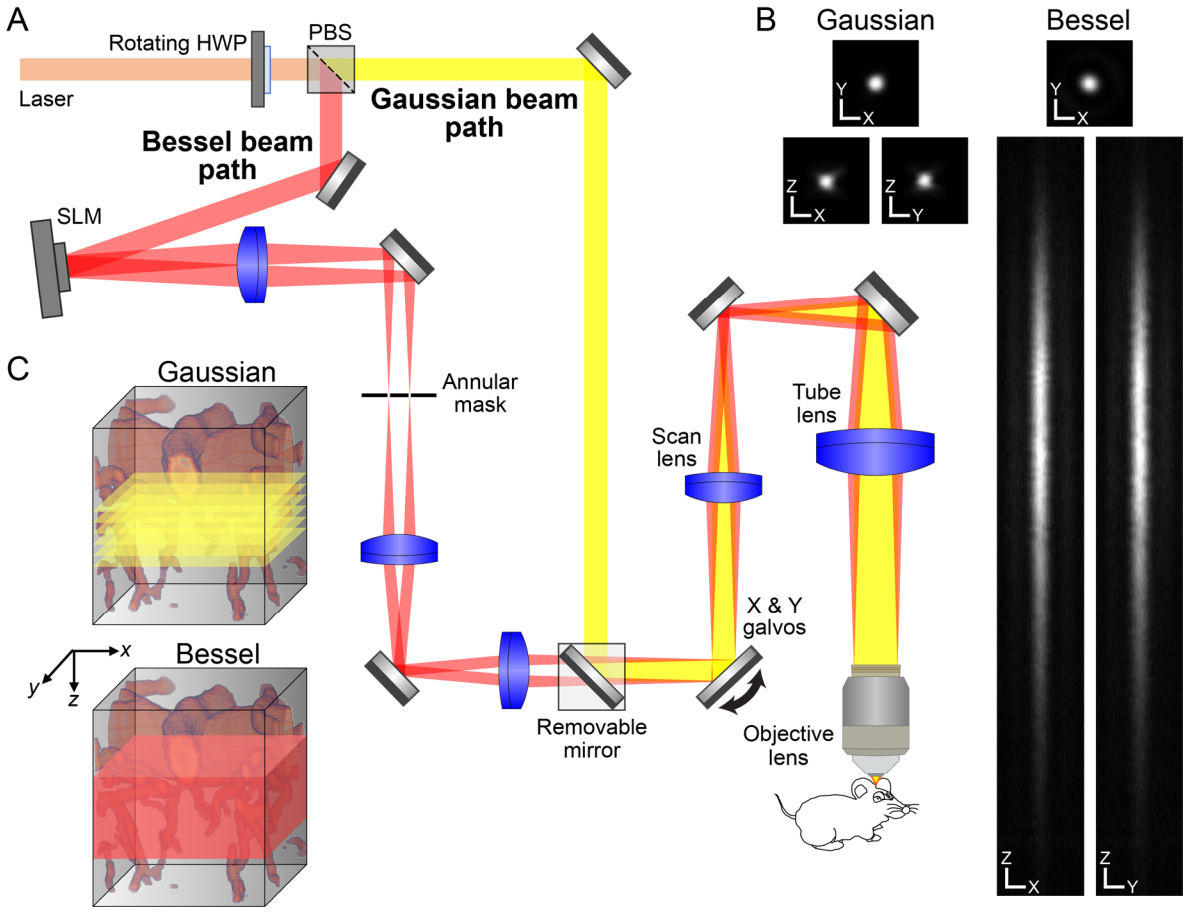

Figure 1. Design and characterization of a commercial two-photon laser scanning microscope with a Bessel focus module.

(A) Schematic of the microscope. A half-wave plate (HWP), a polarizing beamsplitter (PBS), and a removable mirror allow switching between Bessel (yellow) and Gaussian (red) beam paths. In the Bessel path, a spatial light modulator (SLM) and a lens generate an annular illumination pattern, which after spatial filtering by an annular mask is imaged via a 4f system onto the galvos and subsequently imaged via a scan and tube lens pair onto the objective lens back focal plane. **(B)** Lateral and axial point spread functions for Gaussian and Bessel foci. X and Y scale bars: 1 µm. Z scale bar: 5 µm. **(C)** Schematic comparison of Gaussian and Bessel volumetric 2PFM methods. Gaussian volumetric imaging requires multiple 2D frames taken at different Z-positions, while Bessel volumetric imaging is achieved with a single frame.

representative images from one mouse shown in Fig. 2. Gaussian structural imaging was performed on each mouse to obtain 3D morphology of their vasculature network, which enabled us to assign depth information to Bessel data post hoc. Fig. 2a–c shows Gaussian 2PFM images of vasculature labeled with dextran-conjugated Texas Red (peak emission: 615 nm) at 55, 225, and 420 µm below the top surface of the dura mater, respectively. Large segments of pial vessels were visualized in the most superficial image (Fig. 2a). Within cortex, penetrating vessels and capillaries showed up sparsely because only their cross-sections were imaged by the tightly axially confined Gaussian focus. To capture volumes of vasculature, we first scanned the Gaussian focus in 3D.

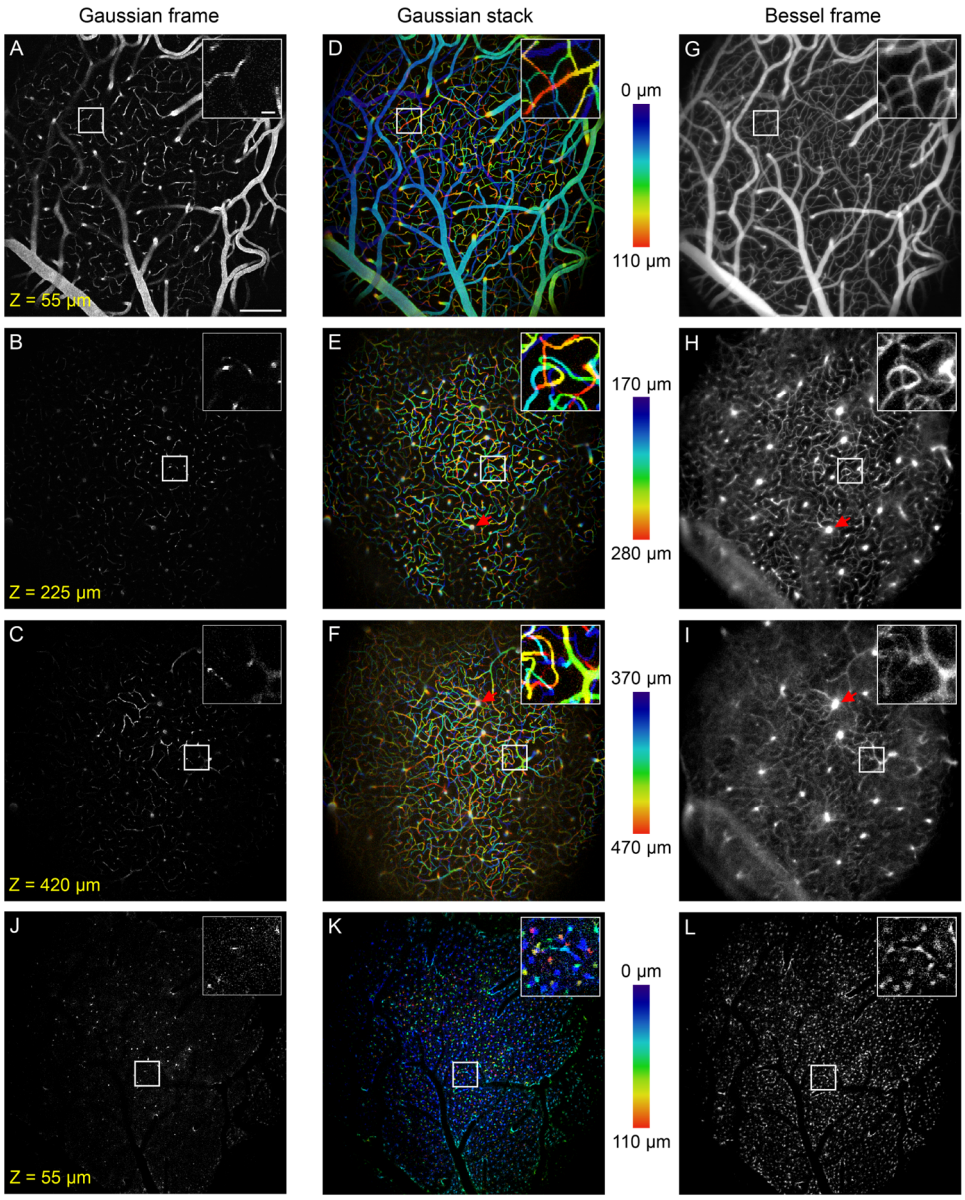

Figure 2. *In vivo* volumetric structural imaging of vasculature and glia with Bessel 2PFM.

(A-C) Gaussian 2PFM images of vasculature labeled with dextran-conjugated Texas Red at 55 µm, 225 µm, and 420 µm depth, respectively, over a 1.4 mm × 1.4 mm area in the mouse cortex *in vivo*. **(D-F)** Gaussian 2PFM image stacks of vasculature at 0 – 110 µm, 170 – 280 µm, and 370 – 470 µm depths, respectively, color-coded by depth. **(G-I)** Scanning the Bessel focus in 2D captured all vasculature in the volumes within (D-F). **(J-L)** Gaussian (J, K) and Bessel (L) images of GFP-expressing glia imaged concurrently with A, D, and G, respectively. Insets: zoomed-in views of the white boxed regions. Red arrowheads: vertically oriented vessels. A and G use a grayscale on the normalized square root of fluorescence signal to highlight dim structures without saturating bright structures. All other panels use grayscale on the normalized linear fluorescence signal. Scale bars: 200 µm for full FOV; 20 µm for insets. Post-objective excitation power: Gaussian: 45-177 mW; Bessel: 217 mW.

Fig. 2d–f shows Gaussian image stacks of vasculature within 0–110, 170–280, and 370–470 µm depth ranges, respectively, taken at 1-µm z-steps and color-coded by depth. Consistent with the Gaussian images in Fig. 2a–c, we observed horizontally located dural and pial vessels in the superficial brain (dark blue and blue-green vessels in Fig. 2d, respectively). Within the cortex, the vasculature was dominated by capillaries that extended over large depth ranges (segments color-coded from blue to red, Fig. 2d–f and insets). Next, by scanning the axially extended Bessel focus (Fig. 1b) in 2D, we imaged 100–110-µm-thick volumes of vasculature simultaneously (Fig. 2g–i) with sufficiently high lateral resolution to resolve individual capillaries (cf. insets in Fig. 2d–i), indicating that Bessel focus scanning drastically improved volumetric imaging throughput without compromising lateral resolution. Penetrating arterioles or venules that ran parallel to the Bessel focus (arrow heads, Fig. 2e, f) generated the brightest fluorescence signal (arrow heads, Fig. 2h, i) because they contained the most fluorophores to be excited by the axially extended Bessel focus. As an example of multicolor volumetric imaging, we simultaneously imaged vasculature and glia cells expressing green fluorescence protein (GFP) in the same cortical volume (i.e., data in Fig. 2a and j, b and k, g and l were acquired simultaneously). A 2D Bessel focus scan recorded vasculature and glia in the 110-µm-thick volume, with the low density of the glia allowing individual cells to be separately identified in the projected view of the Bessel image (Fig. 2j–l and insets).

2.3.3 Fluorescence brightness of vasculature in Bessel images is positively correlated with vasculature size

We systematically compared the vessel and capillary sizes measured by Bessel versus Gaussian focus scanning. We selected 60 segments in Fig. 4a (1.4 mm × 1.4 mm × 100 µm volume, 0–100 µm below the top surface of the pia mater, 1024 × 1024 pixels) and compared their sizes with

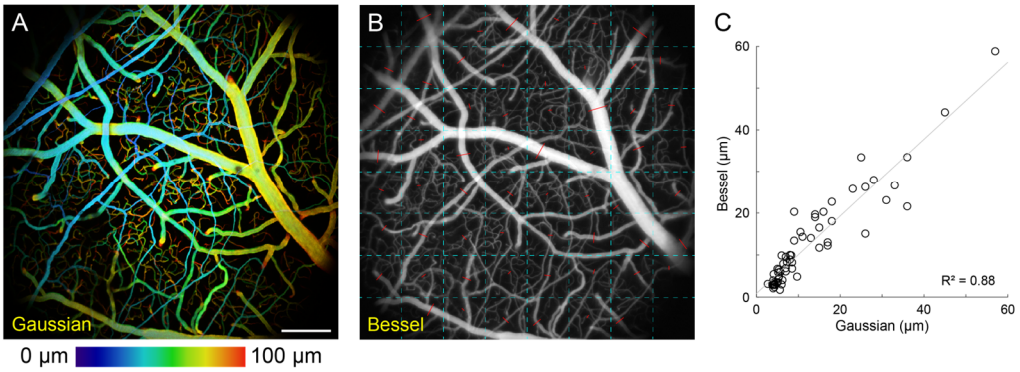

Figure 3. Relationship between blood vessel diameters measured with Gaussian versus Bessel 2PFM methods.

(A) Gaussian image stack of a 1.4 mm x 1.4 mm x 100 µm volume of vasculature, color coded by depth. **(B)** Bessel image of the same volume in A, visualized in grayscale on the normalized square root of fluorescence signal and divided into 8 x 8 equal subregions (cyan dashed lines). One vessel segment was chosen within each subregion except the 4 corner subregions (60 total). Red lines indicate the line along which fluorescence signal and vessel diameter were determined from Gaussian and Bessel image data. **(C)** Scatter plot of the same vessel diameters measured from Gaussian and Bessel data captured at different times. Scale bar: 200 µm. Post-objective power: Gaussian: 45 mW; Bessel: 217 mW.

those measured from the corresponding 3D Gaussian stack (Fig. 3, Methods section 2.2.4). We found that the sizes obtained from both datasets were highly correlated ($R^2 = 0.88$), which indicated that the projected structural images of vasculature volumes from Bessel focus scanning provided accurate measurements of vessel sizes.

Interestingly, visual inspection of vessels and capillaries in Gaussian and Bessel images (Fig. 4b) revealed distinct trends: in Gaussian images, in-focus vessels of different diameters had similar fluorescence brightness, while in Bessel images, larger vessels were much brighter than fine capillaries (Fig. 4b, arrows). These trends were confirmed by systematic analysis on size-brightness correlations using the same 60 vessel segments in Fig. 3. We observed weak positive correlation between fluorescence brightness and vessel size in their Gaussian images ($R^2 = 0.08$), but strong positive correlation ($R^2 = 0.75$) in their Bessel image (Fig. 4c). The strong positive correlation between fluorescence brightness in the Bessel image and vessel size is because larger vessels allowed more fluorescent molecules to be excited along the axial direction by the axially extended Bessel focus (67 µm FWHM), leading to larger fluorescence signal. In contrast, the

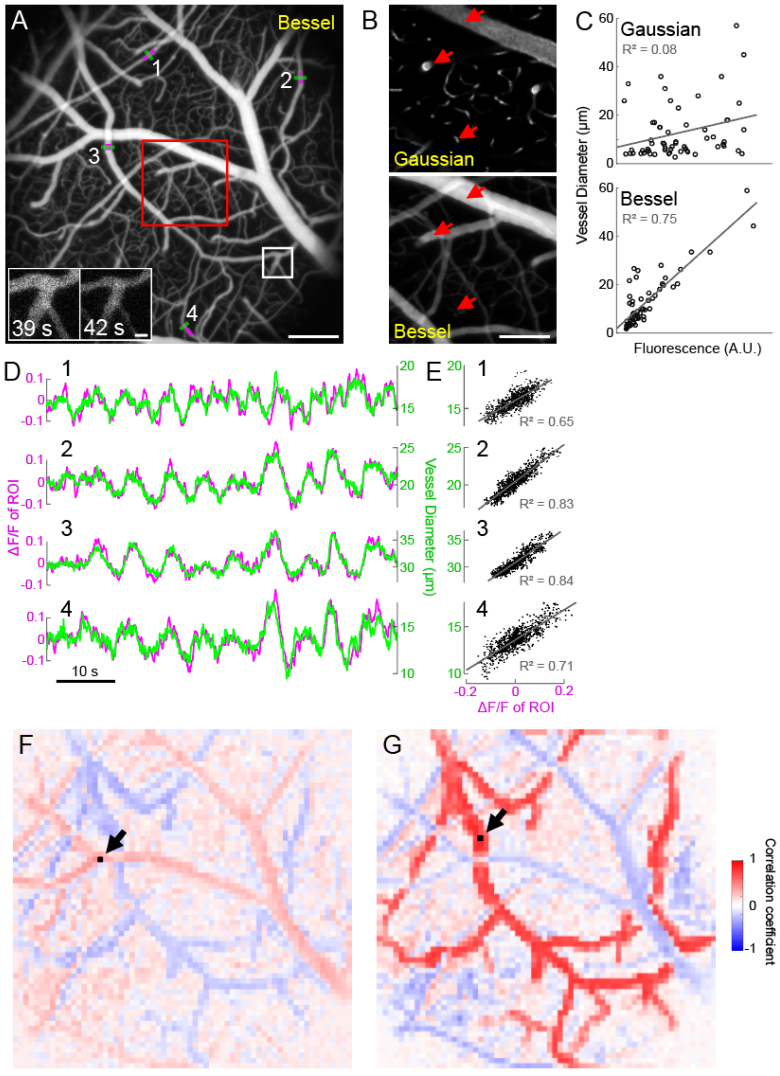

Figure 4. Bessel 2PFM signal is correlated with vessel size and captures distributed dynamics of vasodilation and vasoconstriction in 3D.

(A) A 1.4 mm x 1.4 mm x 0.1 mm volume of vasculature imaged at 15 Hz using Bessel 2PFM, visualized in grayscale on the normalized square root of fluorescence signal. Insets: zoomed-in views of the white-boxed region at two time points, showing changes in vessel size. **(B)** Gaussian (single plane at Z = 50 µm) and Bessel images of the red-boxed region in A captured at different times, visualized in grayscale on the normalized fluorescence signal. Red arrows point to three vessels (large, medium, small) to highlight the differences in their fluorescence signal strength between Gaussian and Bessel 2PFM. **(C)** Fluorescence vs. vessel diameter for 60 vessel segments in A (see Fig. 3) imaged with Gaussian or Bessel 2PFM. **(D)** Time traces of fluorescence signal changes of the magenta ROIs and blood vessel diameter measured along the green lines in A for 4 vessel segments. **(E)** Scatter plot of the data in D. **(F, G)** Maps of cross-correlation coefficients between ROIs tiling the FOV in A and a reference ROI (indicated by arrows and black squares). Scale bars: 200 µm for A, F, G; 20 µm for insets in A; 100 µm for B. Post-objective power: Gaussian: 45 mW; Bessel: 217 mW.

Gaussian focus extended much less axially (3.1 μm FWHM). As a result, its signal did not increase for vessels with larger axial dimensions.

2.3.4 High-throughput volumetric imaging of vasodilation and vasoconstriction

The observed positive correlation between fluorescence brightness and diameter of distinct vessel segments in the Bessel image, although high in value, cannot be relied upon to reach conclusions on relative sizes for different vessels. Even for the vessels in the same field of view (FOV), variations in local tissue scattering, aberration, and orientation relative to the excitation focus led to deviations away from perfect signal-to-size correlation. However, for the same vessel segment, changes in its fluorescence brightness in Bessel 2PFM should be strongly correlated with changes in its size, and thus can be reliably used to detect vasodilation and vasoconstriction. As an example, we used Bessel focus scanning to monitor the vasculature dynamics in 1.4 mm × 1.4 mm × 100 μm volumes at 15 Hz. At this volumetric rate, we captured the hemodynamics of vasodilation and vasoconstriction in five awake mice under fixed ambient lighting condition (e.g., insets in Fig. 4a). We found that temporal variations in vessel size over 1 min of recording (e.g., green traces in Fig. 4d, measured along green lines for four example vessel segments labeled 1–4 in Fig. 4a) were positively correlated with the brightness changes of its lumen (e.g., magenta traces in Fig. 4d, averaged brightness within the magenta regions of interest (ROIs) in Fig. 4a; quantified as $\Delta F/F$, with F being the median value of the time trace) (Fig. 4e, Methods section 2.2.4). The observed dilatory oscillations in Fig. 4d were similar in frequency (~0.1 Hz) to previously observed cerebral vasomotion[60].

We carried out similar analyses for capillaries (vessels with diameters < 6 μm; Fig. 5) in two animals, at 30 Hz and 0.2 μm pixel size. In both Gaussian (Fig. 5c, d) and Bessel (Fig. 5e) modes, we measured diameters of capillary segments and observed dilation and constriction from some capillaries. Our observation that some but not all capillaries dilate is consistent with previous studies where only a fraction of capillaries was found to undergo measurable dilation[61,62]. Those capillaries that did dilate show similar magnitudes of diameter change to those observed previously in response to forepaw or whisker pad stimulations[61–64].

For all example vessels, vessel diameter and fluorescence brightness were highly positively but not perfectly correlated. The lack of perfect correlation was caused by blood cells, which were not labeled by fluorescent dye. Whenever they flowed through the excitation focus, they reduced the fluorescence brightness even when the vessel size stayed constant. To reduce blood-cell-induced fluctuations in fluorescence, we temporally averaged the fluorescence and diameter data (Methods section 2.2.4; 0.33 s moving average for non-capillaries and 5 s moving average for capillaries) and observed the fluorescence brightness to closely reflect the vessel diameter.

This relationship between vessel size and fluorescence brightness provided a simple brightness-based method to detect changes in blood vessel size over an entire volume without the need for image segmentation. As an example, we separated the Bessel imaging volume into 64 × 64 ROIs (with 16 × 16 pixels or 21 μm × 21 μm for each ROI) and cross-correlated each ROI's fluorescence time trace to a reference ROI's time trace. For example, with two distinct ROIs as references (arrows, Fig. 4f, g, respectively), the resulting correlation maps highlighted two vasculature

populations with positively correlated diameter changes within themselves and negatively correlated diameter changes with each other (Fig. 4f, g). The positive correlations likely arose from

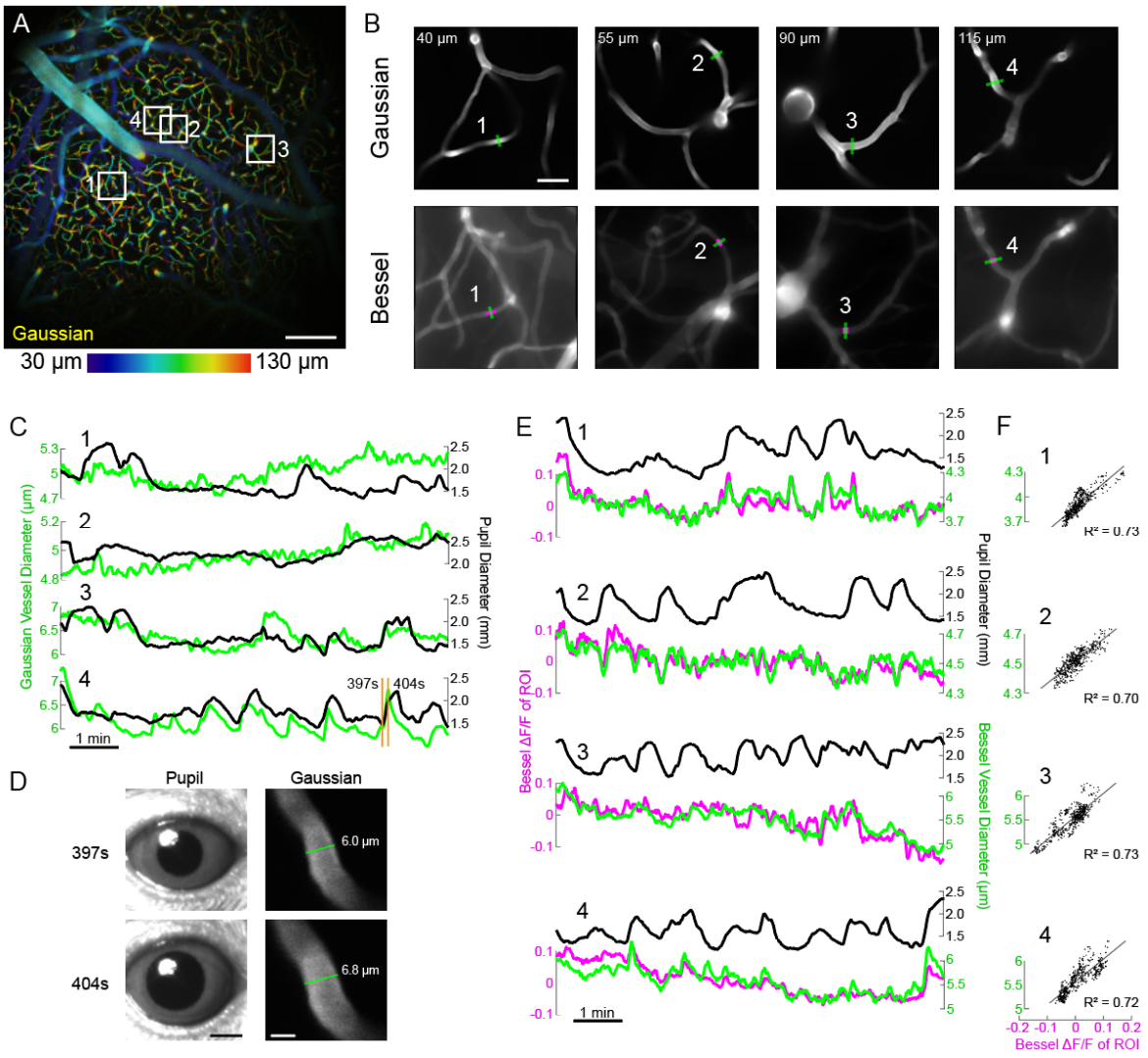

Figure 5. Capillary dilation and constriction probed by Gaussian and Bessel 2PFM.

(A) A 1.4 mm x 1.4 mm x 0.1 mm volume of vasculature imaged with Gaussian 2PFM, color coded by depth. **(B)** High-resolution Gaussian and Bessel images of capillaries. For each area (within the white squares in A), Gaussian images were taken first, followed by Bessel images, both acquired at 30 Hz with 0.2 µm pixel size for 8 minutes. **(C)** Time traces of diameters of 4 capillary segments from Gaussian images in B, plotted with simultaneously measured pupil diameter. **(D)** Example pupil and 1-second averaged Gaussian images of Capillary 4 at two time points (indicated by yellow lines in C) showing changes in pupil and capillary diameters. **(E)** Time traces of fluorescence signal changes and diameters of the same 4 capillary segments from Bessel images in B, plotted with simultaneously measured pupil diameter. Unlike larger vessels whose size correlations with pupil diameter were time-invariant (Fig. 7D), capillaries had time-varying size correlations with pupil diameter over minutes. **(F)** Scatter plot of fluorescence versus capillary diameter data in E. Scale bars: A: 200 µm, B: 20 µm, D: Pupil: 1mm, Gaussian: 5 µm. Post-objective power: Gaussian: 17 mW, Bessel: 112 mW.

the propagation of the dilatory signals along the vessel walls of connected vasculature[47,63,65]. The reference ROI in Fig. 4g had a ΔF/F time trace with a standard deviation 3.6× greater than the reference ROI in Fig. 4f (Fig. 6). Therefore, the ROI in Fig. 4g likely belonged to surface arterioles and the ROI in Fig. 4f likely belonged to venules due to the differing dilatory mechanisms between arterioles and venules[26,41,66]. Pixels with positive correlation with the two ROIs in Fig. 4f and g, respectively, revealed surface venule and arteriole populations. Although the discovery of these two distinct populations was expected, anticorrelated dilatory dynamics of two vasculature populations occupying the same brain volume, to our knowledge, has not been reported before.

Next, we investigated how vasodilation and vasoconstriction were entrained with animal arousal level as reflected by the pupil diameter of the mouse eye. We simultaneously recorded a quietly awake mouse's ipsilateral eye under fixed lighting conditions with an infrared camera (15 Hz, 10 min) and a 1.4 mm × 1.4 mm × 100 µm volume of its brain vasculature with Bessel 2PFM imaging (0–100 µm below the top surface of the dura mater, 15 Hz, 10 min) (Fig. 7a, b). We tracked and extracted the pupil profiles (Fig. 7c, yellow ovals) and observed large spontaneous changes in pupil diameter over the time course of seconds (Fig. 7d, top trace). As there was no

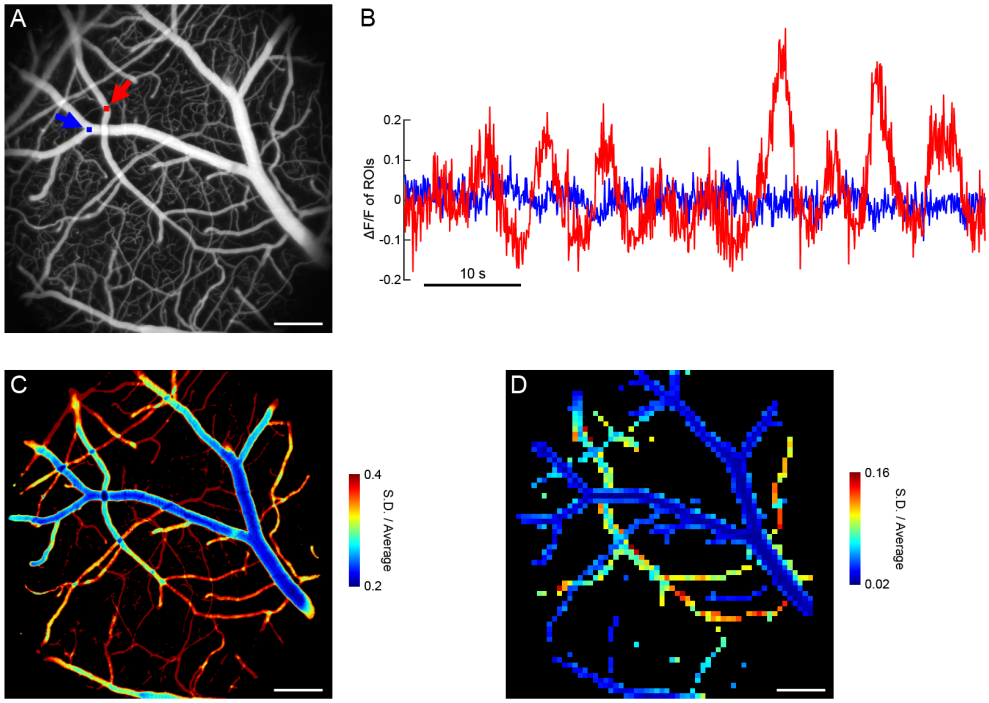

Figure 6. Arterioles exhibited greater changes in Bessel fluorescence signal than venules.

(A) Bessel 2PFM image with the ROIs from Fig. 4F (blue square and arrow) and Fig. 4G (red square and arrow) shown. **(B)** Fluorescence time traces of the ROIs from A showing a large difference in their magnitudes of fluorescence signal change. **(C)** Standard deviation (S.D.) divided by average signal for the brightest 20% of pixels in A (representing vasculature). The dimmest 80% of pixels (representing non-vasculature tissue) are represented in black. **(D)** Standard deviation divided by average signal for the brightest 20% of all ROIs from Fig. 4F, G. Both C and D show a clear distinction between arteriole and venule populations. Scale bars: 200µm for A, C, D.

change in ambient light level, these changes in pupil diameter have been previously shown to reflect the arousal level and/or switching of cortical states[67]. Similar to the analyses performed in Fig. 4f and g, we calculated how fluorescence signal traces of 64 × 64 ROIs were correlated with pupil diameter (Fig. 7e). We observed populations of vasculature whose brightness either positively or negatively entrained to pupil diameter. As indicated by two example time traces (ROIs 1 and 2, Fig. 7d, e), fluorescence signal, and thus vessel sizes according to Fig. 4, exhibited changes either positively or negatively correlated with animal arousal. Based on their location and morphology, ROI 1 and ROI 2 were identified to be a surface artery and a dural arteriole, respectively, with distinct mechanisms regulating their dilation[66]. We noticed that pupil dilation events displayed slower rise and decay dynamics when compared with blood vessel dilation events.

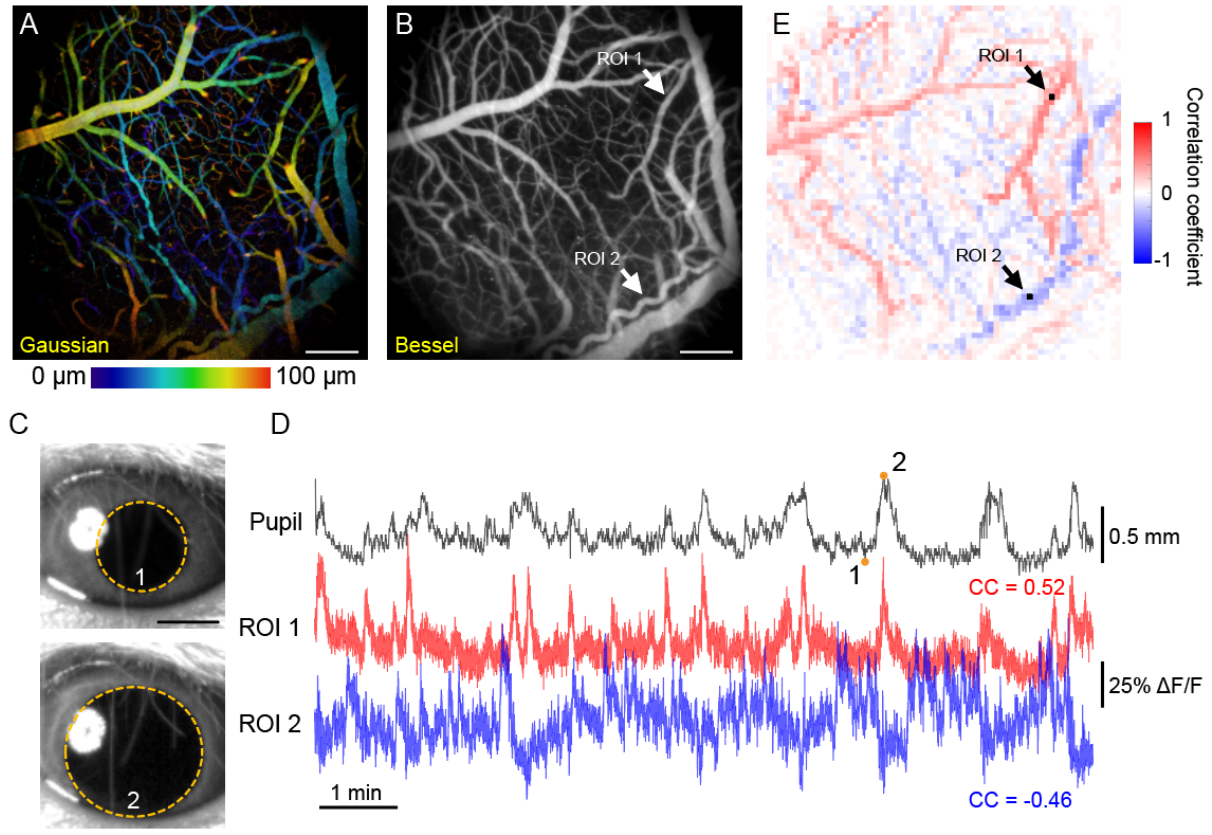

Figure 7. Entrainment of vasodilation and vasoconstriction of a 3D vasculature network with pupil diameter measured by Bessel 2PFM.

(A) A 1.4 mm x 1.4 mm x 0.1 mm volume of vasculature imaged at 15 Hz with Gaussian 2PFM, color coded by depth. **(B)** Bessel 2PFM image of the same volume in A, visualized in grayscale on the normalized square root of fluorescence signal. **(C)** Example pupil images at time points 1 and 2 of the ipsilateral eye acquired concurrently with vasculature imaging. Dashed yellow ovals: pupil profiles automatically segmented from video data. **(D)** Pupil diameter and signal time traces of two ROIs (arrows and black squares in E), showing positive and negative correlation with pupil diameter, respectively. CC: correlation coefficients. Orange circles on pupil time trace indicate time points 1 and 2. **(E)** Map of cross-correlation coefficients between ROIs tiling the FOV in B and pupil diameter. Scale bars: 200 µm for A, B, and E; 1 mm for C. Post-objective power: Gaussian: 47 mW; Bessel: 167 mW.

2.3.5 High-speed volumetric measurement of cerebral blood flow

Finally, we applied Bessel 2PFM volumetric imaging to 3D cerebral blood flow speed measurements in four mice at 99 Hz volumetric rate, an imaging speed fast enough to measure blood flow speeds around 3 mm/s and capture red blood cell (RBC) motion in most capillaries, pial venules, and some pial arterioles[41,42]. As shown for a representative volume (416 µm × 416 µm × 80 µm, 128 × 128 pixels, 0–80 µm below the top surface of the pia mater), Bessel 2PFM was able to record from all vessels and capillaries within the imaging volume (Fig. 8a).

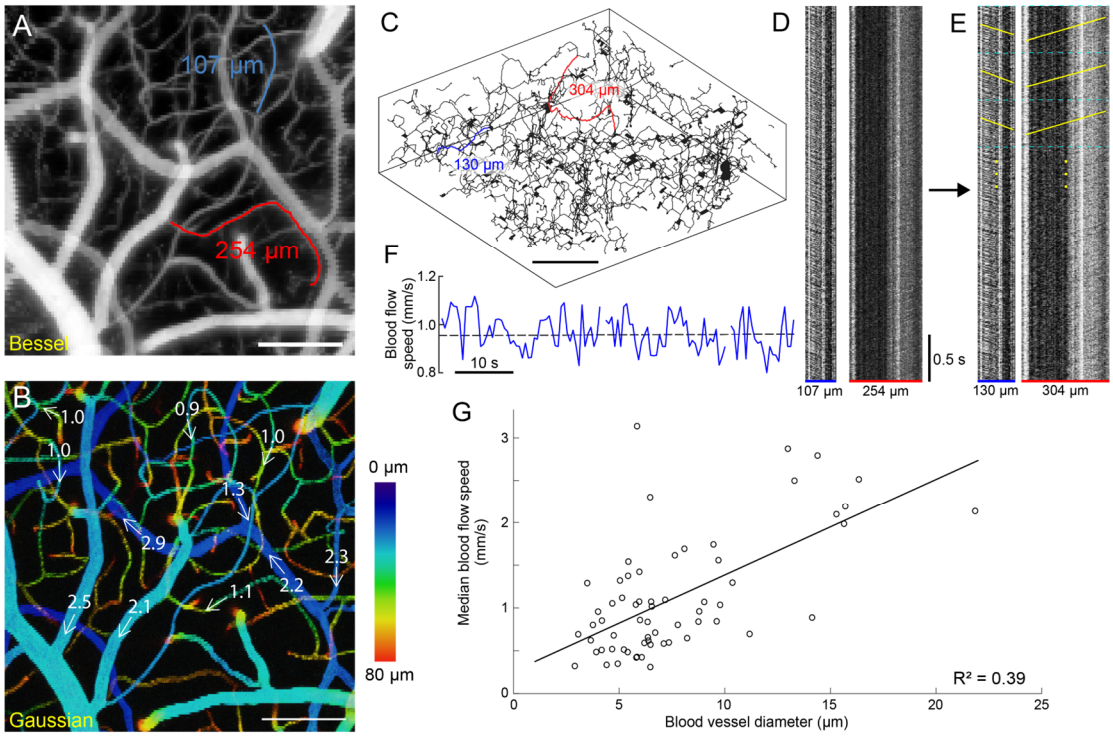

Figure 8. High-speed volumetric measurement of cerebral blood flow speed with Bessel 2PFM.

(A) Bessel image of a 416 µm x 416 µm x 80 µm volume of vasculature that was imaged at 99 Hz with Bessel 2PFM for blood flow speed measurements, with structures visualized in grayscale on the normalized square root of fluorescence signal. Blue and red lines trace two example vessel segments. **(B)** Gaussian image stack of the same volume in A, color-coded by depth and overlaid with median blood flow speeds (in mm/s) of 11 blood vessel segments. **(C)** Skeletonized 3D Gaussian stack from B for the measurements of blood vessel segment 3D lengths. **(D)** Kymographs of two example vessel segments in A, obtained by plotting pixels along the traced blood vessels (horizontal) across time (vertical). Dark diagonal streaks are caused by RBCs traveling along the vessel segment. Note that the horizontal axis represents projected 2D distance. **(E)** Kymographs of the same vessels after nonlinear transformation so that the horizontal axis represents 3D distance. For flow speed measurement, each kymograph was divided into 0.5-second-long blocks (cyan dashed lines, Methods section 2.2.4). Yellow lines represent the distance-time relationship of the blood flow measured for each block. **(F)** Changes in blood flow speed over 1 minute for the blue vessel segment in A. **(G)** Median blood flow speed plotted against blood vessel diameter for 63 vessel segments between 0 and 180 µm below dura, collected from 4 mice. Scale bars: 100 µm for A-C. Post-objective power: Gaussian: 45 mW; Bessel: 217 mW.

We first traced blood vessel segments by hand over the Bessel image (e.g., Fig. 8a, blue and red traces) and then measured their 3D lengths by locating the same segments in skeletonized 3D Gaussian structural data (Fig. 8c, Methods section 2.2.4). In total, we traced 63 vessel segments in seven volumes from four animals (49–549 μm in 3D length, with a median length of 174 μm), of which 28 segments had enough spatial extent along Z to require the use of Bessel focus to measure their blood flow speed. In order to measure blood flow speed, pixels along the traced segments in the Bessel image series were plotted against time and hereafter referred to as kymographs (Fig. 8d). Since the horizontal axes of the kymographs represented 2D-projected vessel lengths, nonlinear transformations were performed on the horizontal axes such that they represented 3D lengths of the blood vessel segments (Fig. 8e). Because RBCs were not labeled with fluorescence, they showed up as dark streaks in the kymographs. From the time required for RBCs to traverse the full length of the segment (i.e., the slopes of the dark streaks in the kymographs), blood flow speed can be calculated. To this end, we applied an automated blood flow speed measurement method based on Sobel filtering and iterative Radon transforms[59] to the kymographs and measured temporally varying blood flow speeds over 1-min-long datasets (yellow lines, Fig. 8e, f). We used the median flow speeds as the representative speeds of the traced vessels (dashed line, Fig. 8f). We overlaid the flow speed on 11 vessels in Fig. 8b to provide a visual representation of flow speeds from the volumetrically distributed blood vessels spanning 80 μm of depth. We plotted the median flow speed against blood vessel diameter for all 63 blood vessel segments and found a positive correlation between vessel diameter and blood flow speed (Fig. 8g), consistent with observations that blood flows faster in larger vessels[31,33,68].

2.4 Discussion

We presented in this study successful fast structural and functional imaging of neurovasculature over large volumes (up to 1.4 mm × 1.4 mm × 110 μm) and at high speed (up to 99 Hz) using a commercially available 2PFM with a Bessel focus module. Scanning the axially extended Bessel focus in 2D enabled us to obtain projected images of 3D volumes, thus drastically increases the volumetric imaging speed and reduces imaging data size. We demonstrated high-throughput tracking of vasodilation, vasoconstriction, and blood flow speed in 3D in the awake mouse cortex.

When Bessel 2PFM was applied to neurovasculature imaging in the mouse cortex, fluorescence intensity proportionally varied with vessel size, thus providing an alternative approach to image segmentation for measuring the dynamics of vessel dilation and constriction. Importantly, this simplified analysis approach combined with the small data size of Bessel 2PFM allowed for fast data analysis using ImageJ and MATLAB without the need for dedicated hardware or optimized software.

By extending the excitation volume axially, a Bessel focus allowed us to measure blood flow in vessels and capillaries that were not parallel to the axis of the Bessel focus. In contrast, in conventional 2PFM imaging with the more axially confined Gaussian focus, many vessels appear only as cross-sections, which makes blood flow measurement difficult. If it is important to measure blood flow from vessels that are parallel with the axis of the Bessel focus, the annular illumination at the back focal plane of the microscope objective can be translated to generate a Bessel focus

traveling along a different direction from the original focus[50,69,70] and a distinct projected view of the vasculature.

In contrast to blood vessel cross-sections captured with Gaussian focus, full length images of blood vessels captured with Bessel focus scanning do not suffer from axial motion artifacts because axial motions several microns in amplitude do not shift the structures out of the extended Bessel excitation focus. Lateral motion artifacts were easily correctable because the fast imaging rates afforded by the resonant galvanometer scanning minimized in-frame non-rigid sample motions. Bessel 2PFM's robustness against motion artifacts is critical for studying hemodynamics in awake animals and would be especially important when working with disease models where motor dysfunctions or seizures cause large sample motion.

Because structures at different depths within the excitation volume appear in the same projected images, Bessel 2PFM performs best with sparsely labeled and high-contrast structures, making it suitable for imaging neurovasculature, which are sparse in the brain and typically labeled with bright fluorescent dyes. With the available laser power and dextran-conjugated Texas Red dye, we were able to image neurovasculature up to 800 μm below the brain surface for conventional Gaussian 2PFM and 600 μm for Bessel 2PFM. The reduced imaging depth of Bessel 2PFM was partly due to the higher fraction of excitation energy distribution in the side rings of the Bessel focus[57], leading to less effective two-photon excitation for the same post-objective laser power. The excitation energy in the side rings also reduces the image contrast and lowers the signal-to-background ratio (SBR). To image vasculature structures at depth, more average power needs to be deposited into the mouse brain with Bessel 2PFM than Gaussian 2PFM. However, the highest average power utilized in this study (up to 217 mW) was under the threshold for heating-induced damage in the mouse brain *in vivo*[71] and below the average powers that were utilized in other high-speed brain imaging technologies[72,73].

Besides increasing laser power, improvements in neurovasculature imaging depth can be accomplished by using longer-wavelength excitation, because scattering mean free path increases with longer-wavelength photons[74]. For example, indocyanine green is two-photon excitable with 1700 nm light and was used to image vasculature down to 2 mm with Gaussian excitation[75]. Three-photon fluorescence excitation using Bessel foci also employs longer-wavelength excitation light and has the added benefit of suppressed side-ring fluorescence excitation due to the higher non-linear process[54].

Bessel beam imaging depth can also be improved by adaptive optics[76,77], a method which corrects for optical aberrations of the imaging-forming excitation light introduced by the brain tissue. We observed distinct effects of optical aberrations caused by large surface vessels for Gaussian and Bessel foci. Large surface vessels aberrated the Gaussian focus and led to reduced excitation efficiency and thus dark shadows in the Gaussian image stacks (Fig. 2e, f). In contrast, large surface vessels degraded spatial resolution and signal-to-background contrast in Bessel image stacks (Fig. 2h, i) suggesting that aberrations in the Bessel focus led to asymmetric focal energy distribution but not a decrease in the overall two-photon excitation efficiency. Removing these sample-induced aberrations would improve excitation efficiency and resolution, which in turn would increase SBR and thus imaging depth.

Even without the improvements outlined above, the current implementation already allowed us to apply Bessel 2PFM to monitor hemodynamics in 3D at capillary resolution. We observed vasodilation and vasoconstriction in superficial blood vessels[78–80] both directly by measuring vessel diameter changes and indirectly through Bessel focus excited fluorescence signal. We observed size changes in some capillaries, which may be regulated by the flow in nearby arterioles or due to active control by more proximal factors such as pericytes[64,80–82]. We observed two vasculature populations negatively correlated with one another in terms of their dilation/constriction dynamics, possibly distinguishing between arterioles and venules. We also observed entrainment of brain hemodynamics to pupil diameter, a phenomenon that was reported in the past using ISOI[83,84]. Since pupil diameter is closely tied to brain arousal levels[85–87] and cortical states[67,88], this entrainment of vessel and pupil dilations reflects underlying neural activity dynamics including the release of vasoactive neurotransmitters[89]. We noticed faster temporal dynamics in vessel size changes than pupil diameter changes, which to our knowledge have not been directly compared in literature. However, this observation is consistent with previous reports that neurovasculature responds to neural activity on sub-second timescales[39,63] while the pupil responds on the scale of seconds[88].

In addition to vasodilation and vasoconstriction, we also used Bessel 2PFM to measure blood flow speeds in 3D at 99 volumes per second from both dural and cortical vessels as well as capillaries. Following the calculations by Shih et al.[41], we estimated the upper bound of RBC flow rate that can be captured at this speed to be 4.3 mm/s, faster than the flow rates of most neurovasculature[41,42]. Compared with previous studies using line scan paths to simultaneously measure blood flow speed in multiple vessel segments which does not scale well with the number of features[90,91], Bessel focus scanning could record from all blood vessels in an imaging volume. To capture even faster blood flow rates if needed, volumetric imaging exceeding 100 Hz can be achieved by using faster optical scanning[8,92], imaging smaller volumes, or sampling at a lower pixel density. Improving SBR by methods described above would become essential when the achievable imaging speed becomes limited by fluorescence signal strength.

Bessel 2PFM enables volumetric imaging of neurovascular dynamics without sacrificing the high lateral resolution and multi-color imaging capability of Gaussian 2PFM. With the developments of bright and efficient two-photon excitable fluorescent sensors for neural and glial activity reporting[93], Bessel 2PFM can simultaneously image neurovasculature with neurons and glia to generate high-throughput, rich datasets for uncovering the detailed dynamics of neurovascular coupling in healthy and diseased brains[78]. Vascular imaging with Bessel 2PFM can also be applied to other vasculature systems such as those in the retina, spinal cord, or skin.

2.4.1 Studying preclinical models using Bessel 2PFM

Enabled by the accessibility of the Bessel 2PFM technique, either through a commercially available system or a cost-effective home-built system[53], researchers can ask new clinically-relevant questions in the neurovasculature field. Blood-brain barrier (BBB) breakdown has been studied using conventional 2PFM and have been linked to both physical[94] (traumatic brain injury, TBI) and neurological sources[34,95]. Vasculature leakage as reported by small molecule fluorescent dyes typically occur seconds to minutes after the injection of dyes or introduction of the leak in

the case of TBI models. During these short time scales, only a certain number of imaging frames could be captured, so Bessel 2PFM would greatly increase the throughput for these time-sensitive experiments.

Another body of literature focused on imaging blood flow through blood vessels, especially capillaries, to observe changes during TBI[96,97], ischemic stroke[32,33], and neurological diseases[33,37]. These studies, which typically observed reduction and/or turbulence in capillary blood flow in diseased animal models, would benefit from the ability to image larger numbers of vessel segments at once. Due to the low throughput of conventional 2PFM for imaging blood flow, small vessel segments were typically imaged and treated as independent samples for analysis. Yet just observing the slowing blood flow of the damaged vessels is not enough to understand how neighboring vessels adapt to the changes in flow and the redundancy in the vascular system. How can treatments improve the speed of this adaptation process to minimize brain damage? Bessel 2PFM opens the opportunity to record simultaneous blood flow in highly interconnected vasculature systems, allowing for relationships between vessels to be observed in both healthy and diseased models.

Chapter 3: A commercial Bessel & Bessel-droplet two-photon fluorescence microscope with modal adaptive optics

The study presented in chapter 2 introduced a commercial 2PFM system capable of both Bessel beam and conventional Gaussian beam imaging[23]. Since the publication of this study, two new technologies have been introduced that directly improve the Bessel 2PFM method. The first technique, Bessel-droplet 2PFM, utilized two concurrently generated Bessel beams which allowed for higher NA Bessel beam imaging with reduced background contamination from side rings[98]. The second technique, Bessel beam adaptive optics, performed aberration correction for improved excitation efficiency and resolution at greater imaging depths[99]. Both original studies were conducted using a state-of-the-art custom-built two-photon fluorescence microscope with specialized optical components not found in commercial systems. The goal of this chapter is to incorporate the two new technologies into a commercial Bessel 2PFM system such that researchers can enjoy the benefits of these new methods with minimal changes to their microscope and imaging workflow.

3.1 Improving image quality through Bessel-droplet 2PFM

The lateral PSF of a Bessel focus has much more pronounced side rings than that of a Gaussian focus[57], especially at higher NA[52]. This is because different equations dictate their lateral PSFs: the lateral PSF of a Bessel focus is dictated by a Bessel function of the first kind, as originally calculated by Rayleigh. Side rings not only take away laser power from the central peak resulting in lower peak brightness, but also create a "halo" effect that is especially apparent when imaging small structures[98]. However, the central peak of the Bessel focus lateral PSF is narrower than that of the Gaussian focus which means the Bessel focus has a higher lateral resolution compared to the Gaussian focus at the same NA. The quick-fix solution to the side ring problem was therefore to stop down the Bessel focus NA, such that the lateral resolution was still comparable to that of a high-NA Gaussian focus while at the same time having manageable side rings[52].

Recently, an alternative solution to the side ring problem, coined Bessel-droplet, has emerged which allowed for high-NA Bessel 2PFM with reduced side rings, enabling Bessel-droplet two-photon volumetric imaging to be both faster and higher-resolution than its Gaussian counterpart. A detailed explanation and discussion around Bessel-droplet beam generation can be found in the original study that demonstrated this technology for two-photon *in vivo* imaging[98]. In brief, like how a single Bessel beam is generated, two Bessel beams, one at approximately half the NA of the other, were generated by the same SLM and spatially filtered with a concentric double annular ring mask. The lower-NA Bessel beam was chosen to, as best as possible, cancel out the first side ring of the higher-NA Bessel beam, which resulted in a 7 to 8-fold reduction of side ring signal. A side-effect of interfering two Bessel beams was the creation of a sinusoidal illumination pattern in the axial direction, thus the "droplet" name. One can then generate two Bessel-droplet beams, one with the inner and outer annular rings in phase and the other at π out of phase, which focuses the axial droplets π-offset from each other. Scanning the 3D sample with one beam after the other and summing the fluorescence signals recovers the axial information that would have been lost to a single Bessel-droplet beam.

Using a home-built two-photon fluorescence microscope with accurate scan optics and perfect conjugation of optical components, high-resolution, high-contrast video-rate volumetric imaging was performed on both neurovasculature and neuronal processes *in vivo*[98]. Given the clearly

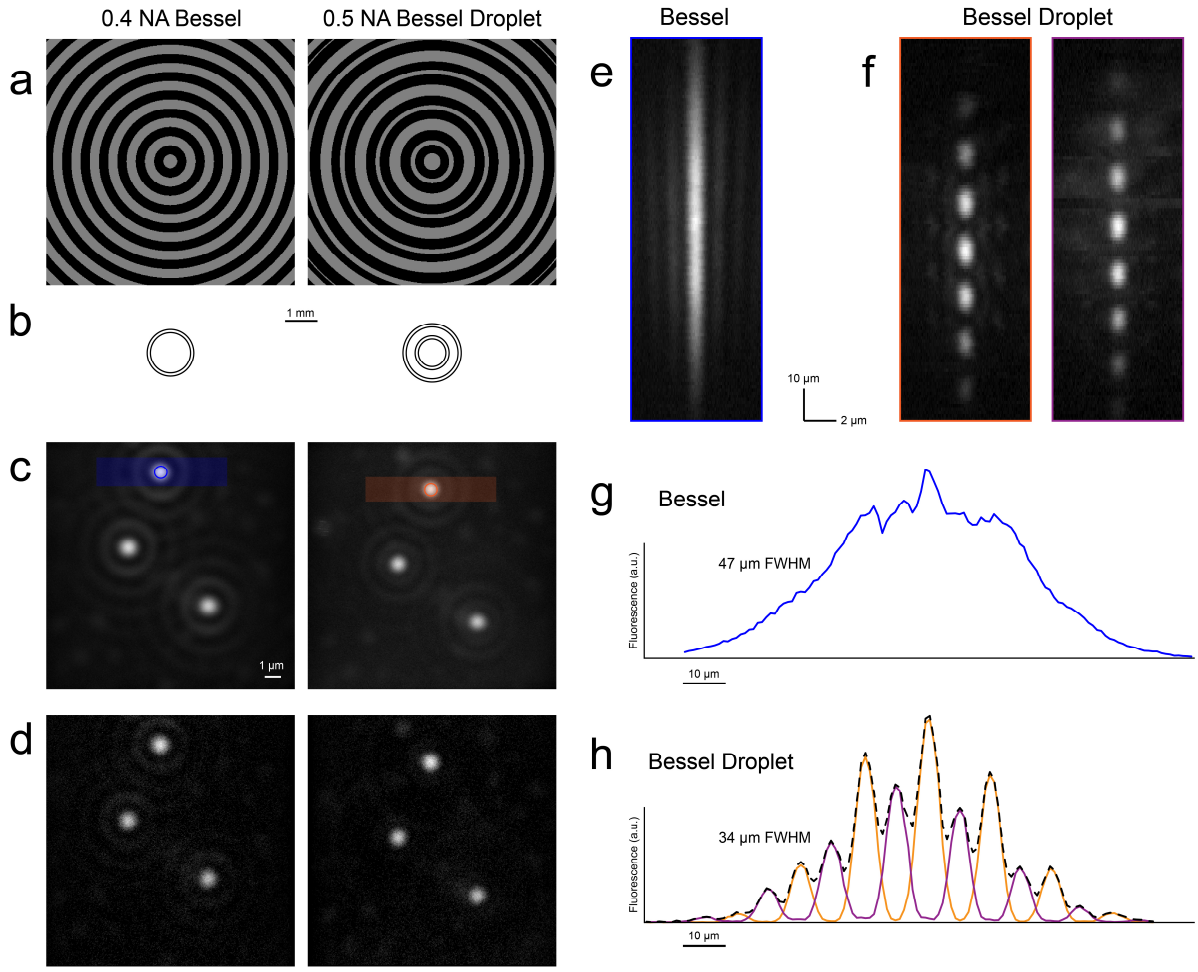

Figure 9. Bessel-droplet two-photon fluorescence microscopy with a commercial microscope system.

(A) 0.4 NA Bessel and 0.5 NA Bessel-droplet patterns displayed on the focal plane SLM for Bessel focus generation. Scale bar represents actual size of pattern displayed on the SLM. **(B)** Pupil plane mask patterns for Bessel and Bessel-droplet, at the same scale as A. **(C-F)** All fluorescence images are plotted using the square root of intensity for better visualization of dim features. **(C)** Mean two-photon intensity X-Y projections of 0.5 µm beads, imaged using Bessel and Bessel-droplet foci. Colored circles represent ROIs used to generate axial intensity plots. Shaded rectangles represent XY projection regions. **(D)** 5-frame averaged images at Bessel and Bessel-droplet's respective planes of peak brightness, showing a large difference in side lobe fluorescence. **(E,F)** Bessel and Bessel-droplet XZ projections of the shaded volumes in C. Purple-bordered image is an XZ projection of a π-offset Bessel-droplet focus. **(G)** Mean axial intensity plot from the blue circle in C, showing a Bessel axial FWHM of 47 µm. **(H)** Mean axial intensity plot from the orange circle in C and the π-offset focus in purple (XY projection not shown), showing axially-π-offset droplet positions. The sum of the two axial intensities is shown in the dotted black trace and has a FWHM of 34 µm.

demonstrated benefits of Bessel-droplet 2PFM, we sought to apply this technique to the commercial Bessel 2PFM detailed in chapter 2. The commercial microscope system, in contrast to the home-built system, does not have perfectly conjugated X and Y-axis galvanometer mirrors and is less precisely aligned, leading to larger system aberrations. It was therefore unclear whether Bessel-droplet 2PFM would perform well in these conditions.

Pairs of Bessel beams were simulated in MATLAB software, originally developed by Dr. Wei Chen[98], to find specific annular ring diameters and thicknesses which result in maximal destructive interference of side rings. Bessel-droplet parameters were then backpropagated to the SLM plane and quantized to the resolution of the SLM (8-bit, 512 x 512 pixels). Double annular ring masks were fabricated by a photomask company (Photo Sciences, Inc.) on quartz and gold, the latter used for its high reflectivity at NIR wavelengths. Masks were designed for two objective lenses: the 16x 0.8 NA Nikon objective, and the 25x 1.05 NA Olympus objective. Bessel-droplet masks in a range of NAs were fabricated to test the effectiveness of Bessel-droplet generation and side lobe reduction at different NAs. We characterized the PSFs of the imaging system in Bessel and Bessel-droplet modes with 0.5-μm-diameter fluorescent beads (Fig. 9). Mean projection images of the bead showed the presence of side lobes in both Bessel and Bessel-droplet (Fig. 9c), but side lobes were less apparent at Bessel-droplet peaks (Fig. 9d). The square root of fluorescence brightness was shown for easier visualization of the dim side lobes. X-Z mean projection images reveal that side lobes for Bessel-droplet beams alternated between bright and dim and was dimmest at droplet peaks (Fig. 9f), which was predicted in simulation[98]. Bessel-droplet beams π-offset in phase generated droplets offset in the axial direction, such that the summation of the two recovered a continuous axial profile (Fig. 9h). The combined Bessel-droplet envelope had a FWHM smaller than that of the Bessel beam, which was expected since the Bessel-droplet beam had higher effective NA than the Bessel beam. We quantified side ring contamination by measuring the ratio between the first side ring and the central peak's integrated fluorescence signals. At the z-position of peak brightness, 0.4 NA Bessel had a ratio of 0.27 while 0.5 NA Bessel-droplet had a ratio of 0.096, which was 2.8x less side ring contamination.

Further work will include characterizing Bessel-droplets of other NAs and objective lenses. With our characterizations demonstrating a functional commercial Bessel-droplet 2PFM system, we look forward to this system being used by future experimentalists who require fast volumetric imaging at high resolution in opaque biological samples.

3.2 Removing aberrations in 2PFM using adaptive optics

Signal contamination from Bessel beam side rings is not the only barrier to achieving high resolution, high contrast two-photon imaging in opaque tissue. Aberrations in the optical path, from laser source to sample plane, reduce image quality in Gaussian, Bessel, and Bessel-droplet 2PFM, albeit to different degrees of severity[98,99]. Especially unpredictable are the aberrations within opaque tissue samples, such as the mouse brain, which can vary by animal, region, and depth. As a result, true diffraction-limited resolution can rarely be achieved at high NA, even with advanced home-built microscopes. The technique of adaptive optics[76,77,100] (AO) for 2PFM sets

out to solve this problem, through measurement and subsequent hardware correction of aberrations in both the imaging system and sample.

Aberration measurement involves the acquisition of the combined wavefront error of the system and sample. This can be most simply achieved with a Shack-Hartmann (SH) direct wavefront sensor, a technology inherited from the astronomy field to measure earth atmospheric wavefront error[101,102]. This method of direct wavefront measurement involves a "guide star", a name also inherited from astronomy, which is a lone, bright point object at the sample plane. This guide star, when measured with the SH sensor, provides a map of the accumulated wavefront error between the two planes. This is achieved at the SH sensor with a micro-lens array and camera sensor, which collects information on the phase slopes of all wavefront segments with a single acquisition. Unfortunately, unlike the night sky, which is typically clear during the measurement of atmospheric wavefront aberration, biological samples such as the mouse brain often strongly scatter light, preventing direct wavefront sensing from being applied with fluorophores in the visible spectral range.

Alternatively, indirect aberration measurement methods exist which do not require a guide star, a dedicated SH sensor in the optical system, nor a transparent sample, at the cost of longer measurement times and higher computational complexity. Thankfully, unlike earth's turbulent atmosphere, still biological samples have minimal time-varying aberrations, so the speed of SH sensors can be sacrificed for gains in sample and system simplicity. One method of indirect aberration measurement involves a similar approach to that of the SH sensor, where the phase slopes of wavefront segments, or zones, are individually measured by illuminating the zones serially and observing the lateral displacement of a sample object[100]. Alternatively, instead of measuring the lateral displacement of a sample object which requires a 2D image, one can perform a point measurement of the sample fluorescence while modulating the tip and tilt of a zone to find the corrective angle in which the zone produces the brightest signal. This method can be further sped up by measuring many zones at once through signal multiplexing in Fourier space[103,104]. Both methods of indirect wavefront measurement belong to the category of "zonal" AO.

Once aberrations have been measured either directly or indirectly, correcting for them is as simple as presenting equal but opposite aberrations at the pupil plane, called the corrective wavefront, to pre-correct aberrations that will be picked up as the laser passes through the system and sample. Presenting the corrective wavefront is a piece of programmable hardware, either a deformable mirror (DM) or a spatial light modulator (SLM) that modulates the phase of wavefront segments. DMs are fast and therefore ideal for multiplexed zonal AO but have fewer addressable segments, whereas SLMs are slower but have many addressable segments with modern SLM pixel arrays exceeding 1 megapixel[105]. Both options have been shown to perform successful AO on biological samples to rescue diffraction-limited resolution and signal contrast in conventional gaussian 2PFM[100,104].

Although system and sample aberrations can be measured independently of pupil illumination methodology since aberrations are a product of imperfections of the optical path, Bessel beam AO requires an additional step during wavefront correction. Instead of applying the corrective wavefront at the pupil plane, the wavefront is backpropagated and applied to the focal plane-

conjugated SLM that generates the Bessel beam[99]. Focal plane AO performs favorably to pupil plane AO for Bessel beams, due to better correction accuracy for both phase and amplitude errors, rather than only phase errors. Uncorrected amplitude errors have a largely imperceptible effect on the focal quality of a gaussian beam due to the large back pupil illumination area. However, the same errors are detrimental to Bessel beam due to the much smaller-area ring illumination and the need for a specific electrical field amplitude distribution to generate a high-quality Bessel focus. Conveniently, focal plane AO reduces hardware complexity for Bessel beam wavefront correction, since the same SLM that generates the Bessel beam also corrects its aberrations. Unfortunately, the measurement of aberrations still requires additional hardware at the pupil plane, as outlined earlier in this section.

3.3 Indirect wavefront measurement at the focal plane using modal reconstruction

Indirect wavefront measurement methods share a common methodology of splitting a wavefront into an orthogonal set of unknowns, determining the value of each unknown via measurements of the sample, then reconstructing the wavefront from the orthogonal set. In zonal AO, the orthogonal set of unknowns are zones of the wavefront, typically selected to correspond to individual mirror segments of the DM, each of which has independent phase slopes. Similarly, “modal” AO uses an orthogonal set of polynomial modes that span the full wavefront area, in essence decomposing the wavefront into modes, rather than zones. Any set of 2D orthogonal polynomials can be used for modal reconstruction, but most common are the Zernike polynomials when relating to wavefront aberrations at a circular pupil plane. Unlike zonal AO, modal AO relies on the accuracy of adding 2D polynomials to a wavefront, so it benefits greatly from the high pixel count of a SLM.

The methods for modal AO closely mirror that of zonal AO. A Zernike mode is presented on the SLM at different amplitudes, or coefficients, and the brightness of a sample is measured each time. The optimal value of the Zernike coefficient corresponds to the one that generates the brightest sample. After the coefficients are measured for many Zernike modes, the sum of the weighted Zernike polynomials is the corrective wavefront. Whereas the time needed for zonal wavefront measurement is determined by the number of DM segments and the speed of the DM, the time needed for modal wavefront measurement is determined by the number of modes to be corrected and the refresh rate of the SLM. For high-order Zernike modes, changes in fluorescence signal may become too small to distinguish from noise.

When applied to Bessel beams, modal AO does have one critical advantage over zonal AO: like the corrective wavefronts in focal plane AO, 2D Zernike modes can be backpropagated to the Bessel beam-generating focal plane SLM. This means that, in theory, Bessel AO using modal reconstruction can both measure and correct wavefront aberrations solely using the focal plane SLM already present in the commercial Bessel 2PFM system without the need of additional pupil-plane hardware. However, such an all-focal-plane implementation of modal AO has not been attempted to our knowledge.

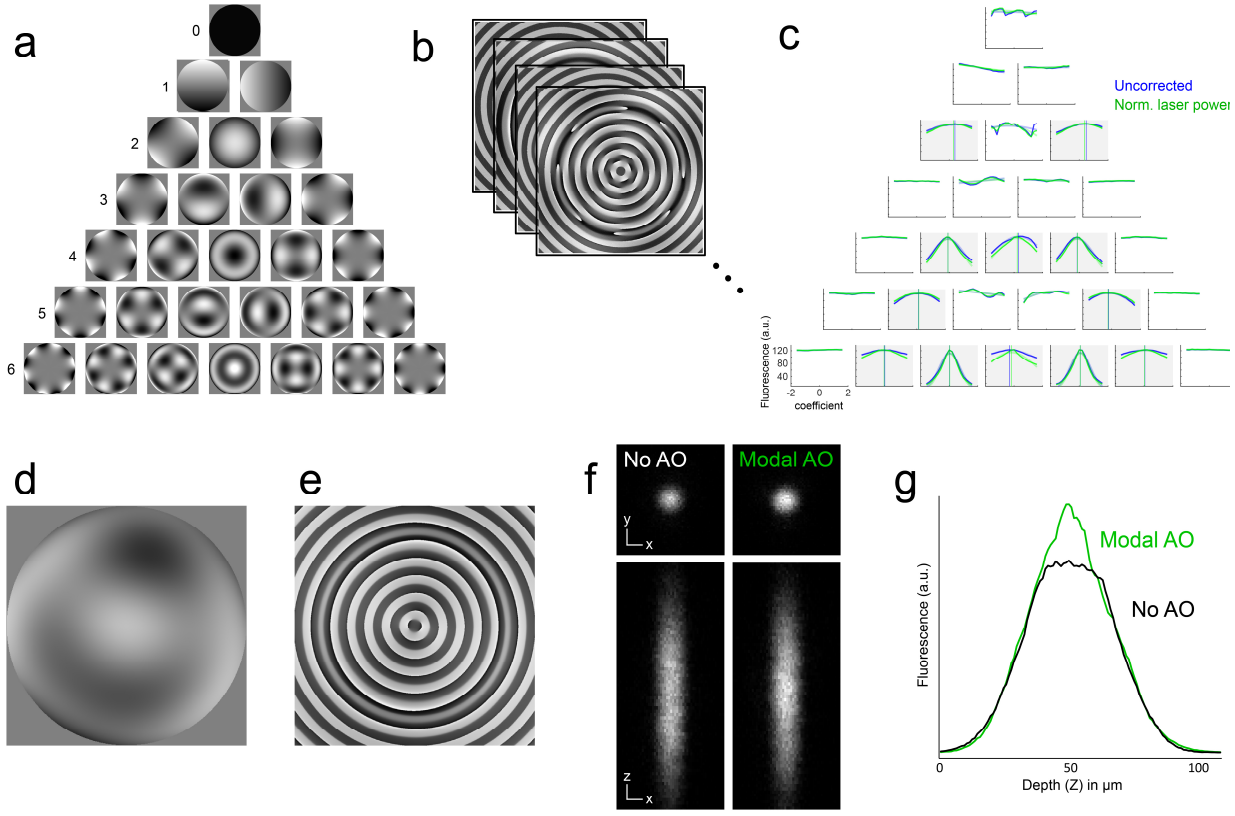

Figure 10. Bessel beam modal-based AO reduces system aberrations.

(A) Generated Zernike modes up to the 6th order, from coefficients of -2 to 2. Pictured are modes with coefficient = 1.4. **(B)** An SLM pattern is generated for each Zernike mode and coefficient value and is serially presented as the fluorescence intensity of a 2 µm bead is imaged. **(C)** Mean fluorescence intensity of the center of a 2 µm bead in the presence of Zernike modal aberrations are plotted in blue. Subplot positions correspond to the Zernike modes in A. Green traces are fluorescence intensities normalized to the post-objective laser power. Light blue and light green shaded lines are fitted Gaussian curves to the blue and green fluorescence traces, respectively. Vertical green and blue lines are the peak positions of the fitted Gaussian curves, representing the fitted correction coefficients for the specific Zernike modes. Light grey-shaded plots are ones with confident Gaussian fitting and therefore the modes used to reconstruct the corrective wavefront. **(D)** Corrective wavefront shown is reconstructed from coefficients fitted to the power normalized fluorescence intensities (green) in C. **(E)** SLM pattern introducing the corrective wavefront in D. **(F)** 2 µm bead XY and XZ mean intensity plots imaged using an SLM pattern with a flat wavefront (No AO) and using the SLM pattern from E (Modal AO). Plotted on the same brightness scale, Modal AO peak brightness at the center of the bead is slightly higher. **(G)** Mean axial intensity plot of the data from F, showing a 30% increase in peak intensity after modal AO correction. Note that the axial extents of the Bessel beams remain very similar.

3.4 Bessel beam adaptive optics using modal reconstruction reduces system aberrations

We set out to test whether modal AO can be applied to focal plane aberration correction of Bessel foci in our commercial Bessel 2PFM system, which only has one SLM used to generate the Bessel beam (Fig. 1a). Using the same MATLAB software which backpropagates a corrective pupil wavefront onto a focal plane SLM[99], we generated a collection of SLM patterns which add known magnitudes of Zernike modes to a Bessel beam-generating grating (Fig. 10a,b). We tested up to 6 orders of Zernike modes (28 polynomials total) and coefficients ranging from -2 to 2 waves with a step of 0.2. Next, we serially presented every SLM pattern and measured the corresponding brightness of a 2 μm bead, while also measuring the corresponding post-objective laser power (Fig. 10c). Measurement of post-objective laser power is important due to the varying throughput of the SLM for different patterns. This is because, despite the SLM being linearly calibrated for $0 – 2\pi$ phase shifts, phase wrapping and other sharp gradients in the SLM pattern result in phase errors caused by pixel crosstalk, reducing SLM efficiency. After post-objective laser power correction of bead brightness, gaussian-fitted peaks for each Zernike mode determined its ideal corrective coefficient (Fig. 10c). A subset of fitted Zernike modes were used in the reconstruction of the corrective wavefront (Fig. 10d). Some Zernike modes which had poor fitting due to weak intensity modulation of the bead were not used in the reconstruction. Weak modulation could be due to low system aberrations at those modes. It could also be that the bulk of the mode pattern lied outside of the area of the 0.4 NA Bessel annular mask, which underfilled the 1.05 NA back pupil. The reconstructed wavefront was then spatially filtered with the annular mask pattern at the pupil plane, followed by backpropagation to obtain the phase pattern on the focal plane SLM (Fig. 10e). This phase pattern therefore both generated a Bessel focus and compensated for the measured aberrations. For a 2 μm fluorescent bead imaged without and with AO (Fig. 10f), we saw a 30% increase in its peak brightness with our all-focal-plane Bessel AO method (Fig. 10g).

Our observation of a mild peak brightness increase is likely due to the relatively low amount of system aberration in the microscope. Further tests in more aberrated environments, such as in opaque brain tissue, is needed to validate this AO method. Low-order aberrations commonly found in microscope systems and biological samples disproportionately affect the brightness of smaller structures[76]. A next step should be to validate this technique with smaller bead sizes and/or small biological structures such as neuronal synapses.

3.5 Discussion: towards an automated Bessel-droplet and AO software solution

We have demonstrated in this chapter compatibility of two next-generation Bessel 2PFM methods, Bessel-droplet and Bessel AO, with an existing commercial Bessel 2PFM system. However, further development is required for these methods to be accessible to experimentalists and incorporated seamlessly into an existing Bessel 2PFM workflow.

Currently, Bessel and Bessel-droplet annular ring masks are mounted in the microscope via a manual 3D translational stage for precise alignment after mask-switching. The switching and subsequent alignment of a mask takes 10 minutes for an experienced user. Although suitable for

testing the performance of mask designs, an automated approach would be preferred for a final commercial system. For example, an array of masks on a rotating stage can be used, much like a filter wheel, to provide the microscope user with options for both Bessel and Bessel-droplet masks of different NA and different objective lenses. If precise positioning of each mask on a rotating stage proves to be difficult, a motorized x-y stage can add the functionality of automatic alignment: x and y positions of the mask are tweaked to maximize laser throughput, read out via a post-mask photodiode. This results in an inexpensive, fully automated mask-switching method which, together with the automatic beam path-switching mechanism (Fig. 1a, Methods section 2.2.1), relieves the end user from needing to service the Bessel beam path.

Bessel-droplet foci, which are discontinuous in the axial dimension, require two 2D scans to sample the same volume as a single 2D scan of Bessel foci. The two scans use different SLM patterns: one that generates a pair of annular rings in phase at the pupil plane and one that generates them in opposite phases. Current commercially available SLMs can switch patterns in as quickly as 2-5 ms[105], which would only fractionally slow down a microscope equipped with a resonant galvanometer imaging at 15-30Hz volumetric imaging rate. This makes Bessel-droplet suitable for imaging slower dynamics such as calcium activity and vasodilation, at half of the volumetric imaging rate as Bessel 2PFM. New fluorescence sensors for glutamate[106] and voltage[7,107] imaging, as well as high-speed blood flow[108], require imaging speeds of 100-1000 Hz which would be difficult to achieve with SLMs, which are limited by the dynamics of liquid crystal molecules. Without the development of faster SLMs, temporally demanding imaging conditions cannot utilize Bessel-droplet, unless the researcher accepts a loss of half of the structural information in the imaging volume. Alternatively, if the researcher is interested only in larger structures such as cell bodies, a Bessel-droplet focus with inter-droplet-distance less than the size of the structures can be used, with the caveat that smaller inter-droplet-distances result in shorter total axial extent and therefore smaller imaging volumes. The process of communicating precise acquisition timings with the SLM, and generating SLM patterns, can be incorporated into future two-photon imaging software, resulting in simple software controls to perform Bessel-droplet imaging using various hardware and data acquisition parameters.

Using all-focal-plane modal AO, we corrected system aberrations in a commercial Bessel 2PFM system. AO corrections in more aberrated *in vivo* environments are needed to validate this method for brain imaging. Simply as a system aberration correction tool, modal AO will improve spatial resolution and contrast in almost all samples, especially flat, thin, or clear ones that match the refractive index of the objective immersion fluid. As a system and sample aberration correction tool, many thicker samples of uneven refractive index, such as the *in vivo* mouse brain, can potentially be imaged at drastically improved resolution and contrast, allowing for *in vivo* imaging of deeper structures inaccessible via non-AO methods. In our modal AO validation experiment, a fluorescent bead was used, but in the absence of bright point objects *in vivo*, the brightness of larger structures such as cell bodies can be used instead, as demonstrated in zonal AO approaches[103,104]. In more aberrated environments, wavefronts can contain higher order Zernike modes and/or larger Zernike coefficients. As a result, it is possible that for such environment, a larger set of Zernike modes is necessary to reconstruct an accurate corrective wavefront. We can

consider using tailored modal test sets for each sample type to minimize AO time for less-aberrated samples and maximize AO accuracy for more-aberrated ones.

Efficient test set sampling can further speed up the modal AO process. Bessel beams are more resilient to many aberration modes when compared to conventional Gaussian beams due to their symmetry[99]. Those aberration modes, which are easily identified due to their minimal effect on sample brightness when introduced to Bessel beams (Fig. 10c), can be omitted from the modal test set. Furthermore, with more samples tested, we may notice that a smaller range of coefficients are sufficient for certain aberration modes, whereas a large range of coefficients may be needed for others. For example, samples such as C. Elegans have intrinsically strong astigmatic aberrations due to their cylindrical shape.

In our modal AO validation experiment, post-objective laser power was measured concurrently with bead brightness to correct for differences in SLM efficiency in a post-processing step. This type of SLM calibration only needs to be performed once for each modal test set since it is sample-independent. Laser power measurement can also be measured at any point after the annular mask, so one photodiode can be used for both automatic mask alignment, as suggested above, and SLM efficiency normalization. Performance of next-generation commercial SLMs looks to improve considerably[105], but real-world testing will validate the usable frame rate of new SLMs. A higher SLM frame rate both increases the maximum imaging speed for Bessel-droplet 2PFM and speeds up measurements for Bessel AO. Unfortunately, new technology can also represent higher cost, which could be prohibitive for an accessible, commercial microscope system.

This chapter has shown that, with limited modifications to the hardware and software of the existing commercial Bessel 2PFM system, Bessel-droplet and AO methods can be incorporated into current Bessel-compatible experiments to improve the quality of collected data. Software can be as simple as a single click without sacrificing functional effectiveness, as suggested above. Finally, Bessel-droplet AO is a natural extension given the existing methods and will share its methods with modal-based Bessel AO.

Chapter 4: Interaction of sensory stimuli and cortical electrical stimulation in the awake mouse brain

4.1 Introduction

In contrast to using concepts in physics to improve 2PFM in chapters 2 and 3, we can pair 2PFM, an optical method, with an electrical method to ask new preclinical questions. In this chapter, we explore the methods of combining 2PFM with brain-surface electrical stimulation. With 2PFM's cell-type specific neural response data, we explore the modulating effects of electrical stimulation on the cortical microcircuit. The resulting scientific findings show clear benefits of our methods for answering translational questions pertaining to cortical electrical stimulation.

4.1.1 Cortical electrical stimulation therapy is a promising clinical field

Neurological disorders are pervasive in society and are becoming more at the forefront of study than ever before, yet treatments are few and far between due to the complexity and mystery of the brain. Pharmacological treatments can be used for some disorders to varying degrees of success, such as Alzheimer's disease (AD) and major depressive disorder (MDD), where certain symptoms of the disorder relate to isolatable biochemical targets[109–111]. Unfortunately, efficacy changes from case to case, and only symptoms, not the underlying disease, can be treated at this time[110,112]. Some neurological disorders such as Parkinson's Disease (PD) and MDD can be treated through continuous, nonspecific electromagnetic perturbation of the nervous system using a medical device, such as DBS[16,17,113,114] or transcranial magnetic stimulation (TMS)[115,116]. Many more neurological disorders have complicated biology that do not lend well to existing drug nor device treatments. Tackling these disorders requires both the understanding of the underlying biological mechanisms that cause them and the development of novel treatment methods to rescue healthy behavior. One promising implantable device for the treatment of neurological diseases is the electrocorticography (ECoG) array, a flexible sheet of electrode contacts placed on the surface of the brain capable of recording neural activity. ECoG arrays are routinely used in the operating room during epileptic surgery for the localization of seizure focus. During the operating procedure, these electrode arrays have been increasingly used as a scientific research tool[117–122].

Beyond their usage as acute recording tools, ECoG devices can also be chronically implanted and write to the brain using electrical stimulation. A primary benefit of the ECoG array is its minimal invasiveness, as it sits on an intact pia and doesn't penetrate the brain surface. As a result, ECoG arrays have been demonstrated to last years in implanted NHPs without damage to the brain[123–125]. Furthermore, due to their larger size, ECoG electrodes typically have much lower electrical impedance than implantable electrodes (e.g., the Utah array[126]), allowing them to electrically stimulate at higher currents to generate a stronger neural response. Recent studies have attempted the development of ECoG-based therapies through acute stimulation experiments in the somatosensory cortex[127–132] as well as chronically implanted devices[133,134]. One specific therapeutic use of ECoG stimulation, Responsive Neurostimulation (RNS®) therapy[135,136], was approved by the FDA in 2013. RNS is used to treat medically intractable epilepsy by measuring ECoG signatures of seizure and applying stimulation in a closed loop. The ECoG stimulation

research field is still in its early stages and therapeutic use of ECoG stimulation for the recovery of sensory function does not yet exist. There is still a wide gap in the scientific knowledge between electrical stimulation input and brain function output.

To effectively treat brain function loss or disorder using electrical stimulation, two fundamentally important relationships need to be understood. The first relationship is between disease symptoms and the defective neural activity patterns that cause them. This is commonly studied using disease animal models, whose brain structure and function can be measured and compared to that of healthy animals. The second relationship is between neural activity patterns and the electrical stimulation methods that evoke them. The parameters that determine the electrical stimulation impact on neural activity include electrode size and shape, surgical placement, and stimulation parameters such as strength, pulse shape, frequency, and spatiotemporal pattern. This second relationship is poorly understood due to a lack of preclinical methods capable of dissecting the relationship between electrical stimulation and cortical circuit activity.

4.1.2 Studying the neural response to electrical stimulation

Attempts at dissecting the relationship between electrical stimulation and neural activity date back to the 1950s[137] and earlier[138,139]. In 1968, a seminal study of *in vivo* electrical stimulation showed that stimulation-recruited neural activity was localized to a sphere around the stimulation site, with the size of the sphere determined by the stimulation current strength[140]. This work guided the general perception of the relationship between electrical stimulation and neural activity for decades, until a 2009 study, enabled by the advent of early calcium indicators and the maturation of 2PFM, painted a very different picture[21]. Histed et al. collected a much larger dataset, which showed distributed neural response over large cortical distances at both low and high current, a stark contrast to the predominant notion. Furthermore, moving the electrode site by only 15 μm in depth results in a largely new population of stimulated neurons. This new result supported the biophysics of electrical stimulation on neuron membranes: axons, but not somas, have the lowest threshold to external electrical input[141–144]. Therefore, moving only a short distance and exciting a new axon population would result in a new spatially distributed population of somas to activate. The findings by Histed et al. were met with some criticism[145], primarily regarding the electrical stimulation and two-photon imaging methods used. For one, calcium imaging was performed at the same plane as the stimulation site, which biased the soma response population towards cell types that projected their axons laterally rather than axially. Sampling neurons over a larger depth range may have resulted in observing soma responses that reduce with distance, as had been observed recently[146]. Data collected by Histed et al. may have also been contaminated by brain motion, since they physically advanced the implanted electrode to reach new axon populations.

Although calcium imaging has slower dynamics than the underlying electrical activity and data analysis requires careful elimination of artifacts, using 2PFM for studying neural response from electrical stimulation provides several key benefits. First, unlike electrical recording methods, 2PFM does not suffer from the stimulation artifact which obscures evoked electrophysiological responses. It can also record from more cells at once, with location specificity, compared to electrophysiology. Finally, a large, mature library of genetic tools provide microscopists with the

ability to distinguish between specific brain regions, neuronal subtypes, and chemical targets. These reasons have led researchers toward 2PFM as the method of choice when studying cortical electrical stimulation in animal models[146–149].

Recent years has also seen a push for modeling the neural response from electrical stimulation. Given the complex nature of the problem, models have also been complex, from biophysics simulations of the effect of stimulation pulses on anatomically accurate neurons[150–152] to models looking at responses in the context of a functioning cortical circuit[150,153]. These models provide testable hypotheses that neurons of different subtypes respond differently to the same electrical stimulus, due to both direct and indirect effects. Direct activation of neurons requires specific orientation and proximity of their processes with respect to the electric field generated by the electrode, so a given electrode position and stimulation waveform will directly excite a specific subset of neurons. Indirect activation or inhibition of neurons is less deterministic because it is a byproduct of direct activation, which causes downstream neural responses within complex circuitry. Towards the eventual application of electrical stimulation to therapy in awake and behaving patients, models should also consider interactions between electrically evoked and sensory evoked activity. Furthermore, behavioral conditions, such as arousal[154], modulate sensory evoked activity and likely also electrically evoked activity. These modeling studies underscore the importance of observing neural responses to electrical stimulation in a holistic fashion: from many neuronal subtypes in the cortical circuit, and within the context of natural brain activity, including sensory input.

The goals of this study were threefold. First, we wanted to design novel methods for concurrent cortical electrical stimulation and 2PFM in the awake, behaving mouse. This would allow us to measure cell type-specific neural activity during concurrent electrical stimulation. Next, we wanted to observe electrical stimulation-evoked responses in cortical neuron subtypes. Varying electrical stimulation parameters of current strength and pulse polarity, we wanted to test the differences between cortical cell types in their neural responses to electrical stimulation parameters. Finally, we wanted to test if, in the presence of salient sensory stimuli, neurons respond differently to electrical stimulation.

4.2 Methods

4.2.1 Electrode fabrication and mouse implantation

Electrode arrays were microfabricated using similar methods to previously described processes[155,156]. In brief, an established photolithographic fabrication technique embedded PtAg alloy metal traces in a thin optically transparent parylene C substrate. Exposed PtAg electrode contact surfaces were dealloyed in nitric acid which leaves a platinum nanorod (PtNR) film. Compared to PEDOT:PSS, a standard electrode surface coating in neural devices known for its good electrochemical properties, PtNR film-coated electrodes of the same diameter demonstrated comparable impedance at 1kHz and greater charge injection and storage capacity due to its much larger surface area. With larger charge injection and storage capacities, PtNR electrodes were able to inject higher currents without water hydrolysis when compared to PEDOT:PSS electrodes of the same dimensions, making it a superior choice for electrical stimulation. Two different electrode

array layouts using different sized contacts (90 µm and 200 µm diameter) were fabricated for the data collection of this study using the same fabrication methods. Fabricated electrodes were bonded to printed circuit boards (PCBs) using silver epoxy (MG Chemicals 8331) based bump bonding, as described in a previous study[156]. Zero-insertion force (ZIF) connectors attached a ribbon cable between the electrode-bonded PCB and the stimulation/amplifier chip (Intan RHS headstage). Electrode impedances at 1kHz were measured in saline prior to mouse implantation to verify successful fabrication and electrical connection.

All animal experiments were conducted according to the National Institutes of Health guidelines for animal research. Procedures and protocols on mice were approved by the Animal Care and Use Committee at the University of California, Berkeley. Methods for chronic mouse implant surgery were adapted from previous studies[23,58], with additional steps involving the PtNR electrode array. Mice aged 3-6 months, either wildtype (WT, JAX 000664) or of a transgenic background for the Cre-recombinase labeling of inhibitory cell types (PV-Cre, SST-Cre, NDNF-Cre; JAX 017320, 013044, 030757 respectively), were anesthetized and head-fixed in a stereotaxic apparatus (Kopf Instruments). A 3.5 mm diameter craniotomy was performed over the left primary visual cortex (V1, ~2.5 mm medial-lateral and 1 mm anterior-posterior to lambda) and nine viral injections of GCaMP6s[6], a genetically encoded calcium indicator, were made in a 3x3 grid in the exposed cortex, with an average injection spacing of ~600 µm. For WT animals, 30 nL of AAV2/1-syn-GCaMP6s at a titer of 1.3E13 was injected at 250 µm below brain surface per injection site. For PV-Cre, SST-Cre, and NDNF-Cre animals, 30 nL of AAV2/1-syn-FLEX-GCaMP6s at titers of 2.6E12 to 1.3E13 were injected at 250 µm below brain surface per injection site. Cranial windows were made using two glass pieces of 170 µm thickness, a 3.5 mm diameter disk and a 3 mm inner diameter ring, concentrically attached to each other with a UV-cured optical adhesive (Norland NOA61). The PtNR electrode array was then attached to the glass disk with the same optical adhesive, as demonstrated in a similar surgery[157]. The electrode array and cranial window complex was placed into the craniotomy and sealed with tissue adhesive (3M VetBond). Exposed electrode traces emerging from the posterior edge of the cranial window were coated with a surgical-grade silicone elastomer (Kwik-Sil, World Precision Instruments) to protect it from being damaged by dental acrylic, as demonstrated in previous chronic neural electrode implant methods[158,159]. A stainless-steel head-bar was then rigidly attached to the skull with dental acrylic and allowed to cure. A 3D resin-printed structure was attached to the head-bar and functioned as both the head-cone to reject stray light during 2PFM and housing for the electrode-bonded PCB. Finally, additional silicone elastomer, dental acrylic, and superglue (Loctite) were used to protect exposed electrode traces, provide additional structural support, and seal the implant, where needed. Implanted mice were provided with a post-operative analgesia Meloxicam (SC, 5 mg/kg) for 2 days and allowed to recover for at least 2 weeks prior to experiments.

4.2.2 Experimental setup and data acquisition

After surgery recovery, implanted mice showed good viral expression of GCaMP6s, as monitored with an epifluorescence surgical microscope. Mice were habituated to head fixation for 15 minutes twice total: the first time was around 1-week post-implant, and the second time was one or two days prior to their first imaging session. Mice were head-fixed and rigidly attached to the sample

stage of a commercial 2PFM system with Bessel imaging, which was previously introduced and characterized[23]. All two-photon imaging was performed with 920 nm wavelength excitation light from a femtosecond titanium-sapphire laser (Chameleon Ultra II, Coherent Inc.). Gaussian beam illumination was used for most of the data acquisition, except for L2/3 SST data, which was collected using Bessel beam illumination. Bessel beam imaging was performed at 0.4 NA with a 25x 1.05NA Olympus objective lens, using methods previously described[23,52]. Gaussian imaging was performed with post-objective laser powers ranging between 4 and 89 mW. Deeper FOVs were imaged with more power (L1: 11.3±6.9 mW, L2/3: 26.5±12.0 mW, L4: 62.9±17.7 mW, mean ± S.D.). Bessel imaging in L2/3 was performed with larger post-objective laser powers than Gaussian, ranging between 165 and 202 mW, due to a higher fraction of excitation energy lost to Bessel focus side rings[57].

Visual stimulation was administered using a laptop (HP Spectre x360 13 with AMOLED screen) displaying monochrome blue light at the lowest brightness setting. An OLED screen was chosen to provide a 100% contrast between the peak and trough of the drifting grating stimulus despite being on the lowest brightness setting. The visual stimulation screen was centered at 10.5 cm from the mouse's right eye and covered 75° x 75° of visual space. Drifting grating stimuli with a spatial frequency of 0.07 cycles/degree and temporal frequency of 2 cycles/second (parameters from a previous study[58]) were used. A uniform visual stimulus at the middle brightness value of grating stimuli was presented during baseline periods to maintain similar total luminance between baseline and response periods.

Electrical stimulation and all impedance measurements were performed using the Intan RHS Stim/Recording System and RHX software. The electrode ground was attached to the mouse head-bar, which was rigidly (and electrically) connected to both the skull and scalp. Stimulation parameters were pseudorandomly varied and sent to the headstage via TCP control before every trial using a MATLAB script. The electrode stimulation pulse was triggered by a digital input from a photodiode reading the visual stimulation screen, to eliminate jitter caused by the screen's refresh rate.

Retinotopic measurements were performed once for each animal, using a large FOV 10x 0.45NA Nikon objective lens covering a FOV of 2.2 x 2.2 mm. The visual stimulation screen pseudorandomly flashed a square section of the screen chosen from a 3x3 grid spanning a total of 75° x 75° of visual space. Averaging the neural responses from these visual stimuli, a retinotopic map was reconstructed to identify the region of the cranial window that corresponded to V1. Within the retinotopic region, smaller imaging FOVs were chosen for higher resolution 2PFM. Electrically connected and low-impedance electrode contacts near the smaller FOVs were chosen to be the source of electrical stimulation, and imaging depths were varied to cover the majority of L2/3, L4, and/or L1, depending on the animal. A unique FOV was defined as an ROI population which did not overlap with previously collected data, so unique FOVs could share the same depth or X-Y area, but never both.

A 25x 1.05NA Olympus objective lens was used for high resolution 2PFM during concurrent electrical and/or visual stimulation. Fluorescence data acquisition was performed at 15 Hz over a

781 x 781 μm FOV with 0.762 μm pixel size for 6 seconds per trial, beginning with 2 seconds of baseline then 4 seconds of stimulation response. The onset of data acquisition was triggered using another photodiode reading the visual stimulation screen, such that the visual stimulation computer acted as the master clock for both two-photon data acquisition and electrical stimulation. After the 6 seconds of fluorescence data acquisition, there was a break of 4 seconds for fluorescence response to fall back to baseline levels, for a total of 10 seconds per trial. 450 total trials lasting 75 minutes consisted of 10 repeats of 45 unique trial types of visual-electrical stimuli pairs: 9 unique visual stimuli (8 drifting grating directions plus a blank control) and 5 unique electrical stimuli (cathode-leading or anode-leading 100 or 200 μA current strength, plus a 0 μA control). Animals were imaged up to 4 days total over a two-week period post-recovery, with each day consisting of up to 2 unique FOVs.

4.2.3 Data preprocessing

In total, 62 unique FOVs were imaged across 14 animals split across 4 genetic backgrounds (WT: 3 animals, 14 FOVs, PV: 3 animals, 12 FOVs, SST: 5 animals, 21 FOVs, NDNF: 3 animals, 15 FOVs). All image preprocessing, visualization, and analyses were performed in ImageJ and MATLAB (MathWorks). Raw two-photon fluorescence images were first registered to remove rigid lateral motion artifacts before further analyses. All ROIs for all FOVs were hand-drawn by the same person. Cell bodies were hand-drawn with the oval tool in ImageJ, primarily using the mean and standard deviation images of the stack as reference, but also 5-frame and 15-frame averaged image stacks to catch very sparsely-firing ROIs that may not appear in the mean or standard deviation images. Fluorescence traces were extracted for each ROI by averaging the signals from all pixels within the circled ROI.

An important pre-processing step in 2PFM of soma signals was the subtraction of neuropil contamination signal. This step was even more critical for electrical stimulation experiments since electrical stimulation directly and strongly excited neuropil. In this study, fluorescence traces of nearby neuropil signals were extracted and subtracted from the ROI signals following similar methods to a previous study[160]. The average fluorescence signal from a 35 μm radius area centered on a drawn ROI, excluding pixels belonging to circled ROIs, was extracted for each ROI. The extracted neuropil trace was then compared to the extracted ROI trace to find a neuropil subtraction coefficient for the ROI that best removes the contaminant neuropil signal (see the Supplementary Fig. 2a from Dipoppa et al.[160]). This method of determining the neuropil subtraction coefficient specifically relies on sparse neural response, so only large skew (> 2) ROI traces were considered. Assuming the uniformity of the neuropil subtraction coefficient across a FOV, the mean measured coefficient was used for all ROIs in that FOV. Additionally, the extracted neuropil trace was baseline-subtracted prior to subtraction to not create artificially low baseline values for neuropil-subtracted ROI traces. Neuropil subtraction coefficients were determined separately for each unique FOV, to account for differences in cell type-dependent neuropil density, imaging method differences (Gaussian vs. Bessel beam), imaging depth, etc. (Table 3). Finally, neuropil-subtracted ROI fluorescence traces were converted to $\Delta F/F_0$, where F_0 was the mode of the signal trace.

We removed all inactive ROIs from further analyses. ROIs were considered active if at any point during the experiment, in the presence of electrical stimulation or visual stimulation or both,

fluorescence $\Delta F/F_0$ rose above the mean baseline + 3 standard deviations for 1 second. Baseline data was defined as the time points during the 2 seconds of data acquisition before the response period. Due to the large number of trials per experiment which resulted in long 75-minute imaging sessions, we sometimes observed a very slow drift in a ROI's baseline over the course of the experiment. This extremely slow drift (on the order of minutes) could be due to several factors, including sample motion, brain state changes, and learning/habituation processes. To remove these effects from our data, we subtracted baseline signal separately for each trial of each ROI. However, some ROIs showed highly varied baseline values within an experiment, so subtracting baselines from these ROIs would result in largely varied responses. Much of these ROIs with highly varied baselines had high rates of spontaneous activity and were not good ROI candidates to observe responses to electrical nor visual stimulation. As a result, we removed these ROIs whose baseline values were very different from those of the ROI population (all ROIs of the same cell type). Specifically, baselines that were farther than the population median ± 3 times the median absolute deviation. This was a small proportion of ROIs (< 15%) that did not end up affecting the findings of this study. A caveat to subtracting baselines from our data is the removal of physiological effects that we would have wanted to study. For example, it would be useful to characterize how quickly cells become habituated, if at all, to consistent electrical perturbation, resulting in weaker responses over time. It would also be useful to know the animal's brain state so that we can look for differences in stimulation sensitivity during times of high vs. low alertness.

4.2.4 Analysis and statistics

Electrical stimulation-only analyses were performed in Figs. 12 and 19 by analyzing only the subset of trials which had blank visual stimulation (50/450 trials). For each of the 5 electrical stimulation conditions, there were 10 trials, whose responses were averaged for a mean response. The population mean response to electrical stimulation was an average of the mean responses for all individual ROIs. Shaded SEMs throughout this study were calculated based off the number of ROIs, not the number of trials, that were averaged. The averaged first second of response for a given ROI, coined the "early response", was an average of 15 frames (at 15 Hz) beginning immediately post-stimulation, whereas the "late response" was an average of the last 15 frames of the trial (frames 46-60 post-stimulation). Statistical differences between the early responses of two electrical stimulation conditions were tested using two-sample Kolmogorov-Smirnov (KS) tests. 3D distances between ROIs and stimulating electrodes were calculated using the centers of both objects. Correlation strength and statistical significance between an ROI's early response strength and its distance from the electrode were calculated by fitting a linear regression model.

Visually-evoked ROIs were defined as ROIs that significantly respond to at least one visual stimulus. Specifically, an ROI's "late response" to a visual stimulus in the absence of electrical stimulation was compared to its baseline period using a Student's t-test. An ROI was considered visually-evoked if at least one drifting grating direction tested significant against baseline ($p < 0.05$). Note that this criterion did not distinguish between direction-selective ROIs and ROIs that responded to all visual stimuli, a feature of many INs. Nor does this criterion select for high gOSI values or good tuning curve fitting.

ROIs' early responses to visual stimuli (in the absence of electrical stimulation) were fit to double gaussian curves. The double gaussian curve was constrained in two ways, for better fitting performance: the two gaussians had peaks exactly 180° apart, and had the same tuning widths (sigma, or width, of the gaussian function). Preferred tuning direction was defined as the peak position of the larger fitted gaussian. Widths of the fitted gaussians, which were conventionally used to represent the tuning width (or tuning sharpness) of neurons[58], were not further analyzed due to the insufficient sampling of drifting grating angles in our experiment. Over a large population of ROIs, preferred tuning directions were uniformly distributed (Fig. 13d). Averaged time traces (e.g., Fig. 13c) were plotted based on ROIs' preferred tuning directions rounded to the nearest 45°, wrapped to 0°, then averaged. ROI early responses were similarly averaged for the population tuning curves (e.g., Fig. 13f). Double gaussian fitting of the population tuning curve had an additional constraint of the preferred direction peak being at 0°. Global orientation selectivity indices (gOSIs) for each electrical stimulation condition were calculated for each ROI using their mean early responses. gOSIs are a non-fitted measure of orientation specificity that considers the contrast of responses across all orientations and is a preferred metric for characterizing V1 tuning. We used a two-sample KS test to test for significant differences between gOSI distributions of different electrical stimulation conditions.

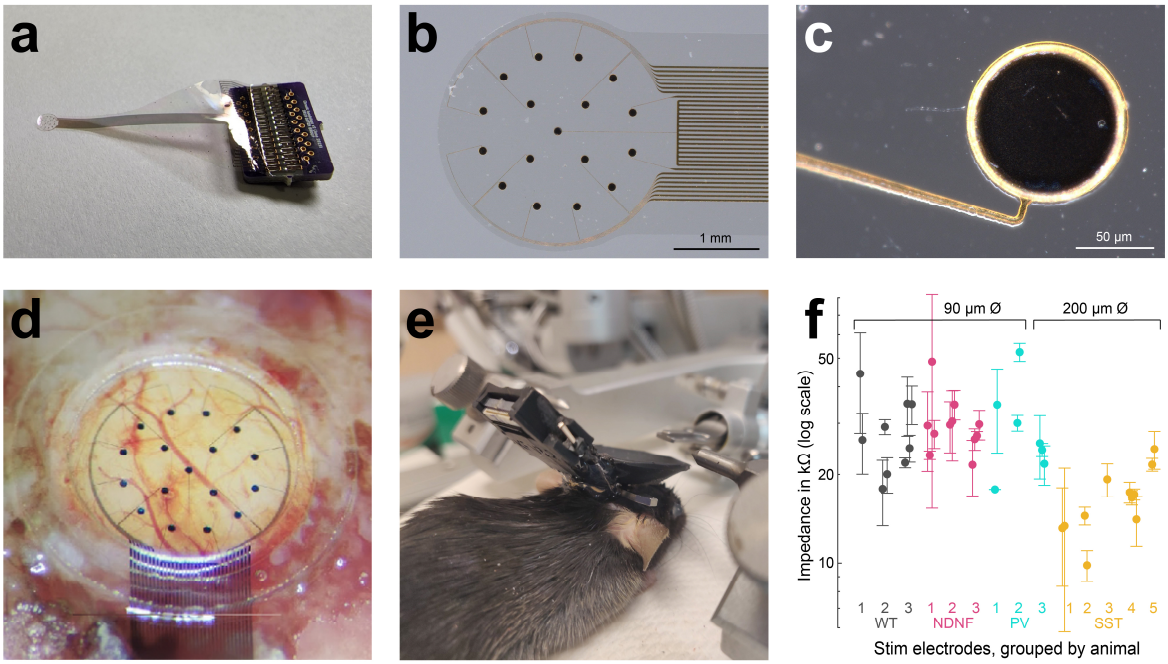

Figure 11. Chronic implantation of a PtNR electrode array and cranial window in mice.

(A) PCB-bonded flexible microelectrode array. **(B)** Zoomed in view of electrode array. **(C)** Further zoomed in view of a single electrode contact. **(D)** Electrode glued to glass window, implanted in a craniotomy during surgery. **(E)** Mouse immediately post-surgery, showing 3D-printed implant housing and head bar. **(F)** Impedances of electrode contacts used for electrical stimulation. Each circle represents one unique electrode contact. Two different electrode contact diameters were used in this study, labeled. Error bars = S.D. over multiple measurements on each electrode contact (2 to 9 measurements per contact). One impedance measurement was performed per experiment session which used the electrode contact for stimulation.

4.3 Results

4.3.1 A novel brain surface implant compatible with 2PFM imaging of the awake mouse cortex

We developed a novel chronic mouse brain implant that combines a cranial optical window with a surface electrode array for concurrent cortical microstimulation and 2PFM in the awake mouse (Fig. 11a-e). The electrode array mirrored that of a miniaturized human ECoG array, placed during surgery on the intact mouse dura, which is similar in thickness to the human pia mater. Fabrication of the electrode array included the process of developing platinum nanorod (PtNR) films on electrode contact surfaces, which resulted in impedances comparable to the popular PEDOT:PSS (Fig. 11f), while having better charge injection and storage capacity[155]. Craniotomy and viral injection methods were adapted from previous chronic studies[23,58]. The PtNR electrode array, glued to a glass window, was implanted into the craniotomy as part of the surgical procedure.

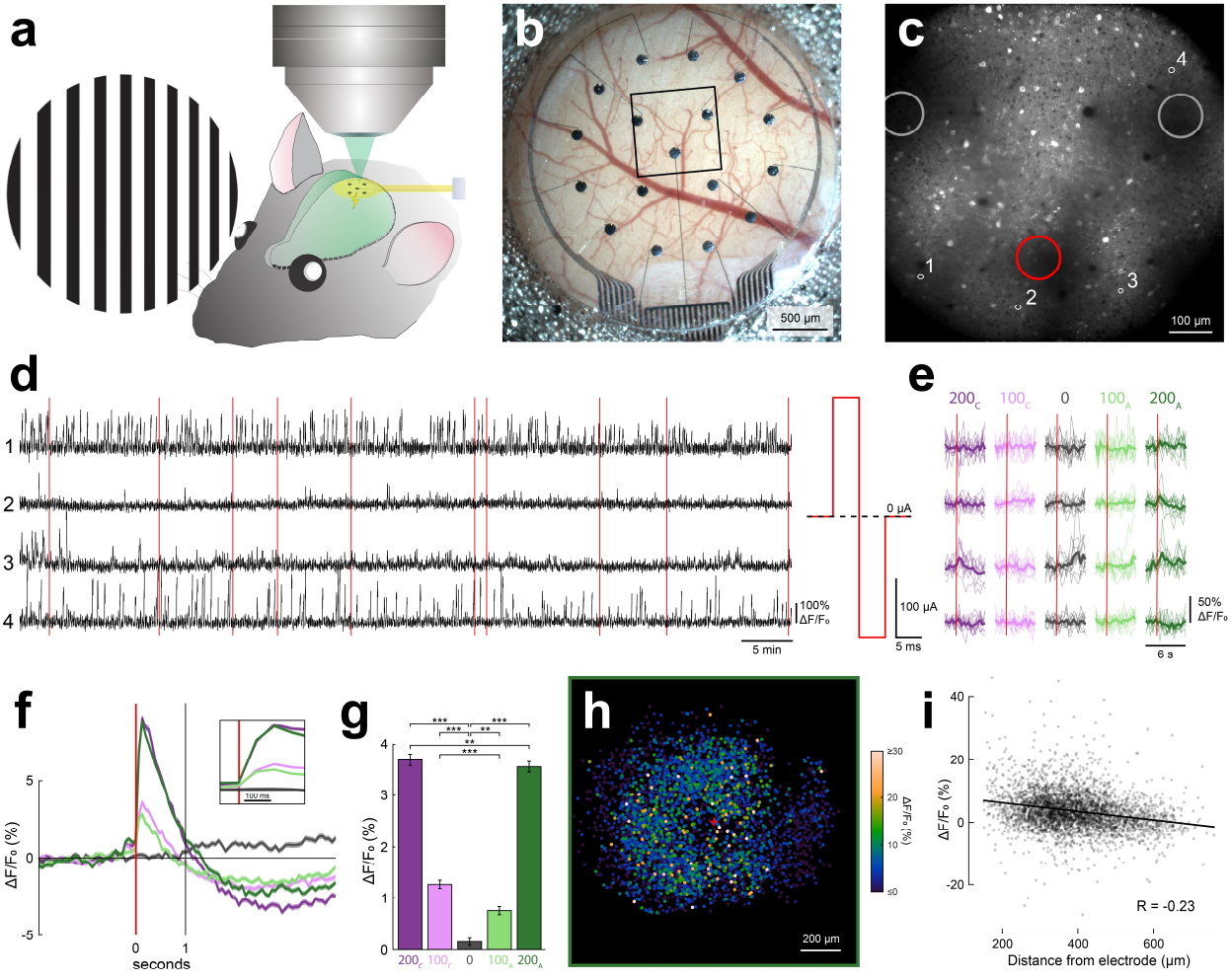

Figure 12. Layer 2/3 neurons are activated by single-pulse brain surface electrical stimulation.

Figure 12 captions.

(A) Setup for concurrent 2PFM, electrical stimulation, and visual stimulation of the awake mouse V1. **(B)** Surgical light microscope image of a cranial window 2 weeks post-implant. The black square represents an example 2PFM FOV. **(C)** Averaged image of two-photon calcium fluorescence at the FOV from B, 200 µm below the brain surface. The image was averaged over a full experiment and displayed at 0.5 gamma for better visibility of dim structures. Large circles represent the X-Y extent of brain surface electrodes, with the red circle representing the electrode chosen for stimulation. Small circles show several example hand-drawn soma ROIs. **(D)** Fluorescence time traces of the example ROIs from C, over a 75-minute experiment. The 75-minute time trace is made of 450 individual trials of 6-second acquisitions at 15 Hz, with 4 seconds of pause in between trials. For each trial, one electrical stimulation pulse was administered 2 seconds after the start of image acquisition. Red bars highlight the pseudorandomly-distributed 10 trials of 200 µA anode-first stimulation without visual stimulation. Traces are visualized with a 5-frame binned average, but all analyses were performed on non-binned data. Right: Waveform for a 200 µA anode-first stimulation pulse. The biphasic pulse consisted of two equal phases lasting 5ms each of equal but opposite current strength. **(E)** Individual trials (thin lines) and mean response (thick lines) to electrical stimulation of the ROIs from D. Electrical stimulation conditions are color coded, and the time of pulse stimulation is shown with red bars, 2 seconds after the start of image acquisition. **(F)** Mean 15 Hz fluorescence traces over all L2/3 WT neurons (N = 3570) in response to an electrical stimulation pulse (red bar). Traces are colored by stimulation strength. SEM shaded. Inset shows traces zoomed in at the time of electrical stimulation. **(G)** Mean of the first second post-stimulation (0 – 1s) response (early response), showing significant response differences between stimulation and no stimulation conditions. Response differences between cathode-first and anode-first stimulation pulses of the same current strength were also significant. P values: *: < 0.05, **: < 0.01, ***: < 0.001. **(H)** Early response to 200 µA anode-first stimulation, plotted by lateral distance from stimulation source (electrode contact center represented by red "+") for all L2/3 WT neurons. **(I)** Data from H plotted vs. 3D distance from electrode contact center. There is a significant ($p < 0.001$) linear correlation between cell body distance from electrode and response strength for all electrical stimulation conditions (data only shown for 200 µA anode-first stimulation).

4.3.2 Electrical stimulation evokes neuronal responses in a current-dependent manner

We expressed the genetically encoded calcium indicator GCaMP6s[6] in 14 mice across 4 genetic backgrounds using Cre-dependent viral expression. Chronically implanted mice were head-fixed and imaged with conventional Gaussian or Bessel 2PFM during concurrent electrical and/or visual stimulation (Fig. 12a). Imaging fields of view (FOVs) were chosen within the primary visual cortex (V1), verified by retinotopy, and a nearby brain surface electrode was used to issue single pulse stimulation during concurrent 2PFM (Fig 1b,c). Fluorescence of hand-drawn somas were extracted and neuropil-subtracted prior to analysis (see Methods section 4.2.3). A set of stimulation conditions were used throughout the 75 minute, 450 trial experiment, with the same stimulation condition pseudorandomly repeated 10 times. For each trial, a single symmetric biphasic stimulation pulse (Fig. 12d, right) was administered. The 10 trials with anode-leading 200 µA stimulation in the absence of visual stimulation are labeled with red bars in Fig. 12d. Responses to electrical stimulation for each example neuron was shown in Fig. 12e. Some example neurons showed response to electrical stimulation while some did not. Fluorescence time traces of example neurons in Fig. 12d,e were 5-frame averaged for better visualization, but all analyses were conducted on non-averaged data.

Mean fluorescence response to electrical stimulation in the absence of visual stimulation over all cortical layer 2/3 (L2/3) WT neurons (3 animals, 14 FOVs total, N = 3570 ROIs) is shown in Fig. 12f. Two seconds of fluorescence signal before the onset of the electrical stimulation pulse was captured as baseline signal. Fluorescence response averaged over the first second, hereby considered the "early response", was significantly greater with electrical stimulation than without, for all four stimulation conditions (Fig. 12g, 200C: p=1.7E-85, 100C: p=8.3E-13, 100A: p=0.0023, 200A: p=7.5E-81, two-sample KS-test). The fast dynamics of this response (Fig. 12f, inset) suggested that electrical stimulation was directly activating cells in this population, as opposed to indirect effects, such as disinhibition. After the early response, fluorescence response to electrical stimulation reversed and became suppressed, suggesting the presence of a slow, indirect inhibitory effect. 200 µA stimulation current induced significantly larger fluorescence responses compared to 100 µA, and cathode-leading pulses induced slightly larger fluorescence responses than anode-leading pulses (Fig. 12g, 200 µA: $p = 0.004$, 100 µA: $p = 3.1 \times 10^{-7}$, two-sample KS-test). We also observed a correlation between a neuron's early response strength and its distance from the center of the stimulating electrode, for all electrical stimulation conditions (anode-leading 200 µA data shown in Fig. 12h,i, $p = 2.2 \times 10^{-45}$).

4.3.3 Electrical stimulation reduces orientation selectivity in the primary visual cortex

We observed that the effect of electrical stimulation on putative PNs in the mouse V1 depended on the strength of concurrent sensory input. An example neuron with electrical stimulation-evoked and orientation-selective responses shows the format of collected neural data (Fig. 13a). Tuning curves for the example neuron revealed its preferred direction, and the reduction of its preferred responses in the presence of electrical stimulation (Fig. 13b). Next, we looked at only visually responsive neurons when performing analyses involving visual stimulation conditions (see Methods section 4.2.4). Although PNs make up a large majority of visually responsive WT neurons, we also replicated key analyses using narrower criteria which better isolated PNs from inhibitory neurons, to similar results (Fig. 14). In the absence of visual stimulation, visually responsive neurons showed immediate increased response to electrical stimulation, with a larger response observed for larger stimulation current like in Fig. 12f (Fig. 13c, N=2173). In the presence of visual stimulation, fluorescence responses were divided into three categories, depending on the neurons' drifting grating direction preference (orthogonal, preferred, and opposite, see Fig. 13b x-axis labels). Neurons at their orthogonal visual stimuli received little to no visually-driven response, and responded to electrical stimulation like they would in the absence of visual stimulation. Conversely, neurons at their preferred and opposite visual stimuli showed an expectedly large visually-driven mean response, which was quickly suppressed by electrical stimulation within the first second. At 15 Hz imaging frame rate, we were able to discern the temporal difference between stimulation modalities: electrically evoked activity was fast and peaked within a couple of imaging frames, whereas visually-evoked activity slowly climbed over seconds.

Early response for all visually responsive WT neurons, sorted by their preferred direction, were shown in Fig. 13d. Without electrical stimulation, we observed a diagonal line of positive fluorescence response (middle column) suggesting most of these neurons were orientation or direction tuned, as expected with PNs. In the presence of electrical stimulation, the diagonal line became difficult to see, in part due to the increase in response over all visual stimuli. Subtracting

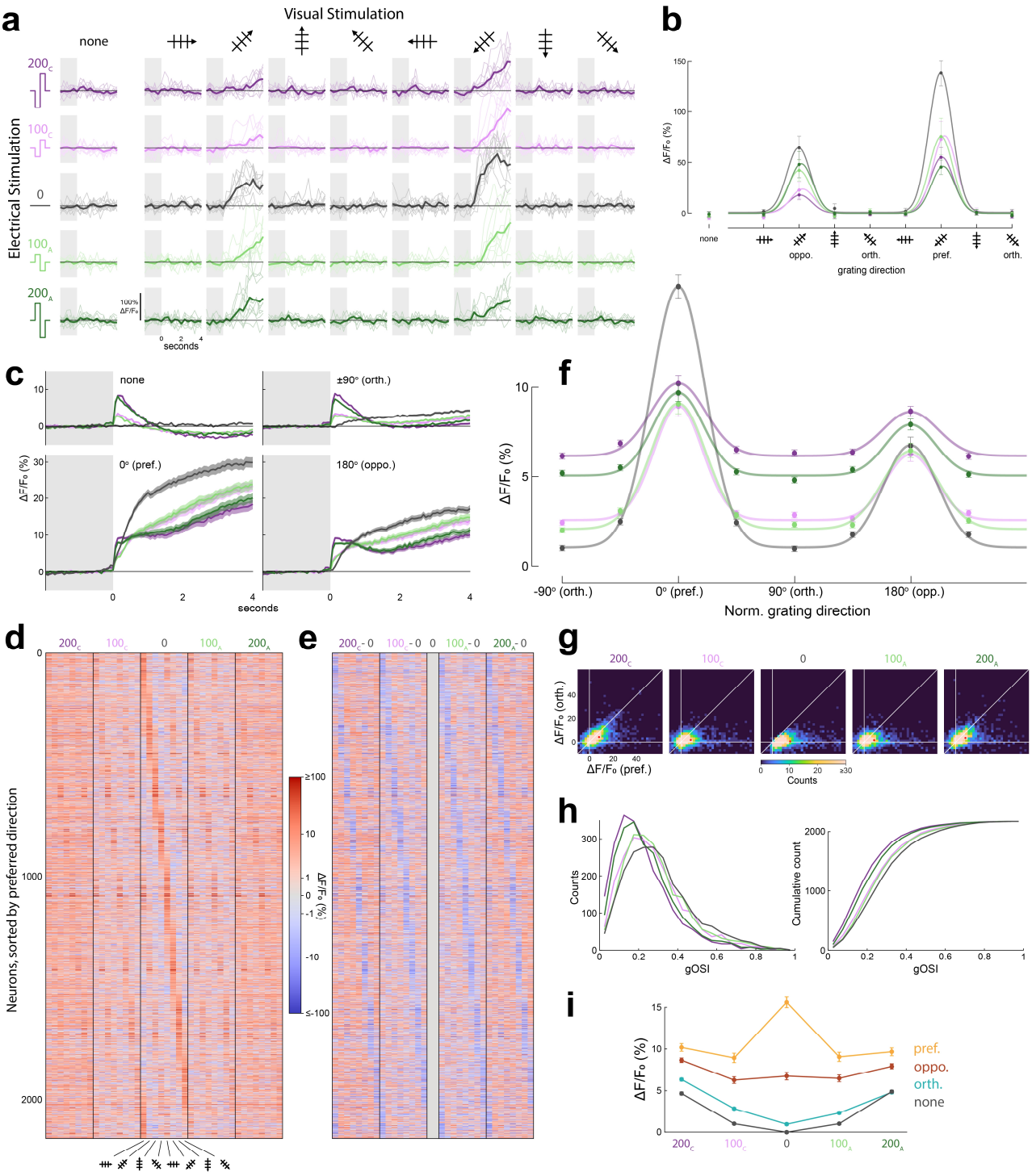

Figure 13. Electrical stimulation reduces orientation selectivity in layer 2/3 neurons.

Figure 13 captions.

(A) Data from one example neuron shows orientation and direction-selective responses to visual stimulation. Each plot represents one electrical-visual stimulation parameter pair, labeled by the row and column labels respectively. Traces are visualized with a 5-frame binned average, but all analyses were performed on non-binned data. Mean time traces of 10 trials shown in bold. 2 seconds of baseline period (shaded gray background) precedes 4 seconds of visual drifting grating stimulation (white background), with the electrical stimulation pulse at the onset of visual stimulation. **(B)** Tuning curve showing mean fluorescence over the 4 second response period to the 8 visual stimulation orientations for the example neuron in A. This example neuron shows a reduction of fluorescence response in the presence of electrical stimulation at both its preferred direction and the opposite direction (180° from the preferred direction), with no fluorescence response at orthogonal (±90° from the preferred direction). Double gaussian curves were used to fit direction-specific responses for each electrical stimulation condition. **(C-I)** Analyses on all visually evoked L2/3 WT neurons (N = 2173, see Methods section 2.2.4). **(C)** Mean fluorescence traces separated into 4 visual stimulation conditions: no stimulus, orthogonal, preferred, and opposite. Each neuron's preferred direction was determined individually using a double gaussian fit (see Methods section 2.2.4). SEM shaded. **(D-I)** Mean response from the first 1 second of the response period (early response) was used for analyses. **(D)** Heatmap showing response strength. Rows are individual neurons sorted by their preferred direction, and columns are electrical-visual stimulation parameter pairs. **(E)** Heatmap showing the difference between electrically-stimulated and non-electrically-stimulated responses from D. Blue represents a reduction in response while red represents an increase in response. **(D,E)** Heatmap colors were plotted on a symmetric log scale for better visualization. **(F)** Population mean tuning curve of the early response. Like in C, preferred directions were determined individually for each neuron. Double gaussian curves were used to fit relative direction-specific responses for each electrical stimulation condition. **(G)** 2D histograms of neurons' preferred vs. orthogonal response strengths, separated by electrical stimulation strength. The average of the data is represented with a red circle. Data on the diagonal line represent cells that do not have a preferred drifting grating direction. **(H)** Histogram and cumulative distribution of neurons' gOSIs, separated by electrical stimulation strengths. The population gOSI distribution is reduced at 100 μA stimulation and further reduced at 200 μA stimulation. **(I)** Population mean electrical stimulation curve of the early response. 4 curves correspond to the 4 visual stimulation conditions from C, labeled by color.

the visual-only response of these neurons from their electrical stimulation responses revealed that responses at preferred directions reduced (blue diagonals) while responses at non-preferred directions increased (Fig. 13e). During the last 1 second of visual stimulation, hereby referred to as the "late response", we observed electrical stimulation-evoked suppression which was especially pronounced at cells' preferred orientations (Fig. 15). A direction-normalized population mean tuning curve of the early response summarized the visually-dependent electrical inhibition effect (Fig. 13f, Table 1). Two-dimensional (2D) histograms showed the distribution of the visually-responsive WT population according to their early response to preferred and orthogonal visual stimuli (Fig. 13g). Distributions shifted toward both a decrease in preferred direction signal and an increase in orthogonal signal in the presence of electrical stimulation. As a result of the changes in response to preferred and orthogonal stimuli, we observed a significant decrease in the WT population's global orientation selectivity index (gOSI) distribution (Fig. 13h, Table 2). This suggested that electrical stimulation may have reduced orientation selectivity in the mouse V1 by enhancing neuronal activity at non-preferred stimuli while suppressing activity at preferred stimuli.

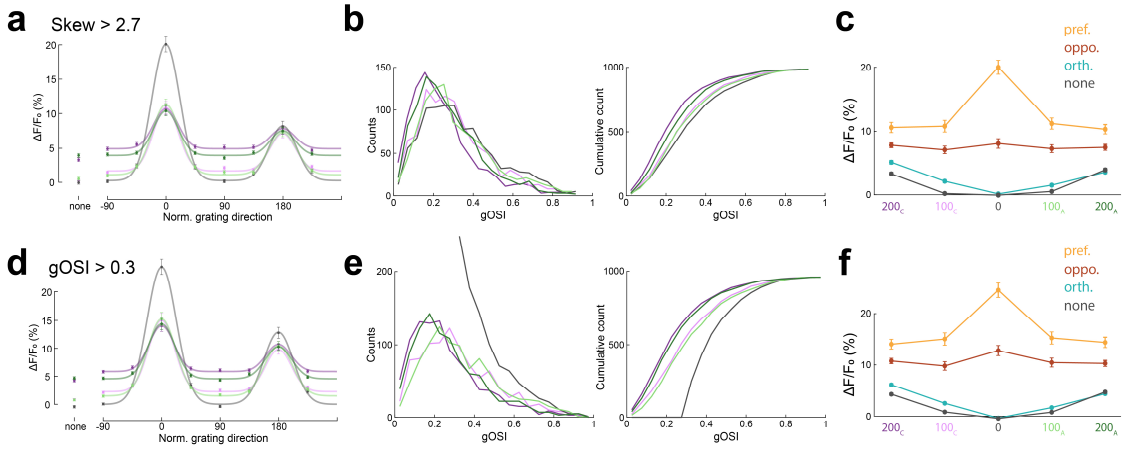

Figure 14. Electrical stimulation reduces orientation selectivity in putative L2/3 pyramidal neurons.

(A-C) Analyses on all visually evoked L2/3 WT neurons with a fluorescence trace skewness > 2.7 (N = 986). Neurons with skewness > 2.7 are exceedingly likely to be PNs, from Dipoppa et al. 2018. A, B and C are counterparts to Fig. 13f, 13h, and 13i, respectively. **(D-F)** Analyses on all visually evoked L2/3 WT neurons with gOSI > 0.3 (N = 959). Neurons with a large gOSI are more likely to be PNs, since INs tend to respond to all orientations, thereby having lower gOSIs on average. Both methods for filtering out INs from the WT population result in similar qualitative results to Fig. 13.

4.3.4 PV interneurons are suppressed, not excited by brain surface electrical stimulation

Given our observations on electrical stimulation-induced suppression of sensory signals in L2/3 putative PNs, we looked to local interneuron (IN) subtypes to understand the inhibitory source. Parvalbumin-expressing (PV) INs are a group of cells characterized by their direct inhibition of PNs at the soma and basal dendrites. We injected Cre-dependent GCaMP6s into transgenic mice expressing Cre recombinase in PV INs to isolate GCaMP6s fluorescence only within PV INs (3 animals, 12 FOVs total, example FOV shown in Fig. 16a). PV INs have been shown to provide important inhibitory control during mouse visual orientation tuning experiments. Specifically, several studies have shown artificially activated PV INs to preferentially inhibit PNs at their preferred orientations, and/or suppressed PV INs to preferentially excite PNs at their preferred orientations[161,162], like our observations in Fig. 13. A contrasting study showed that activating PV INs inhibited PNs but sharpened, not broadened orientation selectivity[163]. In any case, PV INs were a candidate for our observed suppression of PN activity at preferred stimuli.

Surprisingly, we found that PV INs were not directly activated and their visually-evoked responses were suppressed by electrical stimulation (visually responsive L2/3 PV INs, N=156, Fig. 16b). Early response for all visually responsive L2/3 PV INs, sorted by their preferred direction, were shown in Fig. 16c. Subtracting the visual-only response revealed the largely inhibiting electrically evoked response which were most inhibiting at preferred directions (Fig. 16d). Because of the reciprocal connections between PV INs and nearby PNs, our observed suppression of PV INs was

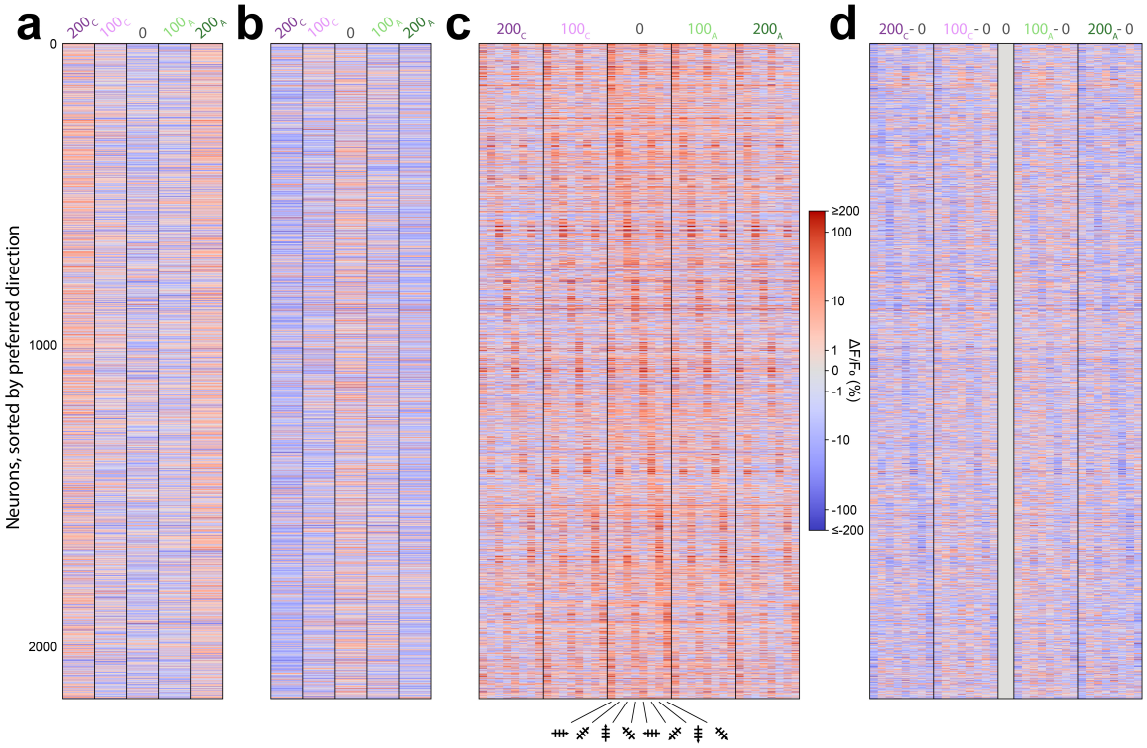

Figure 15. Preferred orientation responses remain preferentially suppressed seconds after electrical stimulation.

Additional heatmaps of visually-evoked L2/3 WT neurons (N = 2173), sorted the same as Fig. 13d-e. Heatmap colors were plotted on a symmetric log scale for better visualization. Note that colormap maximum and minimum values are larger than that of Fig. 13d-e. **(A)** Heatmap of the early response period (0-1 seconds after electrical stimulation) for trials without visual stimulation, showing an overall increase in response to electrical stimulation. **(B)** Heatmap of the late response period (3-4 seconds after electrical stimulation) for trials without visual stimulation, showing an overall reduction in response to electrical stimulation. **(C)** Heatmap of the late response period for trials with visual stimulation. Rows are individual neurons sorted by their preferred direction, and columns are electrical-visual stimulation parameter pairs. **(D)** Heatmap showing the difference between electrically-stimulated and non-electrically-stimulated responses from C. Note the overall suppression of signal in the late response, with a larger magnitude of suppression at preferred directions.

likely a downstream result of the PN suppression observed in Fig. 13. Because PV INs primarily derived their orientation tuning properties from nearby PN inputs, a reduction of PN tuning selectivity, as was observed, would also reduce PV IN tuning selectivity. Indeed, looking at the population mean tuning curve we observed that L2/3 PV IN fluorescence response was maximally suppressed at the preferred grating direction (Fig. 16e, Table 1). 2D histograms of preferred vs. orthogonal response showed a reduction of preferred response due to electrical stimulation (Fig. 16f). Because electrical stimulation reduced the response at all orientations, gOSI distributions did not considerably change (Fig. 16g).

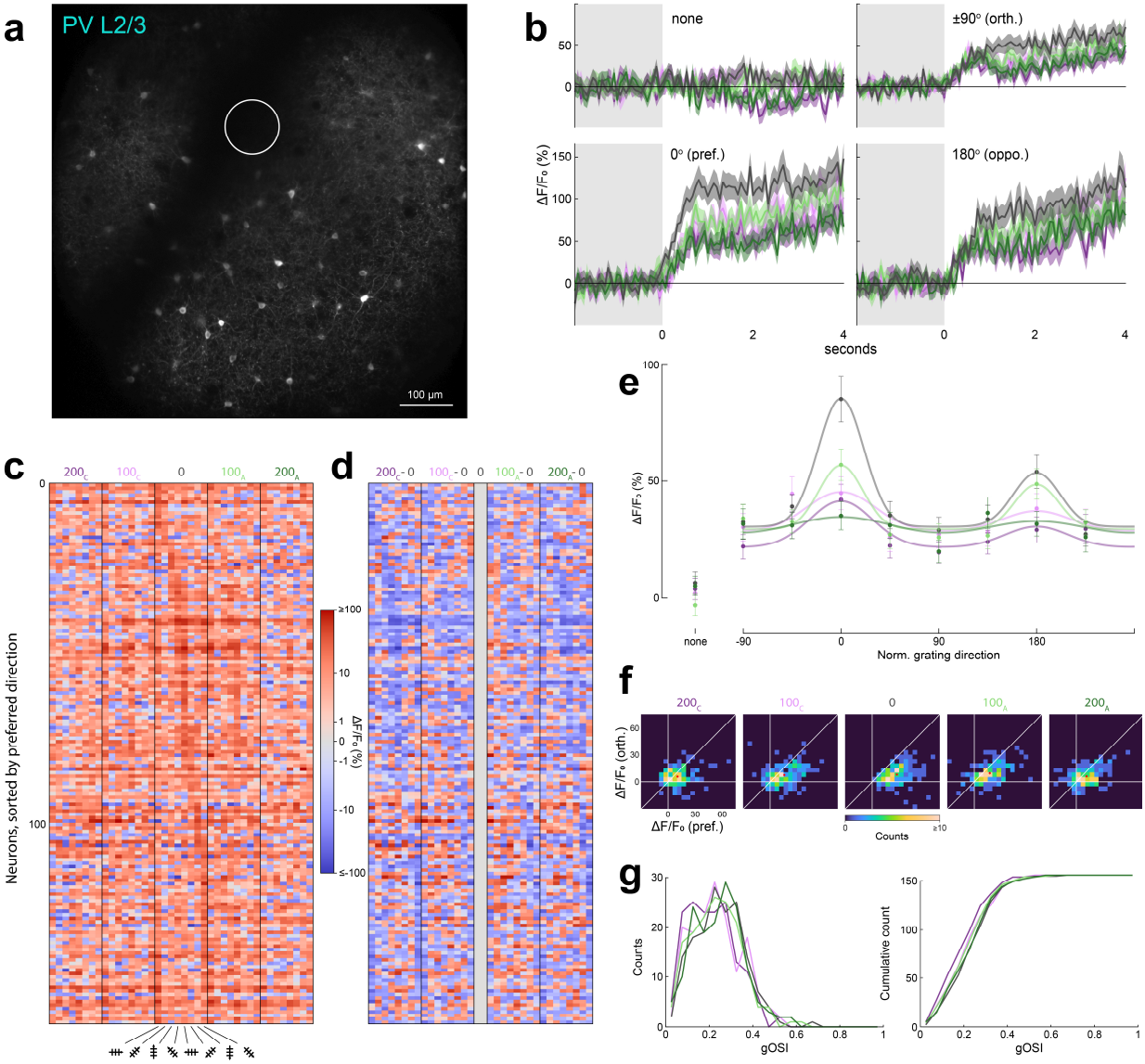

Figure 16. PV INs are not excited by brain surface electrical stimulation

(A) Averaged image of two-photon calcium fluorescence at an example FOV of a PV-Cre mouse, 180 µm below electrode surface. The drawn circle represents the X-Y extent of the brain-surface stimulating electrode contact. **(B)** Mean fluorescence traces for all visually-evoked L2/3 PV INs (N = 156) separated into 4 visual stimulation conditions, like in Fig. 13c. SEM shaded. **(C-G)** Similar analyses to Fig. 13D-H, using the early response of visually-evoked L2/3 PV INs. **(C,D)** Heatmaps showing response strength and difference between electrically-stimulated and non-electrically-stimulated responses. **(E)** Population mean tuning curve. **(F)** 2D histograms of neurons' preferred vs. orthogonal responses. The average of the data is represented with a red circle. **(G)** Histogram and cumulative distribution of neurons' gOSIs, separated by electrical stimulation strengths.

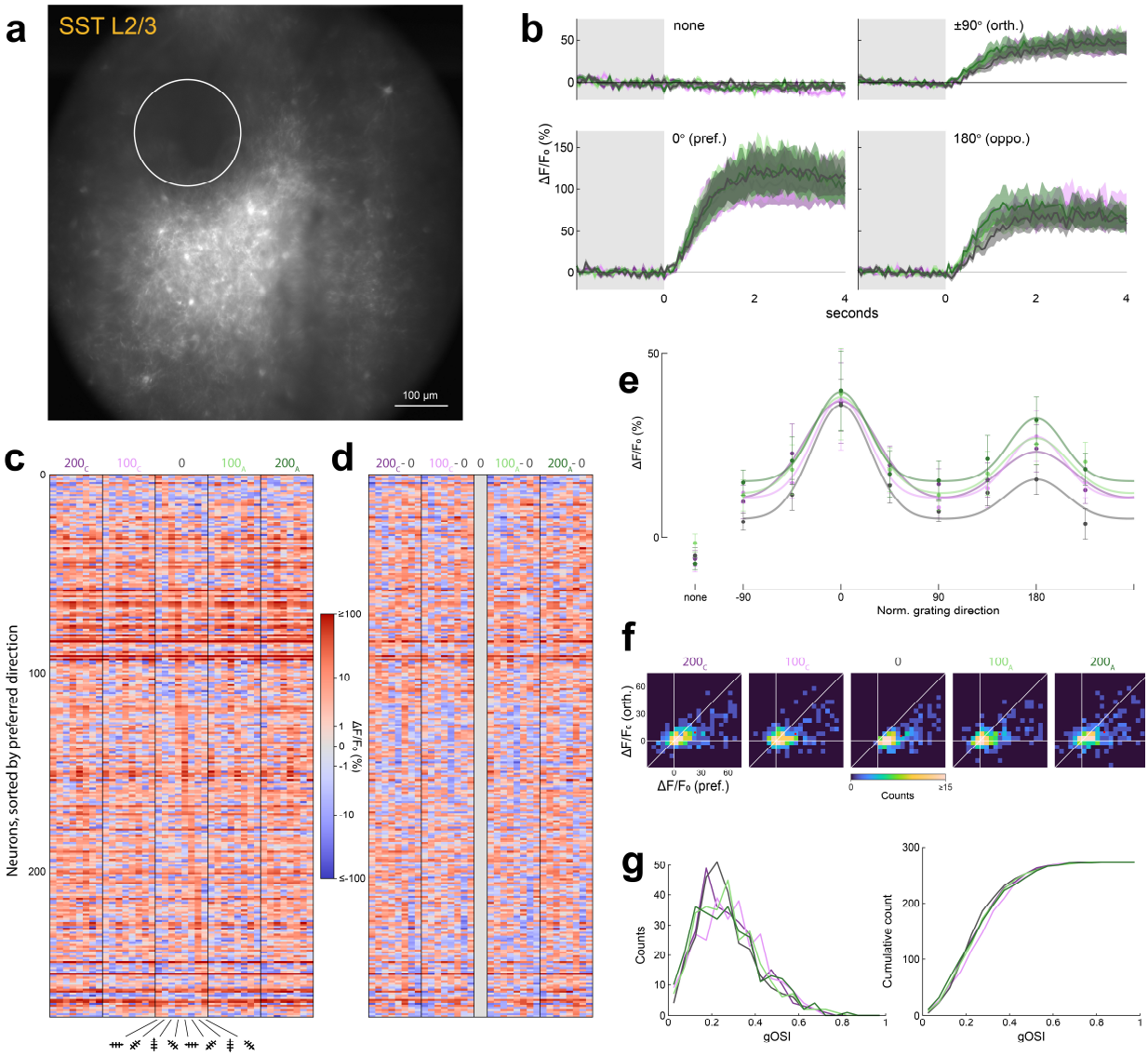

Figure 17. SST INs are weakly excited by electrical stimulation only in the presence of visual stimuli

(A) Averaged image of Bessel two-photon calcium fluorescence at an example FOV of an SST-Cre mouse, 200 µm below electrode surface. The drawn circle represents the X-Y extent of the brain-surface stimulating electrode contact. **(B)** Mean fluorescence traces for all visually-evoked L2/3 SST INs (N = 274) separated into 4 visual stimulation conditions, like in Fig. 13c. SEM shaded. **(C-G)** Similar analyses to Fig. 13D-H, using the early response of visually-evoked L2/3 SST INs. **(C,D)** Heatmaps showing response strength and difference between electrically-stimulated and non-electrically-stimulated responses. **(E)** Population mean tuning curve. **(F)** 2D histograms of neurons' preferred vs. orthogonal responses. The average of the data is represented with a red circle. **(G)** Histogram and cumulative distribution of neurons' gOSIs, separated by electrical stimulation strengths.

4.3.5 SST interneurons are weakly excited by electrical stimulation only in the presence of visual stimuli

Since PV INs innervated the basal dendrites of PNs within L2/3 and were not directly activated by electrical stimulation, we hypothesized that PNs were being modulated via the electrical perturbation of the inputs to their apical dendrites in L1. Supporting this hypothesis, electrical stimulation had been shown to primarily target local axon segments[21,142,143], which would be in L1 given our electrode location. Martinotti cells, which are somatostatin-expressing (SST), project their axons to L1 and are one of the main inhibitory inputs to PN apical dendrites. For this reason, we measured electrical and visual stimulation-induced responses in SST INs (5 animals, 21 FOVs total, example FOV shown in Fig. 17a). Due to the exceptional sparsity of SST-labeled cell bodies in V1 L2/3, we used a fast volumetric imaging method called Bessel 2PFM[52] to improve data throughput (see section 2.1.3, Methods section 4.2.2).

Like PV INs, we did not observe any direct electrical stimulation-triggered responses in our L2/3 SST IN population (Fig. 17b). We did however observe a significant electrical stimulation-induced

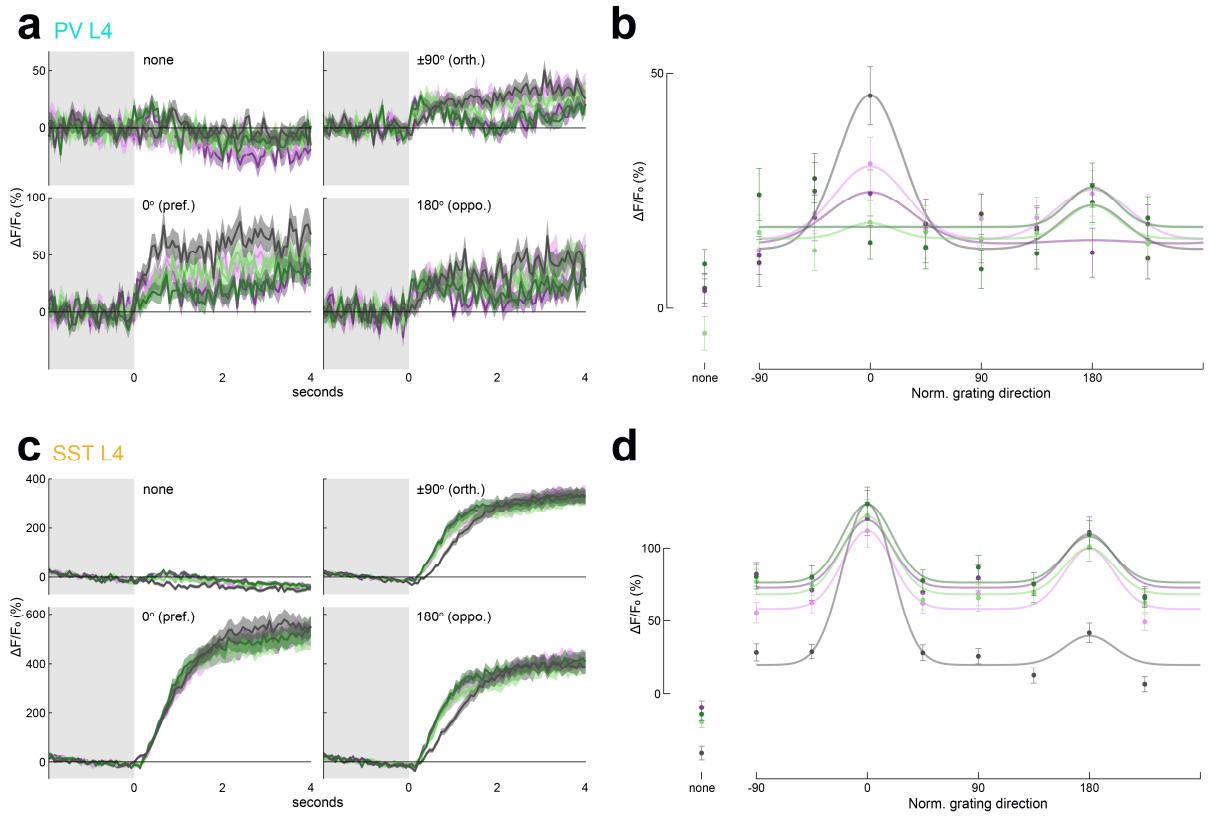

Figure 18. L4 INs responded similarly to L2/3 INs during electrical and visual stimulation.

(A) Mean fluorescence traces for all visually-evoked L4 PV INs (N = 133) separated into 4 visual stimulation conditions, like in Fig. 16b. SEM shaded. **(B)** Population mean tuning curve of L4 PV INs, like in Fig. 16e. **(C,D)** Mean fluorescence traces and population tuning curves for all visually-evoked L4 SST INs (N = 413).

response increase which was only present during visual stimulus presentation, specifically orthogonal and opposite directions. Early response for all visually responsive L2/3 SST INs (N=274), sorted by their preferred direction, were shown in Fig. 17c. Many SST INs were orientation and direction tuned, and tuning seemed to be disrupted by electrical stimulation, but to a relatively lesser degree than WT and PV neurons. Subtracting the visual-only response revealed mostly electrical stimulation-evoked excitation, with preferred direction responses that were both excited and suppressed by electrical stimulation (Fig. 17d). The population mean tuning curve showed an overall electrical stimulation-induced increase of early response, except at the preferred direction, where activation and suppression balanced out and resulted in little mean change (Fig. 17e, Table 1). 2D histograms of preferred vs. orthogonal response showed an increase of orthogonal response due to electrical stimulation (Fig. 17f). Electrically evoked weak activation of L2/3 SST INs did not considerably change their gOSI distribution (Fig. 17g). One mechanism to explain the observation of weak electrical activation only during visual stimulus presentation could be subthreshold activation. Axon segments of SST INs were directly activated by electrical stimulation but were too weak to induce cell body firing. However, with enough internal drive from visual stimulation, the direct activation with electrical stimulation was observed as an increase over normal firing rate. Even during orthogonal visual stimulation, enough subthreshold depolarization was present[164,165,8] to bring cells over the firing threshold. For both PV and SST cell types, we measured activity in the deeper L4 and observed the same response signatures (Fig. 18).

4.3.6 NDNF interneurons in layer 1 are directly activated by electrical stimulation, overriding their visual response

Aside from SST INs, another inhibitory cell type projected to PN apical dendrites are L1 neurogliaform (NGF) cells, which could be the source of the observed sensory input strength-dependent inhibition of putative PNs. NGF cells were imaged using the neuron-derived neurotrophic factor (NDNF) protein as a transgenic label[166] (3 animals, 15 FOVs total, example FOV shown in Fig. 19a). Unlike the previous IN subtypes, NDNF INs showed immediate and strong activation from electrical stimulation in the absence of visual stimulation (Fig. 19b, N = 884). Electrical stimulation-evoked activity in NDNF INs mirrored that of PNs: fast rising dynamics and a reversal to suppression after the first second. Mean early response of NDNF INs during electrical stimulation were significantly greater than no stimulation (Fig. 19c, 200C: p=3.4E-23, 100C: p=2.4E-16, 100A: p=5.8E-14, 200A: p=3.5E-27, two-sample KS-test), but there were no differences between cathode-leading and anode-leading responses (Fig. 19c, 200 µA: p = 0.90, 100 µA: p = 0.64). Like with PNs, we observed a correlation between NDNF INs' early response strength and its distance from the center of the stimulating electrode, for all electrical stimulation conditions (anode-leading 200 µA data shown in Fig. 19d,e, $p = 4.4 \times 10^{-5}$).

Looking at visually-evoked NDNF INs (N = 185), responses to electrical stimulation were qualitatively similar for all visual stimuli (Fig. 19f), even though in the absence of electrical stimulation, NDNF INs exhibited strong direction tuning. Early responses for NDNF INs sorted by their preferred direction showed a diagonal line of positive fluorescence response (no electrical stimulation, middle column) suggesting most of these neurons were direction tuned (Fig. 19g), consistent with previous findings[167]. These same neurons showed no direction tuning for 100 or

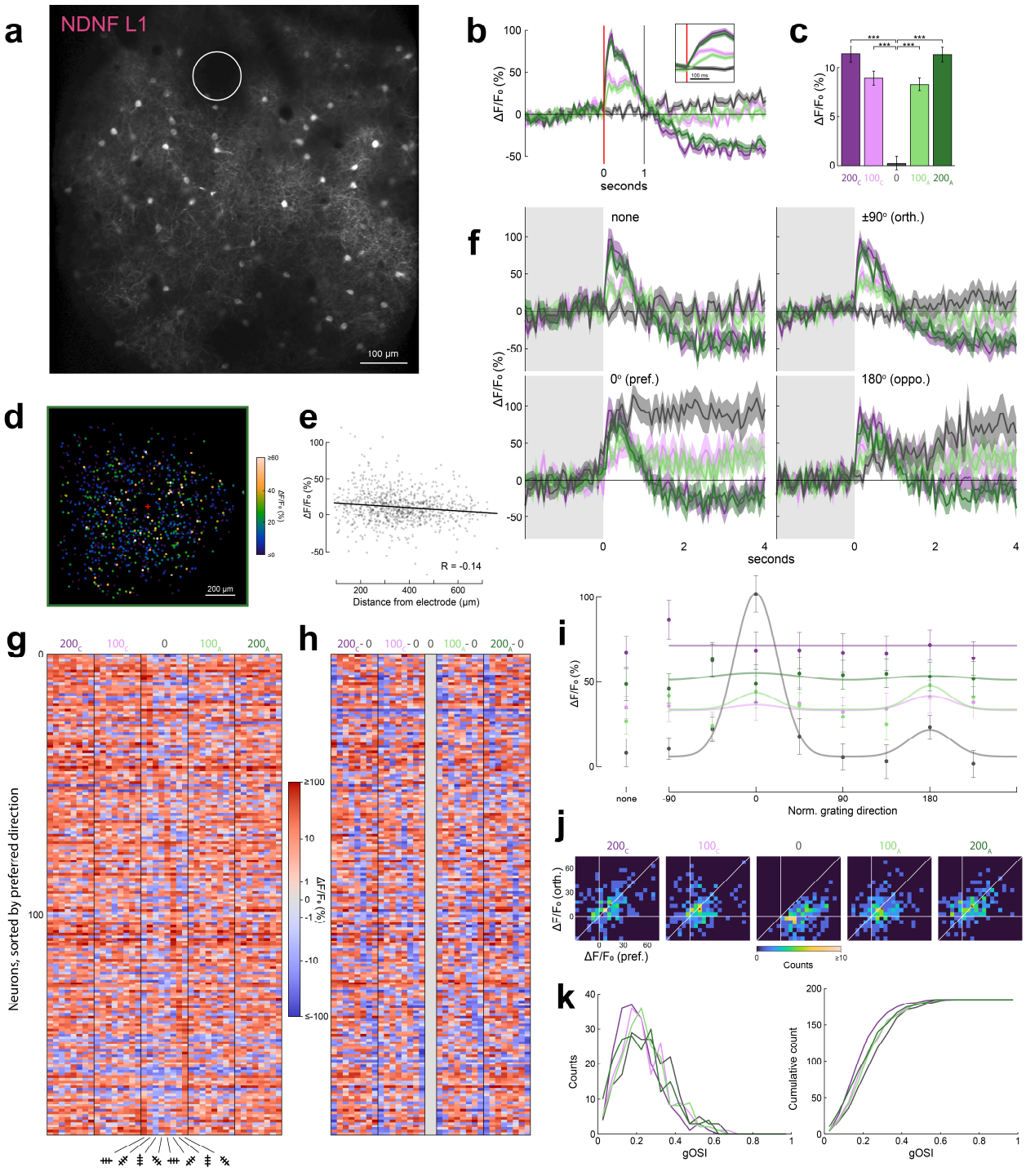

Figure 19. NDNF INs in layer 1 are directly activated by electrical stimulation regardless of visual input

Figure 19 captions.

(A) Averaged image of two-photon calcium fluorescence at an example FOV of a NDNF-Cre mouse, 90 μm below electrode surface. The drawn circle represents the X-Y extent of the brain-surface stimulating electrode contact. **(B)** Mean 15 Hz fluorescence traces over all NDNF neurons (N = 884) in response to an electrical stimulation pulse (red bar). Traces are colored by stimulation strength. SEM shaded. Inset shows traces zoomed in at the time of electrical stimulation. **(C)** Mean of the early response, showing significant response differences between stimulation and no stimulation conditions. **(D)** Early response to 200 μA anode-first stimulation, plotted by lateral distance from stimulation source (electrode contact center represented by red "+") for all NDNF neurons. **(E)** Data from D plotted vs. 3D distance from electrode contact center. There is a significant ($p < 0.001$) linear correlation between cell body distance from electrode and response strength for all electrical stimulation conditions (data only shown for 200 μA anode-first stimulation). **(F)** Mean fluorescence traces for all visually-evoked NDNF INs (N = 185) separated into 4 visual stimulation conditions, like in Fig. 13c. SEM shaded. **(G-K)** Similar analyses to Fig. 13D-H, using the early response of visually-evoked NDNF INs. **(G,H)** Heatmaps showing response strength and difference between electrically-stimulated and non-electrically-stimulated responses. **(I)** Population mean tuning curve. **(J)** 2D histograms of neurons' preferred vs. orthogonal responses. The average of the data is represented with a red circle. **(K)** Histogram and cumulative distribution of neurons' gOSIs, separated by electrical stimulation.

200 μA stimulation conditions, and elevated response at all non-preferred visual stimuli (Fig. 19g,h). The population mean tuning curve summarized the results from Fig. 19f-h, showing strong direction tuning without electrical stimulation, but flat, elevated tuning curves in the presence of electrical stimulation (Fig. 19i, Table 1). 200 μA stimulation pulses consistently activated NDNF INs more than 100 μA pulses. Like with PNs, 2D histograms showed both a reduction of preferred direction response and increase of orthogonal orientation response (Fig. 19j). As expected, population gOSIs were significantly reduced due to electrical stimulation (Fig. 19k). The discovery of this electrical stimulation-triggered inhibitory response suggested a mechanism by which stimulated NDNF INs inhibited the preferred responses of PNs via their apical dendrites. Indeed, previous studies have implicated NDNF INs in contextual modulation of PNs[167,168]. The late suppression effect, which was observed after the first second of response and lasted throughout the response period, was present in PNs, PV INs, and NDNF INs. One mechanism for this effect could have been extracellular volume transmission of GABA by NDNF INs[169–171].

4.3.7 Circuit mechanisms during cortical electrical stimulation and concurrent visual stimulation

Fig. 20 shows our hypothesized circuit model which summarizes mechanisms suggested by our experimental data in this study. Electrical stimulation pulses introduced in the absence of visual stimuli activated NDNF INs and PNs likely through direct antidromic activation of axon segments (Fig. 20a). SST INs also projected their axons to L1, but we did not observe direct activation in their somas, which suggested that electrical activation of SST axons was subthreshold. In contrast, the subthreshold electrical activation of SST became suprathreshold when visual drifting grating stimuli were introduced concurrently with electrical stimulation (Fig. 20b). When visual stimuli were at the orthogonal, non-preferred direction, PNs behaved similarly to when no visual stimuli

were presented at all. However, when visual stimuli were presented at the preferred direction of PNs, their visually-driven activity were markedly suppressed, which indirectly suppressed the preferred response in PV INs (Fig. 20c). The mechanism for this direction-specific suppression was likely due to L1's sensory context-dependent inhibitory control of PN apical dendrites. Electrical activation of NDNF INs, which was visually-independent, only suppressed PNs at their preferred orientations due to the stronger synaptic connection in those sensory contexts. Lastly, our observations of slow activity suppression in PNs and NDNF INs could be attributed to volume transmission of GABA from the early electrical activation of NDNF INs, which indiscriminately inhibited local dendrites (Fig. 20d). SST INs were not suppressed because extracellular GABA did not reach their dendrites, while PV INs were indirectly suppressed due to their inputs from local PNs.

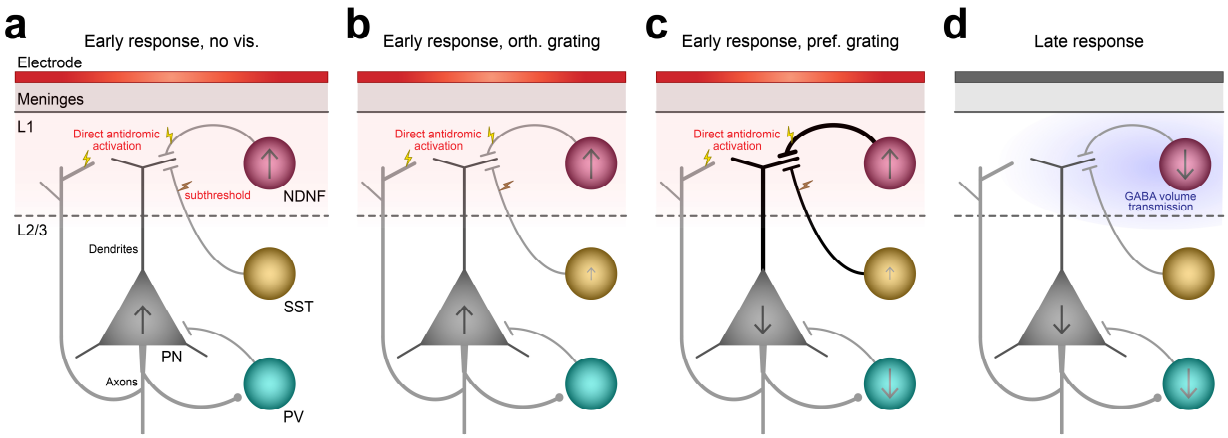

Figure 20. Circuit mechanisms during cortical electrical stimulation and concurrent visual stimulation

Hypothesized circuit model summarizing mechanisms suggested by experimental data in this study. The electrode is above the meningeal layers over mouse V1. Gray, cyan, yellow, and magenta objects represent PNs, PV, SST, and NDNF INs. Arrows within cells represent relative responses of the cell population compared to responses in the absence of electrical stimulation. Lightly shaded red represents the electrode stimulation pulse's suggested region of influence. Yellow lightning bolts represent direct antidromic activation, while orange lightning bolts represent direct subthreshold activation. **(A)** Circuit behavior during early response, in the absence of visual stimulation. Both PNs and NDNF INs are directly activated. **(B)** Circuit behavior during early response, in the presence of an orthogonal visual stimulus. Both PNs and NDNF INs are directly activated, while SST INs are weakly activated due to visual stimulation revealing subthreshold effects. **(C)** Circuit behavior during early response, in the presence of a preferred visual stimulus. NDNF INs are directly activated, which suppresses the preferred response of PNs, resulting in a relative reduction in response in PNs. PV INs are also relatively suppressed as a result of the relative suppression of PNs. **(D)** Circuit behavior during late response shows relative suppression in PNs, NDNF INs, and PV INs. We suggest the role of GABA volume transmission (lightly shaded blue), originating from early NDNF activation, in our observed blanket suppression.

Visual stimulus condition	Electrical stim condition	Two-sample KS test p-values			
		WT	PV L2/3	SST L2/3	NDNF
No visual stimulus	200_C vs. 0	5.6e-85	0.11	0.28	2.9e-8
	100_C vs. 0	6.3e-8	3.8e-4	0.0010	2.8e-4
	100_A vs. 0	3.5e-6	1.7e-5	0.38	0.0022
	200_A vs. 0	1.8e-89	0.023	0.021	0.0015
orthogonal	200_C vs. 0	1.1e-127	0.11	1.1e-5	5.3e-10
	100_C vs. 0	6.7e-20	0.016	0.012	0.019
	100_A vs. 0	5.0e-12	0.63	0.034	0.0047
	200_A vs. 0	2.1e-88	0.18	7.1e-6	1.5e-8
preferred	200_C vs. 0	7.1e-16	1.1e-13	1.9e-6	9.4e-6
	100_C vs. 0	8.8e-62	3.1e-6	1.2e-4	6.2e-11
	100_A vs. 0	1.3e-75	6.1e-4	7.4e-7	3.0e-12
	200_A vs. 0	4.3e-26	4.5e-10	3.7e-4	1.0e-7
opposite	200_C vs. 0	1.6e-38	0.0023	0.16	3.2e-6
	100_C vs. 0	0.0081	0.0077	0.027	0.40
	100_A vs. 0	0.0025	0.63	0.19	0.062
	200_A vs. 0	8.3e-30	0.016	7.5e-4	0.0068

Table 1. Early response p-values of cell populations in different stimulation conditions.

	WT	PV	SST	NDNF
200_C vs. 0	4.9e-54	0.032	0.58	6.9e-5
100_C vs. 0	8.3e-7	0.45	0.0051	0.047
100_A vs. 0	3.9e-5	0.63	0.51	0.22
200_A vs. 0	8.3e-30	0.99	0.33	0.019

Table 2. gOSI significantly reduced with electrical stimulation of WT neurons

Two-sample KS-test p-values comparing gOSI distributions with and without electrical stimulation, for 4 cell populations. Corresponds to Figs. 13h, 16g, 17g, and 19k.

Cell population	# FOVs	Mean	Std
WT	14	0.74	0.05
PV L2/3	6	0.36	0.11
PV L4	6	0.41	0.14
SST L2/3 (Bessel)	8	0.81	0.07
SST L4	12	0.24	0.14
NDNF	15	0.24	0.22

Table 3. Neuropil subtraction coefficients vary between cell types and imaging modality

4.4 Discussion

We designed novel methods for concurrent cortical electrical stimulation using a PtNR electrode array and 2PFM of several neuron subtypes in the awake, behaving mouse. Using single-pulse electrical stimulation, we observed activation in both L2/3 PN and L1 NDNF IN cell populations. In both cell populations, we observed that larger electrical stimulation current evoked larger responses. We also observed a small but significant increase in response to cathode-leading stimulation compared to anode-leading stimulation in L2/3 PNs, but not NDNF INs. In the presence of both sensory input and electrical stimulation, we observed that L2/3 PN orientation selectivity reduced. This effect was a combination of direct PN activation and indirect sensory input strength-dependent suppression. We observed that, in L1 NDNF INs, electrical stimulation

response overrode the sensory-evoked response. From our observations, we suggest that strong activation of L1 NDNF INs resulted in the sensory-dependent suppression of L2/3 PNs. Finally, we demonstrated that both SST and PV INs showed delayed responses, suggesting that they were not directly, but rather indirectly, activated by electrical stimulation within the cortical circuit.

The methods and experiments detailed in this study represented the beginning of a new foray into studying the cortical effects of electrical stimulation. A specific focus on methods which enabled clinical translation, combined with a holistic approach to neural data collection with cell type-specificity and both electrical and sensory stimuli, allowed us to collect a unique dataset which yielded novel biological findings. By using surface electrodes analogous to human ECoG arrays, we hoped to provide translational insight on how electrical stimulation could enhance or disrupt sensory responses. A single stimulation pulse, as opposed to a stimulation train, at the onset of the visual stimulus was used to simplify the interpretation of responses by removing electrical stimulation-caused steady-state effects. This allowed us to observe and differentiate between short-term and long-term effects caused by a perturbation at a discreet point in time. Single stimulation pulses, if successful in perturbing neural responses, could replace stimulation trains as a sparser, more temporally precise intervention which could reduce the overall charge injected into a human brain for a given desired response, therefore being potentially safer on brain tissue and saving on implant battery life. Choices to use surface stimulating electrodes and single pulse stimulation both had the goals of translation and minimization of invasiveness. To our best knowledge, neither have been demonstrated during measurement of neural activity *in vivo*.

We took three steps towards the goal of observing a holistic picture of neural responses to electrical stimulation. First, we imaged chronically implanted awake mice. By giving the mice time to heal post-surgery and imaging in an awake state, we avoided unnatural brain activity caused by anesthesia, which would have confounded our neural recording results. Second, we included visual stimulation in our experimental setup. Since we were imaging the mouse V1 and knew that many neurons preferentially responded to specific directions of visual drifting gratings, we were able to contrast the naturally driven sensory response of these neurons in the presence or absence of artificially introduced electrical stimulation. A dataset with awake and sensory-driven neural activity was a more realistic framework to study the effects of electrical stimulation, so the results may be more clinically relevant to modulating or rescuing human senses. Third, we collected cell type-specific data on multiple inhibitory neuron subtypes, which allowed us to differentiate between cortical circuit mechanisms of inhibition and how they were affected by electrical stimulation. To our best knowledge, the effects of electrical stimulation on sensory-driven neural activity or inhibitory neuron subtypes have not been previously demonstrated.

In the short time scale, electrically stimulated excitation of NDNF likely explained the inhibition of PNs at their preferred orientations, as previously demonstrated by Malina et al. in optogenetic experiments[167]. A combination of context-dependent inhibition from NDNF INs and direct excitation from electrical stimulation resulted in PNs exhibiting reduced orientation selectivity as reported by their gOSI values. Due to our course sampling of visual stimulation angles, we were unable to discern changes in PN tuning width, which would have shed light on whether or not apical dendritic inhibition disrupted the ability for the animal to discriminate between grating directions. A previous study showed that ablation of apical dendrites did not affect any orientation

tuning parameters[172]. Future verification of this form of interrogation using finer sampling of visual stimulation angles and behavioral tests would further shed light on electrical stimulation's clinical utility of disrupting or rescuing sensory function.

The effect of electrical stimulation on L2/3 SST INs was unique since a difference in response was seen only in the presence of visual stimulation. This effect could be explained by weak subthreshold direct activation. Because Martinotti cells, which made up most of the L2/3 SST population, projected their axons into L1, it was likely that some of these axons were directly activated by electrical stimulation. Due to the threshold required to translate axonal activity to calcium activity in the soma, only during visually driven activity did we observe the electrical stimulation effect. Since visually driven activity ramped slowly, so too did our observed electrical stimulation effect. The difference in response between SST and NDNF INs, despite both being L1-projecting, was likely due to a difference in density, positioning, and sensitivity of neural processes, as well as integration of input signals. An alternative explanation for the responses observed in SST INs would involve their upstream inputs. SST INs exhibited visually evoked activity due to integration of their visually evoked inputs, including local PNs, and those inputs may have been activated by electrical stimulation. Regardless of the mechanism, electrical activation of SST INs was too delayed to be the inhibitory source directly impacting our PN findings.

A theme observed across PNs, PV INs, and NDNF INs was a delayed, seconds-long inhibition from a single electrical stimulation pulse. Long periods of inhibition after the end of electrical stimulation was observed in excitatory neurons in previous studies[149], but the mechanism was not known. Here, we proposed that NDNF INs, directly activated by electrical stimulation, played a key role in the long-term inhibition of cells in layers 1-3 via extracellular release of GABA neurotransmitters. It has been known that L1 INs projected to and inhibit most cortical neuron subtypes from L1-3[173]. Importantly, and with support from our results, NDNF INs did not directly inhibit SST INs in the mouse V1[167]. However, L1 INs have been shown to evoke long-lasting network inhibition through volume transmission (non-synaptic release) of both $GABA_A$ and $GABA_B$ neurotransmitters[167,169,170,174]. The idea that long-term inhibitory effects were the result of GABA volume transmission coincided with our observation of early direct electrical activation of NDNF INs. Validation of this hypothesis would require further experiments using tools such as chemogenetic knockout of GABA volume transmission and/or fluorescent GABA sensors[175].

We observed that inhibitory subtypes NDNF, SST, and PV, like PNs, exhibited orientation tuning. PV and SST INs were broadly responsive to all orientations as was observed with their non-zero responses to orthogonal visual stimulation in the absence of electrical stimulation. NDNF INs were responsive only at their preferred orientations, like PNs. Responses to drifting grating visual stimulation without electrical stimulation in all neuron types were consistent with previous literature[58,162,167,176,177]. In the presence of electrical stimulation, direction preference in both PV and NDNF INs was heavily reduced. Aside from the previously mentioned reciprocal connections between PNs and PV INs, another mechanism for the context-dependent inhibition of PV INs could be that NDNF – PV connections shared preferred tuning directions, and NDNF tuning was abolished during electrical stimulation. The mechanism which abolished NDNF IN orientation

tuning at large electrical stimulation currents remains unclear, but could feasibly be credited to GABA volume transmission, where NDNF INs self-suppress. L1 INs were also shown to innervate onto each other in a previous study[166]. SST INs were indiscriminately activated by what was likely a subthreshold direct activation effect but did not show differences in response at their preferred orientations, suggesting a counteracting suppression effect. Suppression of SST response at preferred orientations could be a result of reduced orientation-specific inputs from local PNs, like the proposed mechanism for PV IN suppression.

4.4.1 Experimental method design and future work

Towards understanding the transformation of electrical stimulation input to neural activity output, we varied two stimulation parameters: strength and polarity. As expected, stimulation strength dictated the magnitude of neural response. Weaker stimulation resulted in weaker direct activation of PNs and NDNF INs, as well as weaker slow suppression of PNs, PV INs, and NDNF INs. Interestingly, although weak electrical stimulation directly activated PNs less than strong stimulation, it inhibited PNs roughly equally at their preferred directions over the first second (Fig. 13f). Since PN inhibition was likely a result of NDNF IN activation, we hypothesize that NDNF INs should be more sensitive to electrical stimulation than PNs. Further experimentation at finer granularity of stimulation currents would be needed to address this point. In our experimental design, we also tested for differences between stimulation polarities. Here, we observed a small but significant response increase in PN direct activation for cathode-leading stimulation pulses (Fig. 12g). This was consistent with previous findings in mice[149,178] and computational models[150], as well as clinical literature preferring cathode-leading stimulation for greater treatment efficacy. Our small effect difference between cathode and anode-leading pulses was likely due to our use of a single stimulation pulse, rather than a train, since a train of pulses likely amplifies response differences between polarities. Future experiments could utilize a wider gamut of stimulation pulse shapes, especially asymmetric pulses which may amplify polarity differences in the neural data.

This study has revealed a highly complex neural response to a simple, single-pulse electrical perturbation, which fits within a qualitative cortical circuit framework. To provide quantitative predictions and further validate our hypotheses, we would need to design a computational model – one which considers neuronal subtype morphologies and their proximity to the electrode, together with the interconnectivity of these subtypes within the cortex. Existing modeling efforts have focused on NHPs[152,153] and rats[150,151], but not mice, which have the largest genetic toolkit for experimental validation. An ideal computational model would account for the complete cortical circuit, including all major neuronal subtypes in all layers, and include representations of bottom-up sensory input and top-down control. Together with experimental data for model fitting like the data collected in this study, we could eventually use such a model to generate specifically tailored neural activity patterns using brain surface electrode arrays. For applications in clinical therapy, similar stimulation experiments can be performed acutely during human brain surgery, typically for epileptic seizure monitoring, or chronically in paralyzed patients undergoing BCI experiments. Without cell-type specificity, electrophysiological recordings in humans, as well as information about human cortical morphology, could be used to adjust the mouse-based computational model.

Finally, as shown in our results, we imaged at 15 Hz frame rate and observed immediate calcium signal increase in as early as the first imaging frame: what we considered to be direct activation of PNs and NDNF INs. Unfortunately, an inherent limitation to cytosolic calcium signal is its slow dynamics compared to the underlying APs of interest. We used the popular calcium indicator GCaMP6s for its large, sensitive fluorescence response, but it had slow rise and decay dynamics[6]. Recently, two-photon-compatible voltage indicators have been developed to enable optical-based electrophysiological readout with single-AP temporal precision[7,107]. Concurrently, techniques for kilohertz 2PFM have emerged, allowing the measurement of these fast indicators[8]. Excitatory apical dendrites are known to be a source of spike bursting[168], and inhibition could lead to a reduced number of APs per burst, but not necessarily the number of burst events. Voltage imaging would be able to answer this question, along with other AP spike timing subtleties, such as the relative timing of NDNF and PN electrical stimulation-triggered activation. Importantly, voltage imaging has major benefits over traditional electrophysiology: not only does it have access to cell type-specific genetic tools, but it also circumvents the electrical stimulation artifact which has always inherently plagued this field of research.

The experiments presented in this study highlight the value of 2PFM as a tool for measuring cortical response to electrical stimulation. The techniques and findings described here set the stage for future research directions, including characterization of electrical stimulation parameters, modeling of cortical circuit responses, and finer-grain signal measurements using neurotransmitter sensors and voltage indicators.

Chapter 5: Conclusion

Over the last decade, the Ji lab has demonstrated an ability to both develop novel microscopy techniques based on concepts from optical physics[8,52,77,179] and apply these techniques in biological studies[58,180,181]. Similarly, the goals of this thesis were to develop new experimental techniques that better apply 2PFM to clinically relevant topics, and then apply these techniques to better understand the biology of the brain. At the same time, new techniques that can be applied to biological study need to be both markedly better than conventional methods and accessible for researchers, especially ones outside of the lab of origin. To this end, a fundamental goal of this thesis was to develop not only useful, but accessible techniques which allow curious researchers to repeat studies in this thesis and ask new questions that push forward our understanding of the brain and its maladies. Three studies summarizing recent research efforts demonstrated the overarching goals of this thesis.

The first study applied the fast volumetric imaging technique of Bessel 2PFM to neurovasculature imaging using a commercial microscope system. Bessel 2PFM was able to capture volumetric hemodynamics in the awake mouse brain at high spatiotemporal resolution. With the axially extended Bessel focus, the fluorescence signal of a vessel became proportional to its size, which enabled convenient intensity-based analysis of vessel dilation and constriction dynamics in large volumes. This technique was used to observe entrainment of vasodilation and vasoconstriction with pupil diameter, which showed distinct vasculature populations which were correlated and anticorrelated with animal arousal state. Bessel 2PFM also enabled the measurement of 3D blood flow speeds simultaneously in a vessel population which consisted of capillaries conventionally difficult to image. Demonstrating high-throughput monitoring of hemodynamics in the awake brain using an accessible technology, we expect Bessel 2PFM to make broad impacts on neurovasculature research.

The second study built upon the commercial Bessel two-photon fluorescence microscope from the first study by introducing to it both Bessel-droplet and AO functionalities. Importantly, Bessel 2PFM imaging quality was improved using the new techniques without the need to complicate the system with additional optical components. Bessel-droplets were generated using the included SLM and newly designed, easily swappable masks and demonstrated a reduction in fluorescence background excited by Bessel beam side lobes. Without a direct wavefront sensor nor an SLM conjugated to the pupil plane, Bessel AO was possible using a modal-based wavefront sensing approach, taking advantage of the same SLM that generated the Bessel beam to correct for aberrations. Preliminary experiments showed successful correction of system aberrations using modal AO. Further characterization of both Bessel-droplet and modal AO methods using the commercial Bessel 2PFM are necessary to show their effectiveness for biological imaging.

The third study aimed to understand the cortical circuit response to electrical stimulation in the awake, behaving brain. To this end, a set of novel methods were developed which enabled *in vivo* 2PFM imaging of neurons through a chronically implanted brain surface electrode array. Using cell type-specific genetic labeling of mouse V1, electrical stimulation was found to directly activated both excitatory neurons and L1 inhibitory neurons. Furthermore, electrical stimulation

caused the suppression of excitatory neuron activity only at their preferred visual stimuli, likely due to sensory input strength-dependent inhibition at their apical dendrites by the electrically activated L1 inhibitory neuron population. These experimental results revealed a mechanism by which brain surface electrical stimulation could be used to reduce sensory sensitivity with spatiotemporal specificity, which could guide future therapies.

The results from these three studies satisfy the goals originally set out by the thesis. Useful preclinical questions were addressed when 2PFM was combined with novel technologies and used in new ways: When combined with an axially elongated Bessel beam, neurovasculature was able to be imaged at unprecedented throughput. When combined with cortical surface electrical stimulation, electrically evoked neural responses within the cortical circuit were observed. Future work in incorporating additional techniques, especially accessible ones such as Bessel-droplet and modal AO, further enable researchers to ask daring questions in the pursuit of scientific discovery.

Reference

1. Joo HR, Fan JL, Chen S, et al. A microfabricated, 3D-sharpened silicon shuttle for insertion of flexible electrode arrays through dura mater into brain. *J Neural Eng*. 2019;16(6):066021. doi:10.1088/1741-2552/ab2b2e

2. Denk W, Strickler JH, Webb WW. Two-photon laser scanning fluorescence microscopy. *Science*. 1990;248(4951):73-76. doi:10.1126/science.2321027

3. Wu J, Ji N, Tsia KK. Speed scaling in multiphoton fluorescence microscopy. *Nat Photon*. 2021;15(11):800-812. doi:10.1038/s41566-021-00881-0

4. Greenwald EC, Mehta S, Zhang J. Genetically Encoded Fluorescent Biosensors Illuminate the Spatiotemporal Regulation of Signaling Networks. *Chem Rev*. 2018;118(24):11707-11794. doi:10.1021/acs.chemrev.8b00333

5. Lambert TJ. FPbase: a community-editable fluorescent protein database. *Nat Methods*. 2019;16(4):277-278. doi:10.1038/s41592-019-0352-8

6. Chen TW, Wardill TJ, Sun Y, et al. Ultra-sensitive fluorescent proteins for imaging neuronal activity. *Nature*. 2013;499(7458):295-300. doi:10.1038/nature12354

7. Villette V, Chavarha M, Dimov IK, et al. Ultrafast Two-Photon Imaging of a High-Gain Voltage Indicator in Awake Behaving Mice. *Cell*. 2019;179(7):1590-1608.e23. doi:10.1016/j.cell.2019.11.004

8. Wu J, Liang Y, Chen S, et al. Kilohertz two-photon fluorescence microscopy imaging of neural activity in vivo. *Nat Methods*. 2020;17(3):287-290. doi:10.1038/s41592-020-0762-7

9. Chapin JK, Moxon KA, Markowitz RS, Nicolelis MAL. Real-time control of a robot arm using simultaneously recorded neurons in the motor cortex. *Nat Neurosci*. 1999;2(7):664-670. doi:10.1038/10223

10. Wessberg J, Stambaugh CR, Kralik JD, et al. Real-time prediction of hand trajectory by ensembles of cortical neurons in primates. *Nature*. 2000;408(6810):361-365. doi:10.1038/35042582

11. Hochberg LR, Serruya MD, Friehs GM, et al. Neuronal ensemble control of prosthetic devices by a human with tetraplegia. *Nature*. 2006;442(7099):164-171. doi:10.1038/nature04970

12. Collinger JL, Wodlinger B, Downey JE, et al. High-performance neuroprosthetic control by an individual with tetraplegia. *The Lancet*. 2013;381(9866):557-564. doi:10.1016/S0140-6736(12)61816-9

13. Bouton CE, Shaikhouni A, Annetta NV, et al. Restoring cortical control of functional movement in a human with quadriplegia. *Nature*. 2016;533(7602):247-250. doi:10.1038/nature17435

14. Chiueh CC, Markey SP, Burns RS, Johannessen JN, Jacobowitz DM, Kopin IJ. Neurochemical and behavioral effects of 1-methyl-4-phenyl-1,2,3,6- tetrahydropyridine (MPTP) in rat, guinea pig, and monkey. *Psychopharmacol Bull*. 1984;20(3):548-553.

15. Benabid AL, Pollak P, Louveau A, Henry S, de Rougemont J. Combined (thalamotomy and stimulation) stereotactic surgery of the VIM thalamic nucleus for bilateral Parkinson disease. *Appl Neurophysiol*. 1987;50(1-6):344-346. doi:10.1159/000100803

16. Gardner J. A history of deep brain stimulation: Technological innovation and the role of clinical assessment tools. *Soc Stud Sci*. 2013;43(5):707-728. doi:10.1177/0306312713483678

17. Mocking RJT, Graat I, Denys D. Why Has Deep Brain Stimulation Had So Little Impact in Psychiatry? *Frontiers in Neurology*. 2021;12. Accessed October 12, 2022. https://www.frontiersin.org/articles/10.3389/fneur.2021.757142

18. Tissue Plasminogen Activator for Acute Ischemic Stroke (Alteplase, Activase®) | National Institute of Neurological Disorders and Stroke. Accessed October 12, 2022. https://www.ninds.nih.gov/about-ninds/impact/ninds-contributions-approved-therapies/tissue-plasminogen-activator-acute-ischemic-stroke-alteplase-activaser

19. Barreto AD. Intravenous Thrombolytics for Ischemic Stroke. *Neurotherapeutics*. 2011;8(3):388-399. doi:10.1007/s13311-011-0049-x

20. Zhang S, Boyd J, Delaney K, Murphy TH. Rapid Reversible Changes in Dendritic Spine Structure In Vivo Gated by the Degree of Ischemia. *J Neurosci*. 2005;25(22):5333-5338. doi:10.1523/JNEUROSCI.1085-05.2005

21. Histed MH, Bonin V, Reid RC. Direct Activation of Sparse, Distributed Populations of Cortical Neurons by Electrical Microstimulation. *Neuron*. 2009;63(4):508-522. doi:10.1016/j.neuron.2009.07.016

22. Luan L, Wei X, Zhao Z, et al. Ultraflexible nanoelectronic probes form reliable, glial scar–free neural integration. *Science Advances*. 2017;3(2):e1601966. doi:10.1126/sciadv.1601966

23. Fan JL, Rivera JA, Sun W, et al. High-speed volumetric two-photon fluorescence imaging of neurovascular dynamics. *Nat Commun*. 2020;11(1):6020. doi:10.1038/s41467-020-19851-1

24. Devor A, Tian P, Nishimura N, et al. Suppressed Neuronal Activity and Concurrent Arteriolar Vasoconstriction May Explain Negative Blood Oxygenation Level-Dependent Signal. *J Neurosci*. 2007;27(16):4452-4459. doi:10.1523/JNEUROSCI.0134-07.2007

25. Petzold GC, Albeanu DF, Sato TF, Murthy VN. Coupling of Neural Activity to Blood Flow in Olfactory Glomeruli Is Mediated by Astrocytic Pathways. *Neuron*. 2008;58(6):897-910. doi:10.1016/j.neuron.2008.04.029

26. Drew PJ, Shih AY, Kleinfeld D. Fluctuating and sensory-induced vasodynamics in rodent cortex extend arteriole capacity. *Proceedings of the National Academy of Sciences*. 2011;108(20):8473-8478. doi:10.1073/pnas.1100428108

27. Ogawa S, Lee TM, Kay AR, Tank DW. Brain magnetic resonance imaging with contrast dependent on blood oxygenation. *Proceedings of the National Academy of Sciences*. 1990;87(24):9868-9872. doi:10.1073/pnas.87.24.9868

28. Gagnon L, Sakadžić S, Lesage F, et al. Quantifying the Microvascular Origin of BOLD-fMRI from First Principles with 2-photonscopy and an Oxygen-Sensitive Nanoprobe. *J Neurosci*. 2015;35(8):3663-3675. doi:10.1523/JNEUROSCI.3555-14.2015

29. Logothetis NK, Pauls J, Augath M, Trinath T, Oeltermann A. Neurophysiological investigation of the basis of the fMRI signal. *Nature*. 2001;412(6843):150-157. doi:10.1038/35084005

30. Vanzetta I, Grinvald A. Increased Cortical Oxidative Metabolism Due to Sensory Stimulation: Implications for Functional Brain Imaging. *Science*. 1999;286(5444):1555-1558. doi:10.1126/science.286.5444.1555

31. Shih AY, Friedman B, Drew PK, Tsai PS, Lyden PD, Kleinfeld D. Active Dilation of Penetrating Arterioles Restores Red Blood Cell Flux to Penumbral Neocortex after Focal Stroke. *J Cereb Blood Flow Metab*. 2009;29(4):738-751. doi:10.1038/jcbfm.2008.166

32. Shih AY, Blinder P, Tsai PS, et al. The smallest stroke: occlusion of one penetrating vessel leads to infarction and a cognitive deficit. *Nat Neurosci*. 2013;16(1):55-63. doi:10.1038/nn.3278

33. Huang JY, Li LT, Wang H, et al. In Vivo Two-photon Fluorescence Microscopy Reveals Disturbed Cerebral Capillary Blood Flow and Increased Susceptibility to Ischemic Insults in Diabetic Mice. *CNS Neuroscience & Therapeutics*. 2014;20(9):816-822. doi:10.1111/cns.12268

34. Lee S, Kang BM, Kim JH, et al. Real-time in vivo two-photon imaging study reveals decreased cerebro-vascular volume and increased blood-brain barrier permeability in chronically stressed mice. *Sci Rep*. 2018;8(1):13064. doi:10.1038/s41598-018-30875-y

35. Winkler EA, Nishida Y, Sagare AP, et al. GLUT1 reductions exacerbate Alzheimer's disease vasculo-neuronal dysfunction and degeneration. *Nat Neurosci*. 2015;18(4):521-530. doi:10.1038/nn.3966

36. Sweeney MD, Sagare AP, Zlokovic BV. Blood–brain barrier breakdown in Alzheimer disease and other neurodegenerative disorders. *Nat Rev Neurol*. 2018;14(3):133-150. doi:10.1038/nrneurol.2017.188

37. Cruz Hernández JC, Bracko O, Kersbergen CJ, et al. Neutrophil adhesion in brain capillaries reduces cortical blood flow and impairs memory function in Alzheimer's disease mouse models. *Nat Neurosci*. 2019;22(3):413-420. doi:10.1038/s41593-018-0329-4

38. Grinvald A, Lieke E, Frostig RD, Gilbert CD, Wiesel TN. Functional architecture of cortex revealed by optical imaging of intrinsic signals. *Nature*. 1986;324(6095):361-364. doi:10.1038/324361a0

39. Berwick J, Martin C, Martindale J, et al. Hemodynamic Response in the Unanesthetized Rat: Intrinsic Optical Imaging and Spectroscopy of the Barrel Cortex. *J Cereb Blood Flow Metab*. 2002;22(6):670-679. doi:10.1097/00004647-200206000-00005

40. Sirotin YB, Das A. Anticipatory haemodynamic signals in sensory cortex not predicted by local neuronal activity. *Nature*. 2009;457(7228):475-479. doi:10.1038/nature07664

41. Shih AY, Driscoll JD, Drew PJ, Nishimura N, Schaffer CB, Kleinfeld D. Two-Photon Microscopy as a Tool to Study Blood Flow and Neurovascular Coupling in the Rodent Brain. *J Cereb Blood Flow Metab*. 2012;32(7):1277-1309. doi:10.1038/jcbfm.2011.196

42. Kleinfeld D, Mitra PP, Helmchen F, Denk W. Fluctuations and stimulus-induced changes in blood flow observed in individual capillaries in layers 2 through 4 of rat neocortex. *Proceedings of the National Academy of Sciences*. 1998;95(26):15741-15746. doi:10.1073/pnas.95.26.15741

43. Kleinfeld D, Blinder P, Drew P, et al. A Guide to Delineate the Logic of Neurovascular Signaling in the Brain. *Frontiers in Neuroenergetics*. 2011;3. Accessed December 1, 2022. https://www.frontiersin.org/articles/10.3389/fnene.2011.00001

44. Tang P, Zhang Y, Chen C, et al. In Vivo Two-Photon Imaging of Axonal Dieback, Blood Flow and Calcium Influx withMethylprednisolone Therapy after Spinal Cord Injury. *Sci Rep*. 2015;5(1):9691. doi:10.1038/srep09691

45. Kelly P, Hudry E, Hou SS, Bacskai BJ. In Vivo Two Photon Imaging of Astrocytic Structure and Function in Alzheimer's Disease. *Frontiers in Aging Neuroscience*. 2018;10. Accessed December 1, 2022. https://www.frontiersin.org/articles/10.3389/fnagi.2018.00219

46. Shen Z, Lu Z, Chhatbar PY, O'Herron P, Kara P. An artery-specific fluorescent dye for studying neurovascular coupling. *Nat Methods*. 2012;9(3):273-276. doi:10.1038/nmeth.1857

47. O'Herron P, Chhatbar PY, Levy M, et al. Neural correlates of single-vessel haemodynamic responses in vivo. *Nature*. 2016;534(7607):378-382. doi:10.1038/nature17965

48. Blinder P, Tsai PS, Kaufhold JP, Knutsen PM, Suhl H, Kleinfeld D. The cortical angiome: an interconnected vascular network with noncolumnar patterns of blood flow. *Nat Neurosci*. 2013;16(7):889-897. doi:10.1038/nn.3426

49. Botcherby EJ, Juškaitis R, Wilson T. Scanning two photon fluorescence microscopy with extended depth of field. *Optics Communications*. 2006;268(2):253-260. doi:10.1016/j.optcom.2006.07.026

50. Thériault G, Cottet M, Castonguay A, McCarthy N, De Koninck Y. Extended two-photon microscopy in live samples with Bessel beams: steadier focus, faster volume scans, and simpler stereoscopic imaging. *Front Cell Neurosci*. 2014;8:139. doi:10.3389/fncel.2014.00139

51. Thériault G, Koninck YD, McCarthy N. Extended depth of field microscopy for rapid volumetric two-photon imaging. *Opt Express, OE*. 2013;21(8):10095-10104. doi:10.1364/OE.21.010095

52. Lu R, Sun W, Liang Y, et al. Video-rate volumetric functional imaging of the brain at synaptic resolution. *Nat Neurosci*. 2017;20(4):620-628. doi:10.1038/nn.4516

53. Lu R, Tanimoto M, Koyama M, Ji N. 50 Hz volumetric functional imaging with continuously adjustable depth of focus. *Biomed Opt Express, BOE*. 2018;9(4):1964-1976. doi:10.1364/BOE.9.001964

54. Rodríguez C, Liang Y, Lu R, Ji N. Three-photon fluorescence microscopy with an axially elongated Bessel focus. *Opt Lett, OL*. 2018;43(8):1914-1917. doi:10.1364/OL.43.001914

55. Meng G, Liang Y, Sarsfield S, et al. High-throughput synapse-resolving two-photon fluorescence microendoscopy for deep-brain volumetric imaging in vivo. Marder E, Kleinfeld D, eds. *eLife*. 2019;8:e40805. doi:10.7554/eLife.40805

56. Meng G. *High-Throughput Volumetric Imaging of Neural Dynamics in Vivo*. UC Berkeley; 2021. Accessed October 13, 2022. https://escholarship.org/uc/item/21m0q3wp

57. Welford WT. Use of Annular Apertures to Increase Focal Depth. *J Opt Soc Am, JOSA*. 1960;50(8):749-753. doi:10.1364/JOSA.50.000749

58. Sun W, Tan Z, Mensh BD, Ji N. Thalamus provides layer 4 of primary visual cortex with orientation- and direction-tuned inputs. *Nat Neurosci*. 2016;19(2):308-315. doi:10.1038/nn.4196

59. Chhatbar P, Kara P. Improved blood velocity measurements with a hybrid image filtering and iterative Radon transform algorithm. *Frontiers in Neuroscience*. 2013;7. Accessed December 1, 2022. https://www.frontiersin.org/articles/10.3389/fnins.2013.00106

60. Mayhew JEW, Askew S, Zheng Y, et al. Cerebral Vasomotion: A 0.1-Hz Oscillation in Reflected Light Imaging of Neural Activity. *NeuroImage*. 1996;4(3):183-193. doi:10.1006/nimg.1996.0069

61. Stefanovic B, Hutchinson E, Yakovleva V, et al. Functional Reactivity of Cerebral Capillaries. *J Cereb Blood Flow Metab*. 2008;28(5):961-972. doi:10.1038/sj.jcbfm.9600590

62. Hall CN, Reynell C, Gesslein B, et al. Capillary pericytes regulate cerebral blood flow in health and disease. *Nature*. 2014;508(7494):55-60. doi:10.1038/nature13165

63. Tian P, Teng IC, May LD, et al. Cortical depth-specific microvascular dilation underlies laminar differences in blood oxygenation level-dependent functional MRI signal.

Proceedings of the National Academy of Sciences. 2010;107(34):15246-15251. doi:10.1073/pnas.1006735107

64. Cai C, Fordsmann JC, Jensen SH, et al. Stimulation-induced increases in cerebral blood flow and local capillary vasoconstriction depend on conducted vascular responses. *Proceedings of the National Academy of Sciences*. 2018;115(25):E5796-E5804. doi:10.1073/pnas.1707702115

65. Chen BR, Bouchard MB, McCaslin AFH, Burgess SA, Hillman EMC. High-speed vascular dynamics of the hemodynamic response. *NeuroImage*. 2011;54(2):1021-1030. doi:10.1016/j.neuroimage.2010.09.036

66. Gao YR, Drew PJ. Effects of Voluntary Locomotion and Calcitonin Gene-Related Peptide on the Dynamics of Single Dural Vessels in Awake Mice. *J Neurosci*. 2016;36(8):2503-2516. doi:10.1523/JNEUROSCI.3665-15.2016

67. Reimer J, Froudarakis E, Cadwell CR, Yatsenko D, Denfield GH, Tolias AS. Pupil Fluctuations Track Fast Switching of Cortical States during Quiet Wakefulness. *Neuron*. 2014;84(2):355-362. doi:10.1016/j.neuron.2014.09.033

68. Honkura N, Richards M, Laviña B, Sáinz-Jaspeado M, Betsholtz C, Claesson-Welsh L. Intravital imaging-based analysis tools for vessel identification and assessment of concurrent dynamic vascular events. *Nat Commun*. 2018;9(1):2746. doi:10.1038/s41467-018-04929-8

69. Song A, Charles AS, Koay SA, et al. Volumetric two-photon imaging of neurons using stereoscopy (vTwINS). *Nat Methods*. 2017;14(4):420-426. doi:10.1038/nmeth.4226

70. Yang Y, Yao B, Lei M, et al. Two-Photon Laser Scanning Stereomicroscopy for Fast Volumetric Imaging. *PLoS One*. 2016;11(12):e0168885. doi:10.1371/journal.pone.0168885

71. Podgorski K, Ranganathan G. Brain heating induced by near-infrared lasers during multiphoton microscopy. *Journal of Neurophysiology*. 2016;116(3):1012-1023. doi:10.1152/jn.00275.2016

72. Stirman JN, Smith IT, Kudenov MW, Smith SL. Wide field-of-view, multi-region, two-photon imaging of neuronal activity in the mammalian brain. *Nat Biotechnol*. 2016;34(8):857-862. doi:10.1038/nbt.3594

73. Zhang T, Hernandez O, Chrapkiewicz R, et al. Kilohertz two-photon brain imaging in awake mice. *Nat Methods*. 2019;16(11):1119-1122. doi:10.1038/s41592-019-0597-2

74. Wang K, Horton NG, Charan K, Xu C. Advanced Fiber Soliton Sources for Nonlinear Deep Tissue Imaging in Biophotonics. *IEEE Journal of Selected Topics in Quantum Electronics*. 2014;20(2):50-60. doi:10.1109/JSTQE.2013.2276860

75. Cheng H, Tong S, Deng X, et al. Deep-brain 2-photon fluorescence microscopy in vivo excited at the 1700 nm window. *Opt Lett, OL*. 2019;44(17):4432-4435. doi:10.1364/OL.44.004432

76. Rodríguez C, Ji N. Adaptive optical microscopy for neurobiology. *Current Opinion in Neurobiology*. 2018;50:83-91. doi:10.1016/j.conb.2018.01.011

77. Ji N. Adaptive optical fluorescence microscopy. *Nat Methods*. 2017;14(4):374-380. doi:10.1038/nmeth.4218

78. Attwell D, Buchan AM, Charpak S, Lauritzen M, MacVicar BA, Newman EA. Glial and neuronal control of brain blood flow. *Nature*. 2010;468(7321):232-243. doi:10.1038/nature09613

79. Cipolla MJ. *The Cerebral Circulation*. Morgan & Claypool Life Sciences; 2009. Accessed December 1, 2022. http://www.ncbi.nlm.nih.gov/books/NBK53081/

80. Kulik T, Kusano Y, Aronhime S, Sandler AL, Winn HR. Regulation of cerebral vasculature in normal and ischemic brain. *Neuropharmacology*. 2008;55(3):281-288. doi:10.1016/j.neuropharm.2008.04.017

81. Itoh Y, Suzuki N. Control of Brain Capillary Blood Flow. *J Cereb Blood Flow Metab*. 2012;32(7):1167-1176. doi:10.1038/jcbfm.2012.5

82. Peppiatt CM, Howarth C, Mobbs P, Attwell D. Bidirectional control of CNS capillary diameter by pericytes. *Nature*. 2006;443(7112):700-704. doi:10.1038/nature05193

83. Pisauro MA, Benucci A, Carandini M. Local and global contributions to hemodynamic activity in mouse cortex. *Journal of Neurophysiology*. 2016;115(6):2931-2936. doi:10.1152/jn.00125.2016

84. Cardoso MMB, Sirotin YB, Lima B, Glushenkova E, Das A. The neuroimaging signal is a linear sum of neurally distinct stimulus- and task-related components. *Nat Neurosci*. 2012;15(9):1298-1306. doi:10.1038/nn.3170

85. Murphy PR, O'Connell RG, O'Sullivan M, Robertson IH, Balsters JH. Pupil diameter covaries with BOLD activity in human locus coeruleus. *Human Brain Mapping*. 2014;35(8):4140-4154. doi:10.1002/hbm.22466

86. Liu Y, Rodenkirch C, Moskowitz N, Schriver B, Wang Q. Dynamic Lateralization of Pupil Dilation Evoked by Locus Coeruleus Activation Results from Sympathetic, Not Parasympathetic, Contributions. *Cell Reports*. 2017;20(13):3099-3112. doi:10.1016/j.celrep.2017.08.094

87. Schriver BJ, Bagdasarov S, Wang Q. Pupil-linked arousal modulates behavior in rats performing a whisker deflection direction discrimination task. *Journal of Neurophysiology*. 2018;120(4):1655-1670. doi:10.1152/jn.00290.2018

88. Larsen RS, Waters J. Neuromodulatory Correlates of Pupil Dilation. *Frontiers in Neural Circuits*. 2018;12. Accessed December 1, 2022. https://www.frontiersin.org/articles/10.3389/fncir.2018.00021

89. Hamel E. Perivascular nerves and the regulation of cerebrovascular tone. *Journal of Applied Physiology*. 2006;100(3):1059-1064. doi:10.1152/japplphysiol.00954.2005

90. Valmianski I, Shih AY, Driscoll JD, Matthews DW, Freund Y, Kleinfeld D. Automatic Identification of Fluorescently Labeled Brain Cells for Rapid Functional Imaging. *Journal of Neurophysiology*. 2010;104(3):1803-1811. doi:10.1152/jn.00484.2010

91. Göbel W, Kampa BM, Helmchen F. Imaging cellular network dynamics in three dimensions using fast 3D laser scanning. *Nat Methods*. 2007;4(1):73-79. doi:10.1038/nmeth989

92. Wu JL, Xu YQ, Xu JJ, et al. Ultrafast laser-scanning time-stretch imaging at visible wavelengths. *Light Sci Appl*. 2017;6(1):e16196-e16196. doi:10.1038/lsa.2016.196

93. Lin MZ, Schnitzer MJ. Genetically encoded indicators of neuronal activity. *Nat Neurosci*. 2016;19(9):1142-1153. doi:10.1038/nn.4359

94. Cho EE, Drazic J, Ganguly M, Stefanovic B, Hynynen K. Two-photon fluorescence microscopy study of cerebrovascular dynamics in ultrasound-induced blood–brain barrier opening. *J Cereb Blood Flow Metab*. 2011;31(9):1852-1862. doi:10.1038/jcbfm.2011.59

95. Tufa U, Ringuette D, Wang XF, Levi O, Carlen P. Two-photon microscopy imaging of blood brain barrier leakage in fetal alcohol disorder mice. In: *Optics in the Life Sciences Congress (2017), Paper JTu4A.9*. Optica Publishing Group; 2017:JTu4A.9. doi:10.1364/BODA.2017.JTu4A.9

96. Han X, Chai Z, Ping X, et al. In vivo Two-Photon Imaging Reveals Acute Cerebral Vascular Spasm and Microthrombosis After Mild Traumatic Brain Injury in Mice. *Frontiers in Neuroscience*. 2020;14. Accessed November 30, 2022. https://www.frontiersin.org/articles/10.3389/fnins.2020.00210

97. Sword J, Masuda T, Croom D, Kirov SA. Evolution of neuronal and astroglial disruption in the peri-contusional cortex of mice revealed by in vivo two-photon imaging. *Brain*. 2013;136(5):1446-1461. doi:10.1093/brain/awt026

98. Chen W, Zhang Q, Natan R, Fan J, Ji N. Bessel-droplet foci enable high-resolution and high-contrast volumetric imaging of synapses and circulation in the brain in vivo. Published online March 6, 2022:2022.03.05.483143. doi:10.1101/2022.03.05.483143

99. Chen W, Natan RG, Yang Y, et al. In vivo volumetric imaging of calcium and glutamate activity at synapses with high spatiotemporal resolution. *Nat Commun*. 2021;12(1):6630. doi:10.1038/s41467-021-26965-7

100. Ji N, Milkie DE, Betzig E. Adaptive optics via pupil segmentation for high-resolution imaging in biological tissues. *Nat Methods*. 2010;7(2):141-147. doi:10.1038/nmeth.1411

101. Tyson RK, Frazier BW. *Principles of Adaptive Optics*. 5th ed. CRC Press; 2022. doi:10.1201/9781003140191

102. Platt BC, Shack R. History and principles of Shack-Hartmann wavefront sensing. *J Refract Surg*. 2001;17(5):S573-577. doi:10.3928/1081-597X-20010901-13

103. Wang C, Liu R, Milkie DE, et al. Multiplexed aberration measurement for deep tissue imaging in vivo. *Nat Methods*. 2014;11(10):1037-1040. doi:10.1038/nmeth.3068

104. Rodríguez C, Chen A, Rivera JA, et al. An adaptive optics module for deep tissue multiphoton imaging in vivo. *Nat Methods*. 2021;18(10):1259-1264. doi:10.1038/s41592-021-01279-0

105. 1024 x 1024 Spatial Light Modulator - Meadowlark Optics. Published March 4, 2022. Accessed December 1, 2022. https://www.meadowlark.com/1k-x-1k-spatial-light-modulator/

106. Marvin JS, Scholl B, Wilson DE, et al. Stability, affinity, and chromatic variants of the glutamate sensor iGluSnFR. *Nat Methods*. 2018;15(11):936-939. doi:10.1038/s41592-018-0171-3

107. Evans SW, Shi D, Chavarha M, et al. A positively Tuned Voltage Indicator Reveals Electrical Correlates of Calcium Activity in the Brain. Published online September 27, 2022:2021.10.21.465345. doi:10.1101/2021.10.21.465345

108. Meng G, Zhong J, Zhang Q, et al. Ultrafast two-photon fluorescence imaging of cerebral blood circulation in the mouse brain in vivo. *Proceedings of the National Academy of Sciences*. 2022;119(23):e2117346119. doi:10.1073/pnas.2117346119

109. Huang LK, Chao SP, Hu CJ. Clinical trials of new drugs for Alzheimer disease. *Journal of Biomedical Science*. 2020;27(1):18. doi:10.1186/s12929-019-0609-7

110. Sinyor M, Schaffer A, Levitt A. The Sequenced Treatment Alternatives to Relieve Depression (STAR*D) Trial: A Review. *Can J Psychiatry*. 2010;55(3):126-135. doi:10.1177/070674371005500303

111. Gabriel FC, Melo DO de, Fráguas R, Leite-Santos NC, Silva RAM da, Ribeiro E. Pharmacological treatment of depression: A systematic review comparing clinical practice guideline recommendations. *PLOS ONE*. 2020;15(4):e0231700. doi:10.1371/journal.pone.0231700

112. Yiannopoulou KG, Papageorgiou SG. Current and Future Treatments in Alzheimer Disease: An Update. *J Cent Nerv Syst Dis*. 2020;12:1179573520907397. doi:10.1177/1179573520907397

113. Bouthour W, Mégevand P, Donoghue J, Lüscher C, Birbaumer N, Krack P. Biomarkers for closed-loop deep brain stimulation in Parkinson disease and beyond. *Nat Rev Neurol*. 2019;15(6):343-352. doi:10.1038/s41582-019-0166-4

114. Scangos KW, Khambhati AN, Daly PM, et al. Closed-loop neuromodulation in an individual with treatment-resistant depression. *Nat Med*. 2021;27(10):1696-1700. doi:10.1038/s41591-021-01480-w

115. Janicak PG, Dokucu ME. Transcranial magnetic stimulation for the treatment of major depression. *Neuropsychiatr Dis Treat*. 2015;11:1549-1560. doi:10.2147/NDT.S67477

116. Voigt J, Carpenter L, Leuchter A. A systematic literature review of the clinical efficacy of repetitive transcranial magnetic stimulation (rTMS) in non-treatment resistant patients with major depressive disorder. *BMC Psychiatry*. 2019;19(1):13. doi:10.1186/s12888-018-1989-z

117. Miller KJ, Leuthardt EC, Schalk G, et al. Spectral Changes in Cortical Surface Potentials during Motor Movement. *J Neurosci*. 2007;27(9):2424-2432. doi:10.1523/JNEUROSCI.3886-06.2007

118. Wang W, Degenhart AD, Collinger JL, et al. Human motor cortical activity recorded with Micro-ECoG electrodes, during individual finger movements. In: *2009 Annual International Conference of the IEEE Engineering in Medicine and Biology Society*. ; 2009:586-589. doi:10.1109/IEMBS.2009.5333704

119. Gunduz A, Brunner P, Daitch A, et al. Neural Correlates of Visual–Spatial Attention in Electrocorticographic Signals in Humans. *Frontiers in Human Neuroscience*. 2011;5. Accessed November 27, 2022. https://www.frontiersin.org/articles/10.3389/fnhum.2011.00089

120. Chang EF, Rieger JW, Johnson K, Berger MS, Barbaro NM, Knight RT. Categorical speech representation in human superior temporal gyrus. *Nat Neurosci*. 2010;13(11):1428-1432. doi:10.1038/nn.2641

121. Mesgarani N, Chang EF. Selective cortical representation of attended speaker in multi-talker speech perception. *Nature*. 2012;485(7397):233-236. doi:10.1038/nature11020

122. Bouchard KE, Mesgarani N, Johnson K, Chang EF. Functional organization of human sensorimotor cortex for speech articulation. *Nature*. 2013;495(7441):327-332. doi:10.1038/nature11911

123. Chao Z, Nagasaka Y, Fujii N. Long-term asynchronous decoding of arm motion using electrocorticographic signals in monkey. *Frontiers in Neuroengineering*. 2010;3. Accessed November 27, 2022. https://www.frontiersin.org/articles/10.3389/fneng.2010.00003

124. Ryapolova-Webb E, Afshar P, Stanslaski S, et al. Chronic cortical and electromyographic recordings from a fully implantable device: preclinical experience in a nonhuman primate. *J Neural Eng*. 2014;11(1):016009. doi:10.1088/1741-2560/11/1/016009

125. Degenhart AD, Eles J, Dum R, et al. Histological Evaluation of a Chronically-implanted Electrocorticographic Electrode Grid in a Non-human Primate. *J Neural Eng*. 2016;13(4):046019. doi:10.1088/1741-2560/13/4/046019

126. Maynard EM, Hatsopoulos NG, Ojakangas CL, et al. Neuronal Interactions Improve Cortical Population Coding of Movement Direction. *J Neurosci*. 1999;19(18):8083-8093. doi:10.1523/JNEUROSCI.19-18-08083.1999

127. Flesher SN, Collinger JL, Foldes ST, et al. Intracortical microstimulation of human somatosensory cortex. *Science Translational Medicine*. 2016;8(361):361ra141-361ra141. doi:10.1126/scitranslmed.aaf8083

128. Johnson LA, Wander JD, Sarma D, Su DK, Fetz EE, Ojemann JG. Direct electrical stimulation of the somatosensory cortex in humans using electrocorticography electrodes: a qualitative and quantitative report. *J Neural Eng*. 2013;10(3):036021. doi:10.1088/1741-2560/10/3/036021

129. Hiremath SV, Tyler-Kabara EC, Wheeler JJ, et al. Human perception of electrical stimulation on the surface of somatosensory cortex. *PLOS ONE*. 2017;12(5):e0176020. doi:10.1371/journal.pone.0176020

130. Lee B, Kramer D, Armenta Salas M, et al. Engineering Artificial Somatosensation Through Cortical Stimulation in Humans. *Frontiers in Systems Neuroscience*. 2018;12. Accessed November 27, 2022. https://www.frontiersin.org/articles/10.3389/fnsys.2018.00024

131. Fifer MS, McMullen DP, Osborn LE, et al. Intracortical Somatosensory Stimulation to Elicit Fingertip Sensations in an Individual With Spinal Cord Injury. *Neurology*. 2022;98(7):e679-e687. doi:10.1212/WNL.0000000000013173

132. Caldwell DJ, Cronin JA, Wu J, et al. Direct stimulation of somatosensory cortex results in slower reaction times compared to peripheral touch in humans. *Sci Rep*. 2019;9(1):3292. doi:10.1038/s41598-019-38619-2

133. Metzger SL, Liu JR, Moses DA, et al. Generalizable spelling using a speech neuroprosthesis in an individual with severe limb and vocal paralysis. *Nat Commun*. 2022;13(1):6510. doi:10.1038/s41467-022-33611-3

134. Wang W, Collinger JL, Degenhart AD, et al. An Electrocorticographic Brain Interface in an Individual with Tetraplegia. *PLoS One*. 2013;8(2):e55344. doi:10.1371/journal.pone.0055344

135. Morrell MJ. Responsive cortical stimulation for the treatment of medically intractable partial epilepsy. *Neurology*. 2011;77(13):1295-1304. doi:10.1212/WNL.0b013e3182302056

136. Heck CN, King-Stephens D, Massey AD, et al. Two-year seizure reduction in adults with medically intractable partial onset epilepsy treated with responsive neurostimulation: Final results of the RNS System Pivotal trial. *Epilepsia*. 2014;55(3):432-441. doi:10.1111/epi.12534

137. Chang HT. Changes in excitability of cerebral cortex following single electric shock applied to cortical surface. *J Neurophysiol*. 1951;14(2):95-111. doi:10.1152/jn.1951.14.2.95

138. Lorente de No R. Cerebral cortex: architecture, intracortical connections, motor projections. *Physiology of the nervous system*. Published online 1938:288-313.

139. Larriva-Sahd JA. Some predictions of Rafael Lorente de Nó 80 years later. *Front Neuroanat*. 2014;8:147. doi:10.3389/fnana.2014.00147

140. Stoney SD, Thompson WD, Asanuma H. Excitation of pyramidal tract cells by intracortical microstimulation: effective extent of stimulating current. *J Neurophysiol*. 1968;31(5):659-669. doi:10.1152/jn.1968.31.5.659

141. Ranck JB. Which elements are excited in electrical stimulation of mammalian central nervous system: a review. *Brain Res*. 1975;98(3):417-440. doi:10.1016/0006-8993(75)90364-9

142. Nowak LG, Bullier J. Axons, but not cell bodies, are activated by electrical stimulation in cortical gray matter. I. Evidence from chronaxie measurements. *Exp Brain Res*. 1998;118(4):477-488. doi:10.1007/s002210050304

143. Nowak LG, Bullier J. Axons, but not cell bodies, are activated by electrical stimulation in cortical gray matterII. Evidence from selective inactivation of cell bodies and axon initial segments. *Exp Brain Res*. 1998;118(4):489-500. doi:10.1007/s002210050305

144. Rattay F. The basic mechanism for the electrical stimulation of the nervous system. *Neuroscience*. 1999;89(2):335-346. doi:10.1016/S0306-4522(98)00330-3

145. Tehovnik EJ, Slocum WM. Two-photon imaging and the activation of cortical neurons. *Neuroscience*. 2013;245:12-25. doi:10.1016/j.neuroscience.2013.04.022

146. Dadarlat MC, Sun YJ, Stryker MP. Spatiotemporal recruitment of inhibition and excitation in the mammalian cortex during electrical stimulation. Published online June 4, 2022:2022.06.03.494729. doi:10.1101/2022.06.03.494729

147. Michelson NJ, Eles JR, Vazquez AL, Ludwig KA, Kozai TD. Calcium activation of cortical neurons by continuous electrical stimulation: Frequency-dependence, temporal fidelity and activation density. *J Neurosci Res*. 2019;97(5):620-638. doi:10.1002/jnr.24370

148. Eles JR, Stieger KC, Kozai TDY. The temporal pattern of intracortical microstimulation pulses elicits distinct temporal and spatial recruitment of cortical neuropil and neurons. *J Neural Eng*. 2021;18(1):015001. doi:10.1088/1741-2552/abc29c

149. Stieger KC, Eles JR, Ludwig KA, Kozai TDY. Intracortical microstimulation pulse waveform and frequency recruits distinct spatiotemporal patterns of cortical neuron and neuropil activation. *J Neural Eng*. 2022;19(2). doi:10.1088/1741-2552/ac5bf5

150. Komarov M, Malerba P, Golden R, Nunez P, Halgren E, Bazhenov M. Selective recruitment of cortical neurons by electrical stimulation. *PLOS Computational Biology*. 2019;15(8):e1007277. doi:10.1371/journal.pcbi.1007277

151. Halgren A, Siegel Z, Golden R, Bazhenov M. Multielectrode Cortical Stimulation Selectively Induces Unidirectional Wave Propagation. Published online April 1, 2021:2020.11.28.402289. doi:10.1101/2020.11.28.402289

152. Kumaravelu K, Sombeck J, Miller LE, Bensmaia SJ, Grill WM. Stoney vs. Histed: Quantifying the spatial effects of intracortical microstimulation. *Brain Stimulation*. 2022;15(1):141-151. doi:10.1016/j.brs.2021.11.015

153. Kumaravelu K, Tomlinson T, Callier T, et al. A comprehensive model-based framework for optimal design of biomimetic patterns of electrical stimulation for prosthetic sensation. *J Neural Eng*. 2020;17(4):046045. doi:10.1088/1741-2552/abacd8

154. Vinck M, Batista-Brito R, Knoblich U, Cardin JA. Arousal and Locomotion Make Distinct Contributions to Cortical Activity Patterns and Visual Encoding. *Neuron*. 2015;86(3):740-754. doi:10.1016/j.neuron.2015.03.028

155. Ganji M, Paulk AC, Yang JC, et al. Selective Formation of Porous Pt Nanorods for Highly Electrochemically Efficient Neural Electrode Interfaces. *Nano Lett*. 2019;19(9):6244-6254. doi:10.1021/acs.nanolett.9b02296

156. Tchoe Y, Bourhis AM, Cleary DR, et al. Human brain mapping with multithousand-channel PtNRGrids resolves spatiotemporal dynamics. *Science Translational Medicine*. 2022;14(628):eabj1441. doi:10.1126/scitranslmed.abj1441

157. Thunemann M, Lu Y, Liu X, et al. Deep 2-photon imaging and artifact-free optogenetics through transparent graphene microelectrode arrays. *Nat Commun*. 2018;9(1):2035. doi:10.1038/s41467-018-04457-5

158. Gage GJ, Stoetzner CR, Richner T, Brodnick SK, Williams JC, Kipke DR. Surgical Implantation of Chronic Neural Electrodes for Recording Single Unit Activity and Electrocorticographic Signals. *J Vis Exp*. 2012;(60):3565. doi:10.3791/3565

159. Chung JE, Joo HR, Smyth CN, et al. Chronic Implantation of Multiple Flexible Polymer Electrode Arrays. *J Vis Exp*. 2019;(152). doi:10.3791/59957

160. Dipoppa M, Ranson A, Krumin M, Pachitariu M, Carandini M, Harris KD. Vision and Locomotion Shape the Interactions between Neuron Types in Mouse Visual Cortex. *Neuron*. 2018;98(3):602-615.e8. doi:10.1016/j.neuron.2018.03.037

161. Wilson NR, Runyan CA, Wang FL, Sur M. Division and subtraction by distinct cortical inhibitory networks in vivo. *Nature*. 2012;488(7411):343-348. doi:10.1038/nature11347

162. Atallah BV, Bruns W, Carandini M, Scanziani M. Parvalbumin-Expressing Interneurons Linearly Transform Cortical Responses to Visual Stimuli. *Neuron*. 2012;73(1):159-170. doi:10.1016/j.neuron.2011.12.013

163. Lee SH, Kwan AC, Zhang S, et al. Activation of specific interneurons improves V1 feature selectivity and visual perception. *Nature*. 2012;488(7411):379-383. doi:10.1038/nature11312

164. Tan AYY, Brown BD, Scholl B, Mohanty D, Priebe NJ. Orientation Selectivity of Synaptic Input to Neurons in Mouse and Cat Primary Visual Cortex. *J Neurosci*. 2011;31(34):12339-12350. doi:10.1523/JNEUROSCI.2039-11.2011

165. Li Y tang, Liu B hua, Chou X lin, Zhang LI, Tao HW. Synaptic Basis for Differential Orientation Selectivity between Complex and Simple Cells in Mouse Visual Cortex. *J Neurosci*. 2015;35(31):11081-11093. doi:10.1523/JNEUROSCI.5246-14.2015

166. Schuman B, Machold RP, Hashikawa Y, Fuzik J, Fishell GJ, Rudy B. Four Unique Interneuron Populations Reside in Neocortical Layer 1. *J Neurosci*. 2019;39(1):125-139. doi:10.1523/JNEUROSCI.1613-18.2018

167. Malina KCK, Tsivourakis E, Kushinsky D, et al. NDNF interneurons in layer 1 gain-modulate whole cortical columns according to an animal's behavioral state. *Neuron*. 2021;109(13):2150-2164.e5. doi:10.1016/j.neuron.2021.05.001

168. Schuman B, Dellal S, Prönneke A, Machold R, Rudy B. Neocortical Layer 1: An Elegant Solution to Top-Down and Bottom-Up Integration. *Annual Review of Neuroscience*. 2021;44(1):221-252. doi:10.1146/annurev-neuro-100520-012117

169. Tamás G, Simon AL Anna, Szabadics J. Identified Sources and Targets of Slow Inhibition in the Neocortex. *Science*. 2003;299(5614):1902-1905. doi:10.1126/science.1082053

170. Oláh S, Füle M, Komlósi G, et al. Regulation of cortical microcircuits by unitary GABA-mediated volume transmission. *Nature*. 2009;461(7268):1278-1281. doi:10.1038/nature08503

171. Abs E, Poorthuis RB, Apelblat D, et al. Learning-Related Plasticity in Dendrite-Targeting Layer 1 Interneurons. *Neuron*. 2018;100(3):684-699.e6. doi:10.1016/j.neuron.2018.09.001

172. Park J, Papoutsi A, Ash RT, Marin MA, Poirazi P, Smirnakis SM. Contribution of apical and basal dendrites to orientation encoding in mouse V1 L2/3 pyramidal neurons. *Nat Commun*. 2019;10(1):5372. doi:10.1038/s41467-019-13029-0

173. Jiang X, Wang G, Lee AJ, Stornetta RL, Zhu JJ. The organization of two new cortical interneuronal circuits. *Nat Neurosci*. 2013;16(2):210-218. doi:10.1038/nn.3305

174. Schulz JM, Kay JW, Bischofberger J, Larkum ME. GABAB Receptor-Mediated Regulation of Dendro-Somatic Synergy in Layer 5 Pyramidal Neurons. *Frontiers in Cellular Neuroscience*. 2021;15. Accessed October 27, 2022. https://www.frontiersin.org/articles/10.3389/fncel.2021.718413

175. Marvin JS, Shimoda Y, Magloire V, et al. A genetically encoded fluorescent sensor for in vivo imaging of GABA. *Nat Methods*. 2019;16(8):763-770. doi:10.1038/s41592-019-0471-2

176. Adesnik H, Bruns W, Taniguchi H, Huang ZJ, Scanziani M. A neural circuit for spatial summation in visual cortex. *Nature*. 2012;490(7419):226-231. doi:10.1038/nature11526

177. Keller AJ, Dipoppa M, Roth MM, et al. A Disinhibitory Circuit for Contextual Modulation in Primary Visual Cortex. *Neuron*. 2020;108(6):1181-1193.e8. doi:10.1016/j.neuron.2020.11.013

178. Stieger KC, Eles JR, Ludwig KA, Kozai TDY. In vivo microstimulation with cathodic and anodic asymmetric waveforms modulates spatiotemporal calcium dynamics in cortical neuropil and pyramidal neurons of male mice. *Journal of Neuroscience Research*. 2020;98(10):2072-2095. doi:10.1002/jnr.24676

179. Turcotte R, Liang Y, Tanimoto M, et al. Dynamic super-resolution structured illumination imaging in the living brain. *Proceedings of the National Academy of Sciences*. 2019;116(19):9586-9591. doi:10.1073/pnas.1819965116

180. Tan Z, Sun W, Chen TW, Kim D, Ji N. Neuronal Representation of Ultraviolet Visual Stimuli in Mouse Primary Visual Cortex. *Sci Rep*. 2015;5(1):12597. doi:10.1038/srep12597

181. Liang Y, Fan JL, Sun W, Lu R, Chen M, Ji N. A Distinct Population of L6 Neurons in Mouse V1 Mediate Cross-Callosal Communication. *Cerebral Cortex*. 2021;31(9):4259-4273. doi:10.1093/cercor/bhab084